APPLICATIONS OF THE KIRCHHOFF-HELMHOLTZ INTEGRAL TO PROBLEMS IN BODY WAVE SEISMOLOGY

Thesis by

Patricia Frances Scott

In Partial Fulfillment of the Requirements

for the Degree of

Doctor of Philosophy

California Institute of Technology

Pasadena, California

1985

(Submitted September 25, 1984)

Acknowledgements

First, I would like to thank God that this is all over! Secondly, I wish to express my gratitude for the tremendous patience Donald Helmberger has shown in allowing me to pursue my thesis topic. I have benefited greatly from my association with him and all the other faculty, students and staff at the Seismo. Lab. I shall miss you all. Thirdly, I wish to acknowledge the tremendous support I have received from the people who assisted me in preparing this thesis. Gladys Engen graciously provided me with essential plotting software. Laszlo Lenches, Cindy Arvesen, and Pat Lee of Graphic Arts prepared the excellent figures. Nancy Durland and Betty Solomon did the difficult job of word processing. Finally, I would to like thank my mother, father, Charles, and Dave. Without their love, this thesis could not have been done. It is to them that this work is dedicated.

This research was supported by:

ONR contract 14-76-C-1070

Abstract

This thesis describes a procedure for evaluating the Kirchhoff-Helmholtz integral and presents applications of it which involve the interpretation of amplitude and travel time anomalies of body waves. The method of integration is a summation of single point evaluations of the integrand and requires that spacing of these evaluations on the surface be small compared to the wavelength of the incident disturbance. The technique predicts amplitudes, travel times and waveforms of acoustic potentials that propagate through a homogeneous medium and interact with three-dimensional curved boundaries. Results from test models compare well with optical solutions for reflections off planar interfaces and rigid spheres and transmissions through planar interfaces.

The reflected integral solution is used to simulate the effect of an idealized mountain on the amplitude and waveforms on pP. This structure causes multiple arrivals, phase shifts, and amplitude anomalies in the synthetic reflection profile. Also the effects of spall on pP waves generated by explosions are simulated by specifying position dependent reflection coefficient on the surface of integration. These experiments predict frequency dependent amplitude anomalies and travel time delays of the reflections.

The transmitted solution is used to model the effect of several idealized crust-mantle boundary structures on teleseismic P waves generated by explosions. The structures are upwarps and produce travel time residuals as a function of delta and azimuth which have the same magnitude as residuals observed for NTS tests within Pahute Mesa. The structures cause early

complicated low amplitude waveforms and late simple high amplitude waveforms. Thus they cause systematic amplitude variations with azimuth, delta, and source location. The magnitude of predicted variation is less than the observed ab amplitude variation with azimuth of Pahute Mesa tests; however, it is approximately the same as the observed ab variation at a given station as a function of test location within the mesa.

The integral method is extended to include a symmetric velocity function in the medium and is used to model ScS waves which propagate through a JB Earth and reflect off a bumpy core-mantle boundary. Solutions with this extension establish that isovelocity Kirchhoff solutions are sufficient to predict the relative amplitude and travel time anomalies of ScS arising from core-mantle boundary relief. Isovelocity modeling shows that upwarps 300 to 600 kilometers wide and at least 10 kilometers high cause precursors to ScS and amplitude reductions of the same magnitude as the observations. However, the height is not mechanically feasible; therefore, the anomalous observations must originate elsewhere.

Table of Contents

General Introduction

A problem confronting seismologists with increasing frequency is assessing the effect of a localized heterogeneity on the waveforms, amplitudes, and travel times of body waves. Several data analyses indicate that most of the propagation path is uncomplicated and can be adequately modeled by existing planar, cylindrical, or spherically symmetric solutions. However, there are areas along the path which have either warped material boundaries, lateral changes in density, or lateral changes in P or S wave velocities. Propagation through these regions cannot be modeled by these solutions.

Given evidence of heterogeneity in the Earth, one can resort to finite difference, finite element, and Rayleigh-FFT techniques to model these processes. But these three techniques are not feasible for teleseismic problems because the propagation path is several hundred wavelengths long. Alternatively one can use geometric ray theory. But this method is only valid if the wavelength of the disturbance is short. Moreover, obtaining the geometric ray path through a complicated medium is often a cumbersome numerical process. Thus an increasing number of workers are turning to hybrid schemes which exploit boundary integral representations to couple the intensive numerical schemes with the spherical, cylindrical, or planar solutions (Harkrider, 1981). The numerical codes calculate the effects of heterogeneity at short distances and the analytical solutions provide the Green's operator which propagates the resultant disturbance through the longer and simpler parts of the path.

Perhaps the simplest hybrid scheme at present is the one used in this thesis. It is the numerical evaluation of the integral representation of the

scalar wave equation with the incorporation of plane wave reflection and transmission coefficients and geometric ray theory to estimate boundary values on the surface. Appendix A describes the theory of this technique. In this appendix we show how the scalar integral representation is obtained from the scalar wave equation. We also derive the plane-wave geometric boundary values by making a series of approximations to the scalar integral representation. The technique represents an improvement over ray tracing because it provides solutions which are valid for longer wavelengths. It predicts diffracted arrivals and does not become singular. It produces phase shifts in a physical manner. Rather than tracking the spreading of a ray tube to determine if the disturbance is tangent to a caustic surface, this scalar integral method, called the Kirchhoff-Helmholtz integral, produces phase shifts by the destructive and constructive interference of secondary point sources on the surface of integration. The method is easy to use as there are no cumbersome numerical calculations.

Of course, there are disadvantages. The particular boundary values we choose do not allow for surface shadowing or multiple scattering caused by irregularities on the surface. This particular lack can be corrected if the surface has simplifying characteristics such as periodicity. But we do not correct for these problems. Instead we try to insure that they are not important for the shapes and source-receiver positions we investigate. The most important deficiency is that the limits of applicability are unknown because the boundary values on the surface are obtained by analogy. Rather than solve the exact problem, we solve a simpler one by assigning the

boundary values on the surface based on physical reasoning. The Kirchhoff-Helmholtz solution is not an expansion of an accurate solution with respect to a small parameter. This contrasts with perturbation solutions. Consequently we cannot precisely evaluate the error terms as we can with finite difference, finite element, or perturbation approaches. So although the Kirchhoff-Helmholtz integral appears to be a broader band solution than optics, we cannot precisely quantify this statement. Ultimately, small scale laboratory modeling and more theoretical work on the integral representation theorem (Meecham, 1956) will quantify the errors of this technique.

With these caveats in mind, we develop a method to evaluate the Kirchhoff-Helmholtz integral and apply it to problems of interest to global seismologists. This technique has been applied to problems in exploration geophysics. Indeed, it was the success of the integral formulation as a tool for migration and forward modeling in exploration geophysics which led us to search for other potential applications. Virtually all small scale laboratory modeling that verifies Kirchhoff-Helmholtz solutions originates from exploration geophysicists (Hilterman, 1970; Smith, 1981; French, 1975). Because the applications in this thesis differ from those of exploration geophysicists, the formalism and approximations differ somewhat. The goal of the exploration geophysicist is to develop a convolution operator from the scalar integral representation which rapidly migrates dense arrays of narrow angle reflection data. Several authors (Berryhill, 1979; Berryhill, 1977; Schneider, 1978) show that the Kirchhoff integral collapses to such an operator if 1) the source and receiver are coincident and 2) the Green's function is selected

such that the gradient term in the integral vanishes. The premium in these developments is speed of the migration operators. Hence the form of a convolution is a convenient result. In contrast, speed is not an essential feature of the work presented in this thesis, although the calculations are not particularly lengthy. Because we are modeling rather sparse data sets, we are more flexible in the selection of the method of evaluation of the integral, the nature of the surfaces, and the source-receiver positions.

In Chapter 1 we outline in detail the implementation of the Kirchhoff integral solution for reflections off a warped material boundary. The method of integration throughout this thesis is a summation of single point evaluations of the integral and, consequently, requires that the grid spacing of the surface be small relative to the incident wavelength of the source. This method of integration is simple. We apply the technique toward a quantitative estimation of how free surface topography distorts short period teleseismic pP. This phase is used with direct P and sP to infer the details of the source time history of earthquakes. The question is, then, can topography contaminate short period seismograms such as to render these data inappropriate for source studies. We also simulate the effect of spallation on pP waves generated by nuclear blasts. The separation of rock layers caused by severe tensional stresses generated by underground explosions is a phenomenon clearly seen on near field recordings of accelerations and velocities. Whether this phenomenon degrades the pP phase is still unanswered but this question is important to workers trying to infer near field processes of nuclear test with remote data.

Chapter 2 is an extension of the Kirchhoff-Helmholtz method to calculations of transmissions through warped boundaries. This extended modeling ability is applied toward the prediction of the effect of near source geologic structures on transmitted P waves generated by nuclear blasts. These phases have both travel time and amplitude anomalies as a function of delta and azimuth. We examine to see whether simple shapes on the Moho which cause travel time residuals can produce the amplitude anomalies. These experiments are important in isolating whether tectonic release or geologic structure is more dominant in impacting short period waves.

The Kirchhoff-Helmholtz method is further extended in chapter 3 to allow the medium of propagation to have a JB velocity function. This extension causes a substantial change in the method of evaluation of the integral because we must trace rays to the surface of integration. It is a more flexible way of evaluating the Kirchhoff-Helmholtz integral and can be used to model waves which travel through a medium with a symmetric velocity structure and interact with a warped boundary. With this new technique and the isovelocity method discussed in Chapter 1, we estimate the size of core-mantle relief needed to produce the amplitude and travel time anomalies of ScS waves. Such an estimate provides insight into the nature of core-mantle boundary and/or D" processes.

This thesis is a beginning in the routine use of the elastic and scalar boundary integral representations to evaluate the impact of heterogeneity on teleseismic body and surface waves. Clearly there are many manipulations of integral representations, numerical approximations of equations,

and analytic solutions yet to be explored. Ultimately we can expect to deduce an equivalent source representation for near source or receiver heterogeneity with the integral equations (Clayton, pers. comm., 1982). Once this formalism is established, then heterogeneity can be put in the synthetic seismogram much in the way earthquakes sources are convolved into a synthetic. This will greatly streamline the modeling process such that inversion schemes will be feasible.

REFERENCES

Berryhill, J. (1977), "Diffraction response for non-zero separation of source and receiver," Geophys., 42, 1158-1176.

Berryhill, J. (1979), "Wave-equation datuming," Geophys., 44, 1329-1344.

Clayton, R. (1982), personal communication

French, W. (1975), "Computer migrations of oblique seismic reflection profiles," Geophys., 40, 961-980.

Harkrider, D. (1981), "Coupling near source phenomena into surface wave generation," in *Identification of Seismic Source - Earthquake or Underground Explosion*, D. Reidel Publishing Co., 277-326.

Hilterman, F. (1970), "Three-dimensional seismic modeling," Geophys., 35, 1020-1037.

Meecham, W. C. (1956), "On the use of the Kirchhoff Approximation for the solution of reflection problems," J. Rational Mech. Anal., 5, 323-333.

Schneider, W. (1978), "Integral formulation for migration in two and three dimensions," Geophys., 43, 49-76.

Smith, T. (1981), "Three-dimensional Kirchhoff methods of acoustic modeling and migration," (thesis, University of Houston).

Chapter 1

Applications of the Reflected Kirchhoff solution

Introduction

Many observed seismic wave phenomena cannot be adequately modeled with solutions to plane-layered and radially symmetric media. For example, amplitude and $\frac{dT}{d\Delta}$ anomalies of teleseismic arrivals at large arrays (Glover and Alexander, 1969; Walck and Minster, 1982) which vary as a function of azimuth suggest the existence of velocity heterogeneities at depth. P and S body waves recorded on short and long period WWSSN stations also have amplitude and travel time anomalies which might be caused by non-planar boundaries. The increasing use of body wave amplitude and waveform information as well as travel times to infer sources, Q, and average velocity structures requires a knowledge of the manner in which lateral heterogeneity in the medium can affect these features of seismic waves. In many applications, heterogeneities act to contaminate the seismic data and prevent us from determining the real parameters of interest. For example, we might want to correct the relative amplitudes of short period pP and sP for the presence of the San Gabriel mountains in order to obtain a detailed source model for the San Fernando earthquake of 1971 (Langston, 1978). In other applications, we are directly interested in predicting amplitudes and travel times of waves interacting with non-planar structures. For example, we might wish to know how the Los Angeles sedimentary basin focuses strong ground motions, which are potentially destructive to building structures.

Clearly, there is a need for methods of predicting the effect of material boundary shape on seismic waves.

Numerical schemes which handle material irregularities are in abundance. Finite difference and finite element codes have been used successfully (Boore et al., 1971; Smith, 1975) and can be applied to a variety of materials; however, the expense of calculating the response at distances which are large compared to the wavelength of interest is prohibitive. These methods are altogether unfeasible at teleseismic distances. Rayleigh-FFT techniques have been exploited for these problems (Aki and Larner, 1970). Implementation of this technique for prediction of three-dimensional scattering is also costly. Geometric ray methods are useful for predicting scattering of signals which have wavelengths that are short compared to the size of the heterogeneity (Hong and Helmberger, 1978). Geometric ray methods have the shortcomings that they do not predict frequency-dependent amplitudes of scattered pulses, they do not handle diffracted arrivals, and they do predict infinite amplitudes at caustics.

In this chapter we develop and implement a method which can be used to model teleseismic arrivals at finite frequencies. It is based on a numerical evaluation of the scalar integral representation and incorporates tangent-plane approximations to evaluate the boundary values on the surface of integration. The method predicts the effects of non-planar three-dimensional boundaries on reflected scalar potentials. The medium in which these potentials propagate is linear and acoustic. We use the resulting potentials, which behave analogously to P-wave displacements, to understand

the effects of structure on P and SH waves. This analogy has been successfully applied in exploration geophysics (Claerbout, 1976) for the interpretation of reflection profiles. After verifying the accuracy of our numerics, we then use the method to predict the effect of mountains and spallation on pP waves.

Discussion of techniques

The method presented in this chapter is an integral equation approach and is based on the evaluation of the scalar integral equation variously called the Kirchhoff, Helmholtz, or Huygen's integral. This equation is a formulation of the wave equation in terms of a linear surface integral over the boundary of a continuous volume. That is, the scalar wave equation is

$$\frac{1}{\alpha^2}\frac{\partial^2\varphi}{\partial t^2} - \nabla^2\varphi(\underline{\xi},t) = \Phi\,, \tag{1.1}$$

Here $\varphi(\underline{\xi},t)$ is the field at a point $\underline{\xi}$ resulting from a source potential Φ and α is the wave speed. Following the formalism discussed by Mow and Pao (1971), we consider the motion of a homogeneous body V with a smooth boundary ∂V with outward pointing normal $\underline{n}$. Then if $\underline{\xi}\ \varepsilon\ V$ and $t\ \varepsilon\ (0,\infty)$

$$\varphi(\underline{\xi},t) = \int_V \int_0^{\infty} G(\underline{\xi},\underline{x},t-t_0)\Phi(\underline{x},t)\,dt_0\,dV_x$$

$$+ \frac{1}{\alpha^2}\int_V \left\{G(\underline{\xi},\underline{x},t)\frac{\partial\varphi}{\partial t}(\underline{x},0) + \varphi(\underline{x},0)\frac{\partial G}{\partial t}(\underline{\xi},\underline{x},t)\right\} dV_x \tag{1.2}$$

$$+ \int_{\partial V}\int_0^{\infty} \left\{G(\underline{\xi},\underline{x},t)\nabla_x\varphi(\underline{x},t) - \varphi(\underline{x},t)\nabla_x G(\underline{\xi},\underline{x},t-t_0)\right\}$$

$$\cdot\,\underline{n}(\underline{x})\,dt_0\,dS_x\,.$$

Here $G(\underline{\xi},\underline{x},t-t_0)$ is the fundamental singular solution of the scalar wave equation

$$\frac{1}{\alpha^2}\frac{\partial^2 G}{\partial t^2} - \nabla_x^2 G(\underline{\xi},\underline{x},t-t_0) = \delta(t-t_0)\delta(\underline{\xi}-\underline{x})\,. \tag{1.3}$$

Let us define $f(\underline{\varepsilon},t)$ as the sum of the first two integrals in equation (1.2). Then $f(\underline{\varepsilon},t)$ can be interpreted as the whole-space solution of the problem with sources $\Phi(\underline{x},t_0)$ and initial values $\frac{\partial \varphi}{\partial t}(\underline{x},0)$ and $\varphi(\underline{x},0)$ (Cole, 1980). Hence, $\varphi(\underline{\varepsilon},t)$ is a sum of the direct pulse and a reflected pulse from the surface which is described by the third integral in equation (1.2).

If $\underline{\varepsilon} \notin V$, then the left-hand side of equation (1.2) is zero. If $\underline{\varepsilon} \in \partial V$, then

$$\frac{1}{2}\varphi(\underline{\varepsilon},t) = \tag{1.4}$$

$$\int_0^{\infty} P \int_{\partial V} \left\{ G(\underline{\varepsilon},\underline{x},t-t_0)\nabla_x \varphi(\underline{x},t) - \varphi(\underline{x},t)\nabla_x G(\underline{\varepsilon},\underline{x},t-t_0) \right\}$$

$$\cdot \underline{n}(\underline{x})\, dt_0 dS_x + f(\underline{\varepsilon},t).$$

Here P denotes the principal value of the integral. A detailed derivation of equation (1.4) can be found in Cole (1980) for the elastic case. This result requires that G has a specific asymptotic behavior at its singularity. The function G used in the Kirchhoff formulation here meets this requirement. Specifically

$$G(\underline{\varepsilon},\underline{x},t-t_0) = \frac{\delta(t-t_0)}{4\pi|\underline{x}-\underline{\varepsilon}|}; \quad t_0 = \frac{|\underline{x}-\underline{\varepsilon}|}{\alpha}. \tag{1.5}$$

and

$$\frac{\partial G}{\partial n} = \frac{1}{4\pi}\frac{\partial r}{\partial n}\left\{ -\frac{\delta(t-t_0)}{r^2} - \frac{\delta'(t-t_0)}{\alpha r} \right\}. \tag{1.5a}$$

Substitution of these functions into equation (1.2) gives a familiar optics

formula (Born and Wolf, 1964)

$$\varphi(\underline{\xi},t)= \frac{1}{4\pi}\int \left\{\frac{1}{r}\left[\frac{\partial\varphi}{\partial n}\right] - \left[\varphi\right]\frac{\partial r}{\partial n}\frac{\partial}{\partial r}\left[\frac{1}{r}\right] + \frac{1}{r\alpha}\frac{\partial r}{\partial n}\left[\frac{\partial\varphi}{\partial t}\right]\right\} dS_x + f(\underline{\xi},t) \quad (1.6)$$

where $r = |\underline{x}-\underline{\xi}|$, the distance from receiver to surface, and $\frac{\partial r}{\partial n} = \nabla|\underline{x}-\underline{\xi}| \cdot \underline{n}$. The square brackets denote the values of the functions on ∂V at the time $t - \frac{|\underline{x}-\underline{\xi}|}{\alpha}$.

The expressions (1.2), (1.4), and (1.6) are exact if the boundary values are correct and are a mathematical representation of Huygen's principle; that is, a disturbance at a receiver point is a superposition of secondary waves proceeding from a surface existing between that point and the source. Diffraction phenomena arise from the mutual interference of these secondary disturbances. However, one needs the value of the potential and its normal derivative on the surface to calculate $\varphi(\underline{\xi},t)$. Equation (1.4) may be solved for φ or $\nabla\varphi \cdot \underline{n}$ on the surface subject to some constraints imposed by boundary conditions (e.g., continuity of φ or $\nabla\varphi \cdot \underline{n}$ across the boundary). This approach is taken by Mitzner (1967) who sets $\nabla\varphi \cdot \underline{n}$ equal to zero and solves for φ. However, this approach is costly for high frequency scattering.

Alternatively, one may estimate the values on the surface by invoking an approximation. This approach is used throughout this study. If we assume a point source at $\underline{x}_o$, the boundary values on the surface are well approximated by

$$\varphi(\underline{x},t) = \frac{f(t-t_1)}{|\underline{x}-\underline{x}_o|}(1+D)\,; \quad t_1 = \frac{|\underline{x}-\underline{x}_o|}{\alpha} \qquad (1.7)$$

$$\frac{\partial \varphi}{\partial n} = \frac{\partial r_0}{\partial n}(1-D)\left\{\frac{-f(t-t_1)}{r_0^2} - \frac{f'(t-t_1)}{\alpha r_0}\right\} . \qquad (1.8)$$

Here $r_0 = |\underline{x} - \underline{x}_o|$, the distance from the source to the surface, $\frac{\partial r_0}{\partial n} = \nabla|\underline{x} - \underline{x}_o| \cdot \underline{n}$. D is the local plane-wave planar interface reflection coefficient, and f(t) and f'(t) are the source time function and its derivative, respectively. The reflection coefficient depends on incidence angle. This approximation is variously called the Kirchhoff, physical optics, or the tangent plane hypothesis and is widely used by workers studying electromagnetic scattering (Davies, 1954). It assumes that the incident pulse is sufficiently high frequency so that locally the amplitude decay is described by both geometric ray theory and plane-wave reflection coefficients. Therefore, every point on the surface reflects the incident pulse as though there were an infinite plane tangent to the surface at that point. The values of the potential and its normal derivative at a point are independent of the boundary values at other points. Hence the effects of multiple scattering and diffractions along the surface are neglected.

Upon substituting the functions (1.5),(1.5a),(1.7) and (1.8) into (1.2), one obtains for the reflected potential

$$\varphi_r(\underline{\varepsilon},t) = \frac{1}{4\pi}\int_{\partial V} D\left\{\frac{1}{r r_0^2}\frac{\partial r_0}{\partial n} + \frac{1}{r^2 r_0}\frac{\partial r}{\partial n}\right\} f(t-t_0-t_1)\,dS$$

$$+ \frac{1}{4\pi}\int_{\partial V} D\left\{\frac{1}{r r_0 \alpha}\frac{\partial r_0}{\partial n} + \frac{1}{r r_0 \alpha}\frac{\partial r}{\partial n}\right\} f'(t-t_0-t_1)\,dS . \qquad (1.9)$$

This equation is similar to those derived by Trorey (1970, 1977), Hilterman (1970, 1975), and Berryhill (1977). These authors have derived convolutional forms of the Kirchhoff integral which make computation rapid. Hilterman (1970) has verified his results with small scale experimental modeling of a point source in air impinging on rigid anticlines, synclines, and normal faults. The agreement between his numerical calculations and experiments is, in general, excellent. However, these analytical forms of the solution place restrictions on either the source-receiver geometry or the surface geometry.

The method presented in this chapter differs from those of Trorey (1970) and Hilterman (1970, 1975) in that the source and receiver are allowed to separate, the surface geometry is arbitrary, and the integral is approximated by the following expression

$$\varphi_r(\underline{\varepsilon},t) = \frac{1}{4\pi}\sum_{k=1}^{N} D\left\{f(t-t_o-t_1)Q_k^{(A)} + f'(t-t_o-t_1)Q_k^{(B)}\right\}\Delta S_k \qquad (1.10)$$

where

$$Q_k^{(A)} = \frac{1}{rr_0^2}\frac{\partial r_0}{\partial n} + \frac{1}{r_0 r^2}\frac{\partial r}{\partial n}$$

and

$$Q_k^{(B)} = \frac{1}{rr_0\alpha}\frac{\partial r_0}{\partial n} + \frac{1}{rr_0\alpha}\frac{\partial r}{\partial n}.$$

An important part of the procedure is the discretization of the surface. The rough surface is specified by a function $z(x_i,y_i)$ where (x_i,y_i) is a location on

a horizontal grid of regularly spaced points separated by a distance Δx and Δy. A schematic diagram is shown in Figure 1.1. In all the following calculations, $\Delta x = \Delta y$. From this information, one can readily calculate $\frac{\partial z}{\partial x}$ and $\frac{\partial z}{\partial y}$. Then the following formulae are used to calculate ΔS_k, $\frac{\partial r_0}{\partial n}$, and $\frac{\partial r}{\partial n}$:

$$\Delta S = \sqrt{1 + (\frac{\partial z}{\partial x})^2 + (\frac{\partial z}{\partial y})^2}\, \Delta x \Delta y \tag{1.11}$$

$$\frac{\partial r}{\partial n} = \frac{\left[(x_s - x_i)\frac{\partial z}{\partial x} + (y_s - y_i)\frac{\partial z}{\partial y} - (z_s - z_i)\right]}{r\sqrt{1 + (\frac{\partial z}{\partial x})^2 + (\frac{\partial z}{\partial y})^2}} \tag{1.12}$$

$$\frac{\partial r_0}{\partial n} = \frac{\left[(x_0 - x_i)\frac{\partial z}{\partial x} + (y_0 - y_i)\frac{\partial z}{\partial y} - (z_0 - z_i)\right]}{r_0\sqrt{1 + (\frac{\partial z}{\partial x})^2 + (\frac{\partial z}{\partial y})^2}} . \tag{1.13}$$

Here x_s, y_s, and z_s are the station coordinates and x_0, y_0 and z_0 are the source coordinates. The integral (1.9) is calculated for a finite surface. However, the Kirchhoff integral is formally stated for a closed surface. This problem is circumvented by integrating over a closed surface consisting of the part of the surface one is interested in (S_α) and a portion of a sphere of large radius (S_β), shown in Figure 1.2. One then argues that the contributions from the infinitely large sphere vanish because of the radiation condition.

We wish to evaluate the response at a receiver for an input source function of a unit ramp function, the integral of a unit step function. We choose a ramp function to circumvent the problem of numerically simulating a delta

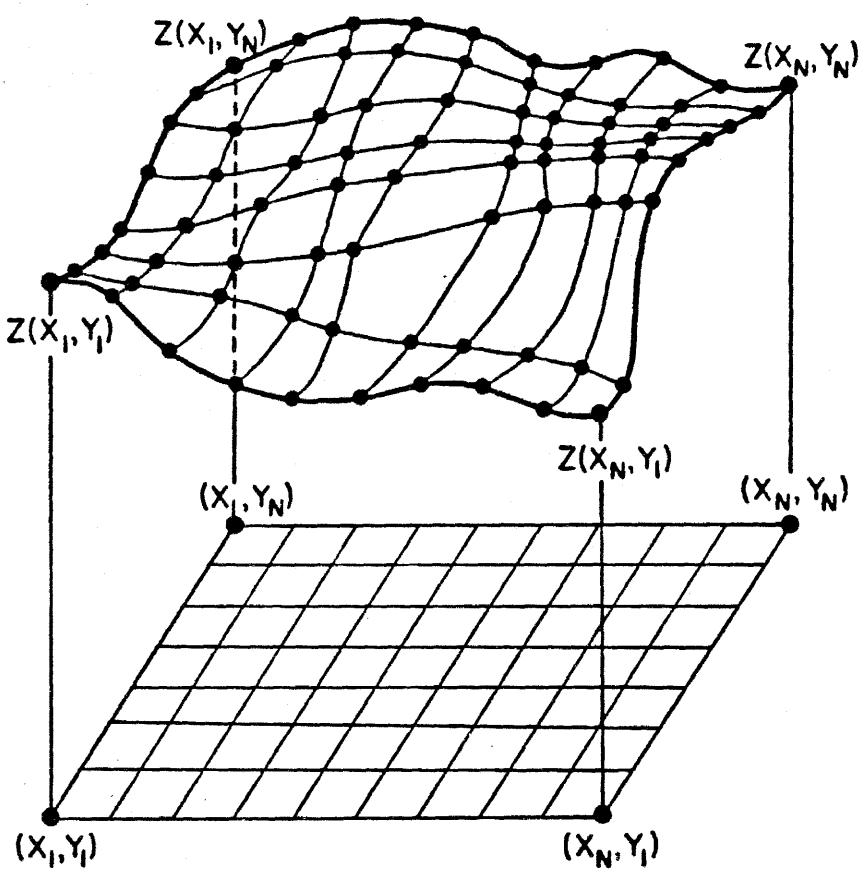

Figure 1.1. The discretization of the surface over which the Kirchhoff integral is calculated.

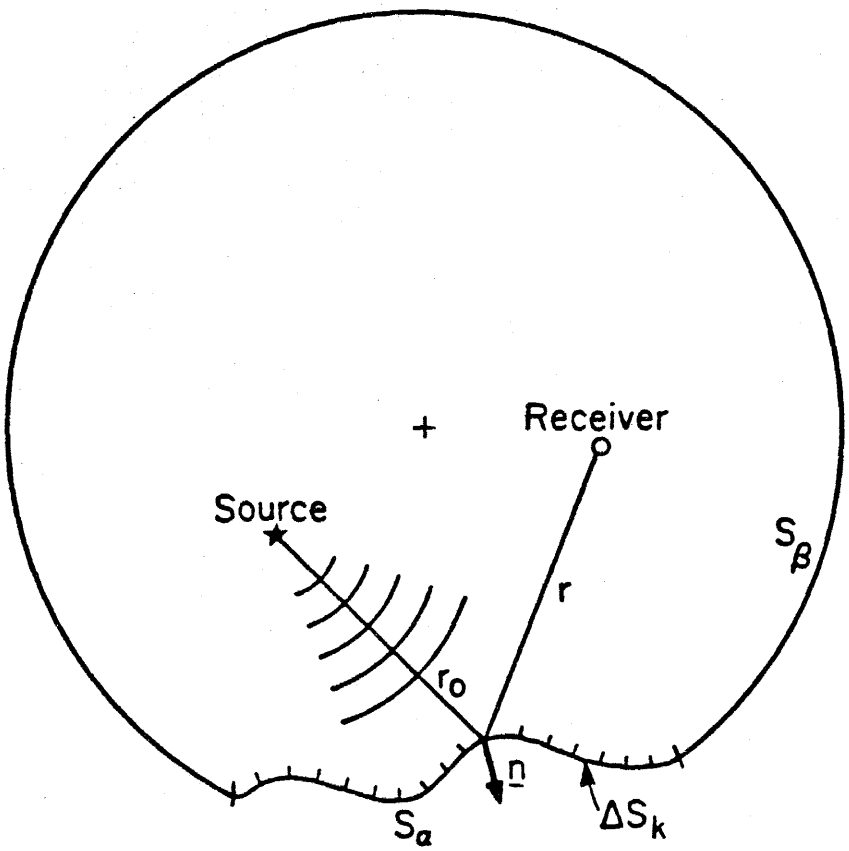

Figure 1.2. The closed surface of integration composed of S_α, the surface over which one integrates, and S_β, the remainder. Also shown are the source and receiver positions and the normal.

function. According to equation (1.10) we must sum two contributions from each point, one which is multiplied by the source function and one which is multiplied by the derivative of the source function. To implement this calculation we specify a step function on each element and multiply by the $Q_k^{(A)}$ and $Q_k^{(B)}$ terms of each element. We sum the two terms independently. Each element is illuminated and contributes to the Kirchhoff synthetic at a time $\tau = \frac{(r + r_0)}{\alpha}$. The two-way travel time is calculated for each point and sorted in order of increasing τ. Each of the two terms are then summed appropriately in time. We define the two summed parts of the solution which correspond to the $Q_k^{(A)}$ and $Q_k^{(B)}$ as Φ_A and Φ_B, respectively. We integrate Φ_A and add this integrated time function to Φ_B to obtain the final ramp response. A schematic diagram which demonstrates the summation process is shown in Figure 1.3.

For problems presented in this chapter, the numerical ramp response is convolved with the analytical third derivative of a Haskell explosion source function , specifically

$$\Psi(t) = \Psi_0\left[1-e^{-kt}\left[1 + kt + \frac{(kt)^2}{2} + \frac{(kt)^3}{6} - B(kt)^4\right]\right] . \qquad (1.14)$$

Here Ψ_0 is the source strength. B is a dimensionless overshoot parameter and determines the step- like or impulse-like nature of the source. The parameter k determines pulse width and rise time of the source and has units of sec^{-1} (Given and Helmberger, 1980). We set Ψ_0 equal to 1 and only vary B and k in the ensuing numerical experiments. The convolution is

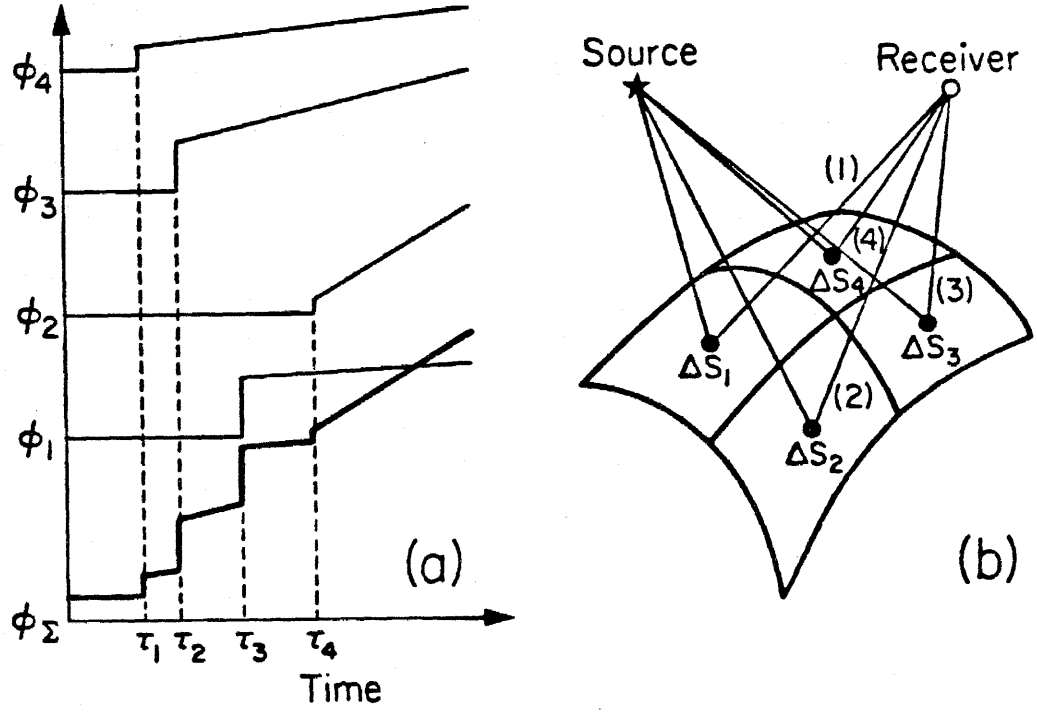

Figure 1.3. The summation of the response from each element to obtain the total response.

mathematically equivalent to the first derivative of the reflected potential caused by a source described by (1.14). From trial and error, we find that such a convolution eliminates the spikiness introduced by simple differencing and, therefore, is the preferred method for differentiation in these calculations.

We have carried out experiments to determine the grid size required to produce a smooth seismogram. As an example we show, in Figure 1.4, the variation of the waveform and maximum amplitude of a seismogram as a function of grid size for a sample reflection problem. The reflecting flat surface is specified for seismograms A, B, and C by grid areas of a wavelength of 4 kilometers. Hence for seismograms A, B, and C the number of grids per wavelength is 11.4, 8, and 4, respectively. Seismogram C shows that the coarse discrimination of the surface has introduced high frequency noise which degenerates the waveform and the maximum amplitude. For each problem we calculate, the grid size is selected by trial and error. The grid is made progressively finer until the solution is unvarying as shown in Figure 1.4.

Applications

The development of any numerical procedure necessitates comparisons with known analytic solutions. We first compare results from this code with an analytical formula derived by Hilterman (1975). This comparison establishes that we do indeed evaluate the Kirchhoff integral correctly. Hilterman reduces the Kirchhoff integral to a simple convolution product when the

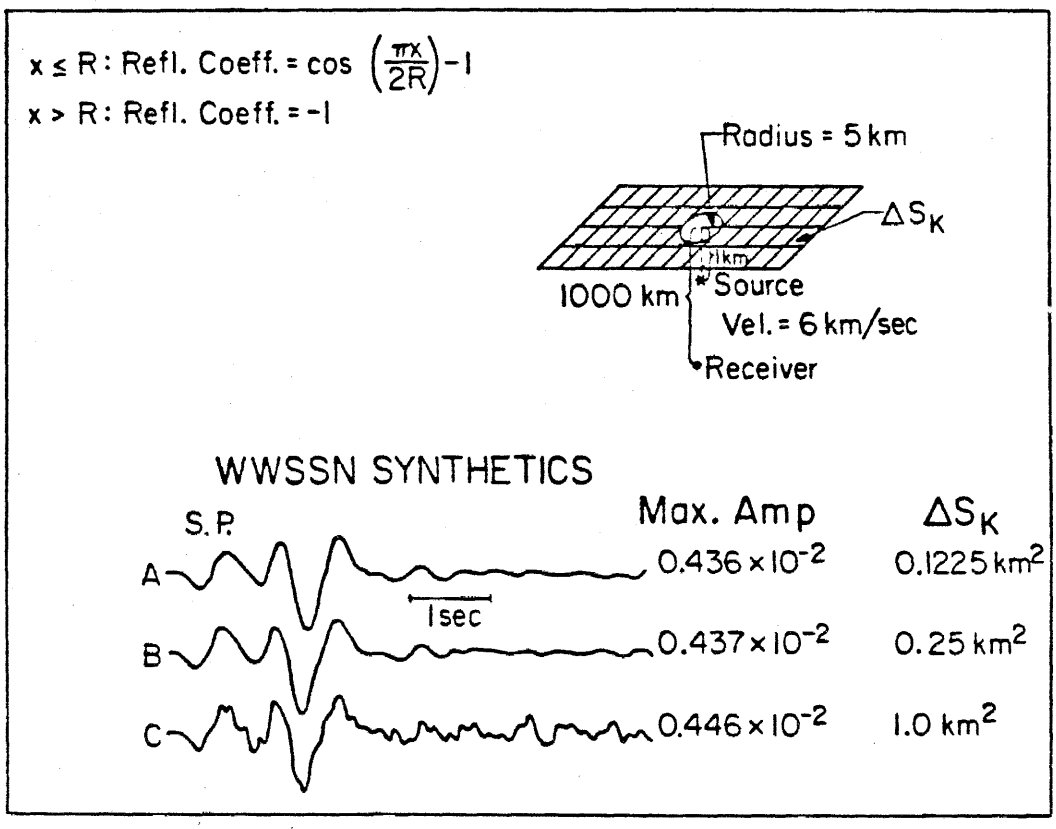

Figure 1.4. This figure shows the change of response as the element size increases. The model used here is a free surface with a hole. The source and receiver are directly below this hole. The response is convolved with a modified Haskell source and a short period WWSSN instrument to produce these seismograms.

source and receiver are coincident. This expression is

$$\varphi_r(\underline{\xi},t) = \frac{1}{2\pi\alpha}\left[\left[f(t)*\frac{2}{t}\frac{d\Omega}{dt}\right] + \left[\frac{df}{dt}*\frac{d\Omega}{dt}\right]\right]. \qquad (1.15)$$

Ω is the solid angle subtended at the source-receiver point by the wavefront intersection with the surface. Hilterman defines $\frac{d\Omega}{dt}$ the wavefront sweep velocity. We use this expression to verify that Φ_A and Φ_B are calculated correctly by the code. We calculate Φ_A and Φ_B for a source-receiver point in a fluid over a rigid hemisphere of radius a imbedded in a rigid infinite plane. The source-receiver point is at a distance R above the center of the grid. The surface geometry and the source-receiver location are shown at the top of Figure 1.5. For this configuration we derive an expression for the wavefront sweep velocity. It is

$$\frac{d\Omega}{dt} = \frac{\pi}{R}\left\{\frac{2(R^2-a^2)}{\alpha t^2} - \frac{\alpha}{2}\right\} H(t-\tau_0) \text{ for } \tau_0 \le t < \tau_1 \qquad (1.16)$$

on the hemisphere and

$$\frac{d\Omega}{dt} = \frac{4\pi R}{\alpha t^2} H(t-\tau_1) \text{ for } \tau_1 \le t \qquad (1.17)$$

on the planar part of the boundary. Here $\tau_0 = \frac{2(R-a)}{\alpha}$, the minimum two-way travel time, and $\tau_1 = \frac{2(R^2+a^2)^{1/2}}{\alpha}$. H(t) is the unit step function. We substitute a unit step function for $f(t)$ in the first term of equation (1.15) to obtain an analytical expression for Φ_A. (Recall that Φ_A is the $Q_k^{(A)}$ summed response before integration.) The convolution product of the first term of

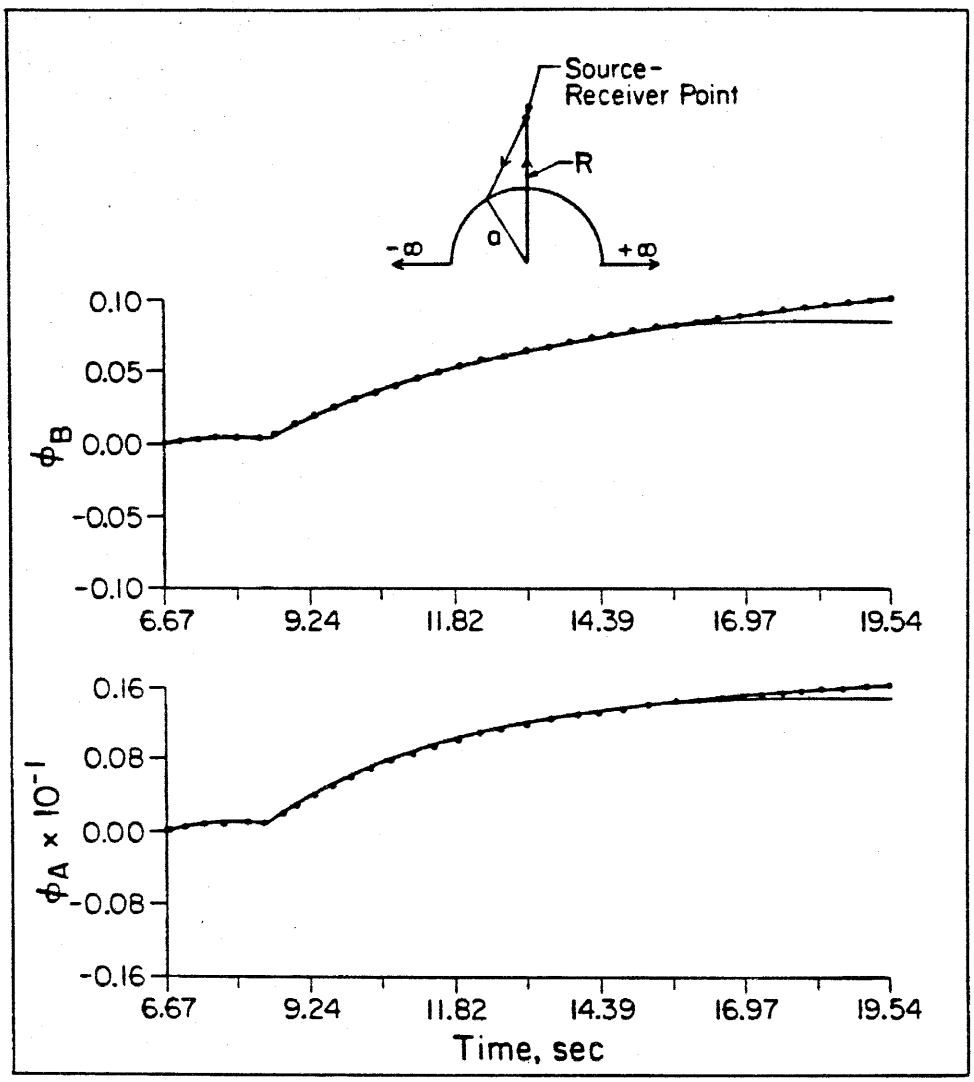

Figure 1.5. The geometry of the spherical test. a is the radius of the hemisphere and is equal to 5 kilometers. R is the distance from the source-receiver point to the center of the grid and is equal to 25 kilometers. The two parts of the solution Φ_A and Φ_B are shown below the geometry. The dotted line is the analytical solution. The solid line is the numerical solution.

equation (1.15) amounts to a simple integration of $\frac{1}{\pi\alpha t}\frac{d\Omega}{dt}$. We obtain

$$\Phi_A = \frac{(R^2-\alpha^2)}{\alpha^2 R}\left(\frac{1}{\tau_o^2} - \frac{1}{t^2}\right) + \frac{1}{2R}\ln\left(\frac{\tau_o}{t}\right) \text{ for } \tau_o \le t < \tau_1 \qquad (1.18)$$

and

$$\Phi_A = \frac{1}{2R} - \frac{2R}{\alpha^2 t} \text{ for } \tau_1 \le t \ .$$

Similiarly we substitute a step function for $\frac{df}{dt}$ in the second term of equation (1.15) to obtain Φ_B, yielding

$$\Phi_B = \frac{1}{\alpha} - \frac{1}{R}\left(\frac{(R^2-\alpha^2)}{\alpha^2 t} + \frac{t}{4}\right) \text{ for } \tau_o \le t < \tau_1 \qquad (1.19)$$

and

$$\Phi_B = \frac{1}{\alpha} - \frac{2R}{\alpha^2 t} \text{ for } \tau_1 \le t \ .$$

The comparison is shown in Figure 1.5. In this calculation, the source-receiver point is 20 kilometers above the top of the hemisphere with a radius of 5 kilometers. The velocity of the medium is 6 km/sec. The agreement is good for τ_0 + 15 seconds. The results differ because the integral is calculated numerically over a finite surface. The conclusion from this experiment is that the numerical evaluation of the integral is adequate.

We further test the code by comparing the Kirchhoff solutions with analytical high frequency solutions. Again we calculate the reflected potentials from a point source impinging on a rigid sphere; however, the source

and receiver are allowed to separate. The numerical results are compared to those from a first-motion approximation of a transform solution obtained by Gilbert and Helmberger (1972). They obtain the following solution for a reflected SH pulse from a fixed and rigid sphere:

$$u = \frac{-f(s)s^{1/2}}{2\pi\mu(2\pi r r_0 \sin\Delta)^{1/2}} \operatorname{Im} \int_C^{c+i\infty} \frac{\gamma^{1/2}\exp[-s(\gamma\Delta + \Psi)]d\gamma}{(\frac{r_o^2}{\beta^2} - \gamma^2)^{1/4}(\frac{r^2}{\beta^2} - \gamma^2)^{1/4}} . \quad (1.20)$$

u and $f(s)$ are the Laplace transforms of $u(r,\Delta,t)$, the time domain SH displacement, and $f(t)$, the source time function. β is the shear wavespeed ($\beta = \frac{\sqrt{\mu}}{\rho}$). The variable γ has the interpretation of a spherical rav parameter at the geometric arrival time. Ψ can be thought of as an intercept time. The path of integration C in the complex γ plane is the standard Cagniard path and is displayed in Gilbert and Helmberger (1972). Helmberger evaluates this expression at the geometric arrival time and obtains (Helmberger, pers. comm., 1979)

$$u = \frac{-1}{4\pi\mu}\left[\frac{a(\cos e)(\sin i)}{\sin\Delta r_o(R_0 r\cos i + R r_0 \cos i_0)}\right]^{1/2} f\left[t - \left[\frac{R_0 + R}{\beta}\right]\right] . \quad (1.21)$$

Figure 1.6 defines the angles and lengths of this solution.

If the source and receiver are together we can show that the spreading factor in solution (1.21) and a spreading factor for a spherical surface obtained from the Kirchhoff integral are identical. Taking the limit of the spreading factor in equation (1.21) as R approaches R_o and Δ approaches 0 yields

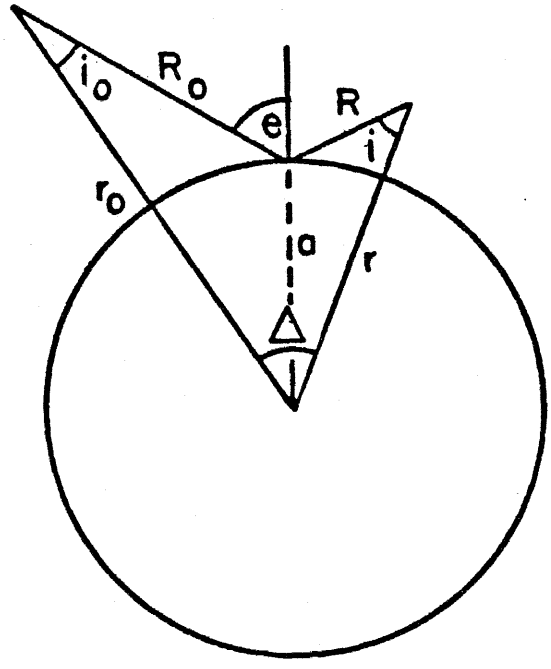

Figure 1.6. Geometry of Helmberger's first-motion spherical solution.

$$S = \frac{a}{2(R_o + a)R_o} \cdot \tag{1.22}$$

Now we examine the Kirchhoff solution when the source and receiver are together. Following an approach developed by Hilterman (1975), the first term in equation (1.15) is discarded as a near-field term.

$$\varphi_r \approx \frac{1}{2\pi a}\left\{\frac{\partial f}{\partial t} * \frac{d\Omega}{dt}\right\} . \tag{1.23}$$

Then a first-motion approximation is made.

$$\frac{d\Omega}{dt} \approx \frac{d\Omega}{dt}\Big|_{t=\tau_0} H(t-\tau_0) . \tag{1.24}$$

Substitution of the value of $\frac{d\Omega}{dt}$ at τ_o into equation (1.23) yields

$$\varphi_r = \frac{a}{2(R_0+a)R_0} f(t-\tau_0) . \tag{1.25}$$

Hence, the Kirchhoff integral yields the correct spreading factor associated with a spherical surface when the source and receiver are together. A similar result is obtained by Hilterman (1975) for a rigid planar surface.

We demonstrate the same result numerically for the source and receiver separated. The maximum amplitudes of the synthetic reflections from a sphere are compared with those amplitudes predicted by the spreading factor in equation (1.21). The time function of the input source for this problem is the third derivative of equation (1.14) with the overshoot constant B = 2 and k = 10. The medium has a wave velocity of 5 km/sec; thus, the

wavelength of the input source is approximately 4 kilometers. The grid length used in these calculations is .1 kilometer, making the number of grids per wavelength equal to 40. The total grid area needed to describe the surface of the sphere is 400 square kilometers. The grid length was selected to give an extremely fine sampling of the surface so that we may investigate the effects of a wide range of pulse widths as input time histories. Six ramp responses for this problem required 595.8 seconds of CPU time on a PRIME750. Table 1.1 shows the parameters used in these numerical experiments and the numerical and theoretical amplitudes. The results compare favorably.

Table 1.1

R (km)	R_e (km)	i deg	Kirchhoff amp.	optics amp.
90.6	90.6	6.3	.02404	.02467
92.2	92.2	12.5	.02320	.02383
94.9	94.9	18.4	.02202	.02257
42.3	95.2	18.9	.04567	.04667
17.5	105.2	31.0	.07967	.08218
55.9	55.9	26.5	.08914	.09163
128.1	128.1	38.6	.01228	.01267
62.5	62.5	36.8	.07253	.07461

The above two experiments indicate that the Kirchhoff code correctly predicts reflections from curved surfaces with large reflection coefficients and far field receivers. Similar efforts have been carried out by workers in the field of electromagnetic scattering. Jiracek (1972) computes the amplitudes of electromagnetic waves caused by an incident transverse electric plane wave impinging on a perfectly conducting two-dimensional sinusoidal surface. He compares results obtained from a Rayleigh-FFT method, an integral equation solver, and the Kirchhoff method. The most obvious failure

of the Kirchhoff technique to predict correct amplitudes occurs when the incident angle is past critical angle. This result is not surprising in light of assumptions made in estimating the boundary values on the surface. However, for angles less than critical, the Kirchhoff code is adequate and inexpensive for problems involving three-dimensional rough surfaces.

We can gain further insight into the usefulness of this formalism by comparison of the Kirchhoff solutions with optical solutions to problems of geophysical interest. First, the technique is applied to the calculation of reflections from a mountain with a buried source. In the second application, reflections from a plane where the reflection coefficient varies as a function of position on the surface are computed. In both calculations, particular attention will be paid to those propagation paths where classical ray theory fails.

The first application of the code is the calculation of the reflected potentials from an isotropic source underneath an idealized mountain. The topography of the mountain is calculated as follows:

$$z = \frac{c}{2}\left\{1 - \cos\left[\frac{2\pi}{w}\left[(x^2 + y^2)^{\frac{1}{2}} - \frac{w}{2}\right]\right]\right\} . \qquad (1.26)$$

Here c, the maximum height, is 5 kilometers, and w, the width, is 33.33 kilometers. The acoustic reflection coefficient is -1 everywhere on the surface. The topography is specified on a 150 x 150 kilometers grid where each element of the grid is 0.5 kilometers long.

Since the angle between the normal to the surface and the incident source ray is calculated by the code, it is simple to plot the path of the reflected rays. These rays are traced for two depths below the baseline of the free surface. In the first plot, Figure 1.7, we can see the rays from a source at 10 kilometers which reflect off the free surface and travel to a depth of 50 kilometers. This figure shows the position of the ray caustic, focii, and the shadow zone caused by the convex shape of the mountain. These features will influence the waveforms considerably.

In Figure 1.8 the rays are traced to a depth of 1000 kilometers. The Kirchhoff responses are calculated at this depth at the marked positions which range from 0 to 750 kilometers horizontally. Upon closer inspection of Figure 1.8, one can see slight asymmetries in the location of the rays with respect to the position at 0 kilometers. These asymmetries are caused by the discretization of the surface of the mountain. The error in the value of the computed normal derivatives introduces about 10 kilometers of uncertainty into the location of the rays at this depth.

The calculated reflected responses are shown in Figure 1.9. These pulses are convolutions of the ramp response with the Haskell function with the parameter B=0 and k=25. Hence, the number of grids per wavelength is 10. As the horizontal distance of the receiver changes, we see systematic waveform variations which can be interpreted in terms of rays interacting with caustics. In the ranges of 0, 50, 100, and 150 kilometers the synthetics have complicated pulse shapes caused by the interference of three families of rays. The first arrival is a simple pulse with a π phase shift which is a

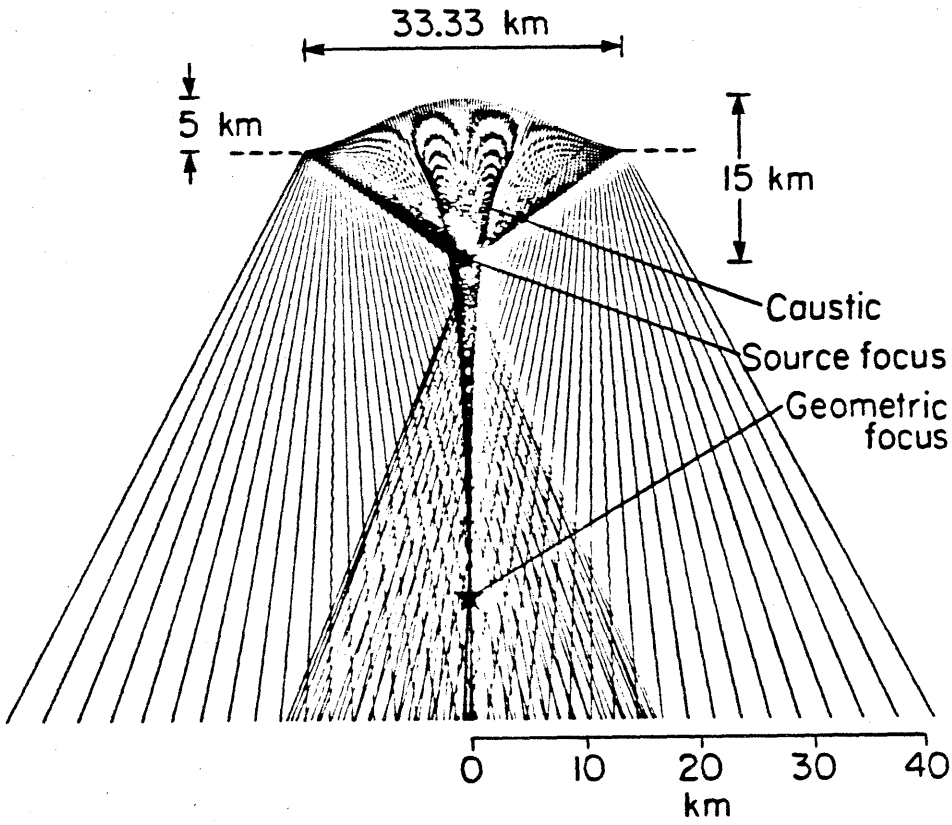

Figure 1.7. The rays which reflect off a mountain described by the equation (1.26) traced to a depth of 50 kilometers. The source is 10 km below the baseline indicated by the dashed line. Also shown are the caustics and the geometric focus formed by the mountain.

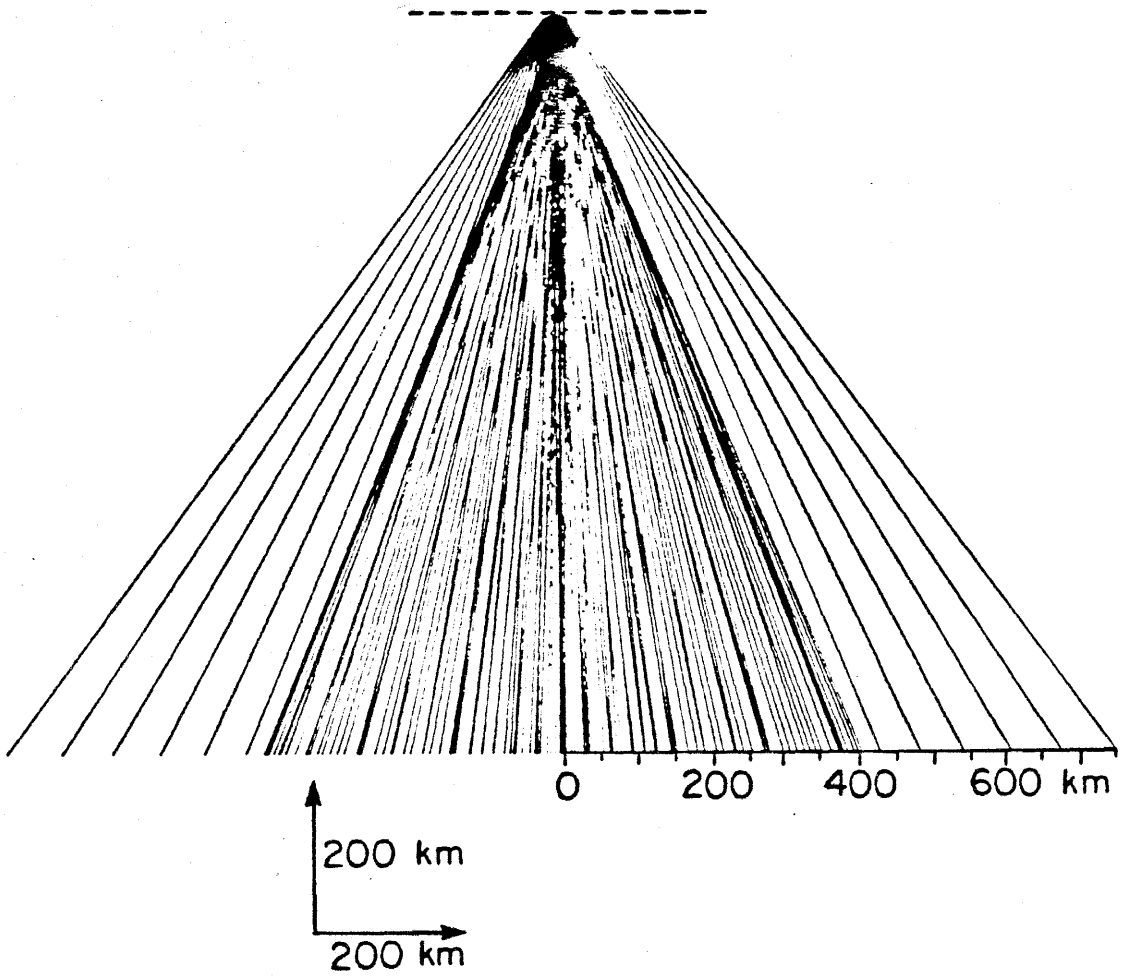

Figure 1.8. The rays traced to a depth of 1000 km.

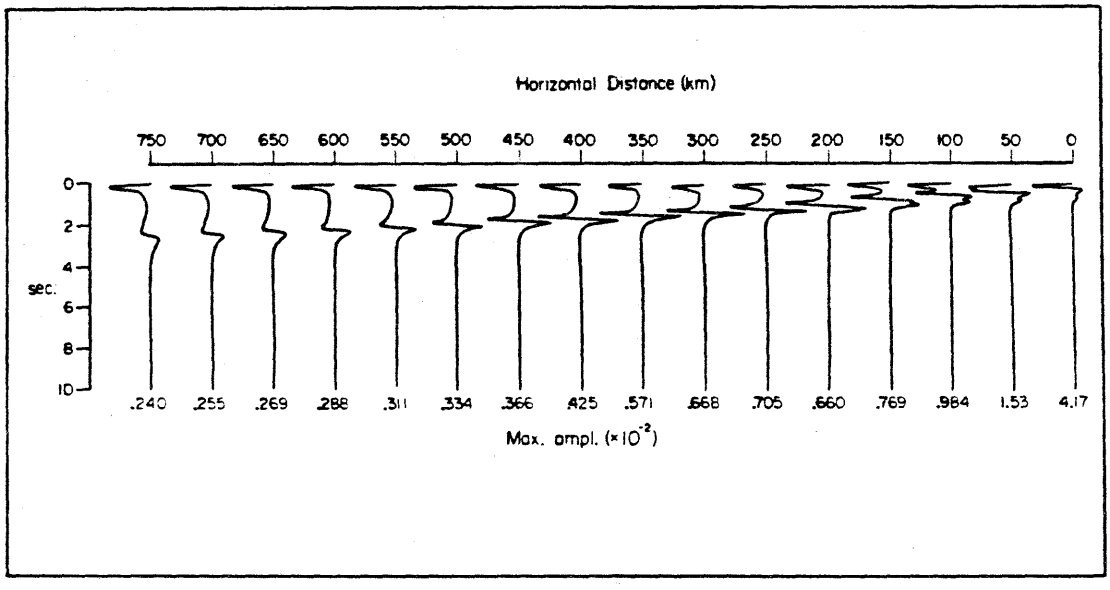

Figure 1.9. The responses convolved with a modified Haskell source for receivers at a depth of 1000 kilometers and at horizontal distances ranging from 0 to 750 kilometers away from the center.

consequence of the reflection off the free surface. The second pulse is a reflected ray with a path which is tangent to the caustic formed by the mountain. This path results in a $\pi + \pi/2$ phase shift of the pulse. The third arrival reflects off the mountain and travels through the geometric focus caused by the mountain; thus, the phase shift of this arrival is $\pi + \pi$. The maximum amplitude of these four distances is controlled by the interference of these rays. Clearly the high amplitude and the simple pulse of the first synthetic at 0 kilometers is a result of the constructive interference of the first two rays. Past 150 kilometers, the latter two arrivals arrive closely in time and their interference controls the amplitude and frequency content of the second pulse on the record. From Figure 1.8 , it is clear that a ray interpretation of pulses on records past 400 kilometers is no longer valid. Ray theory predicts only one reflected pulse because the mountain creates a shadow zone; yet one sees two distinct pulses predicted by the Kirchhoff method. The second phase shifted pulse decreases in amplitude and frequency content. As the horizontal distance of the receivers increases, the amplitude of the first reflection becomes the maximum amplitude of the record. If one calculates the maximum amplitudes of reflections off a plane for the same source-receiver geometry, one can see that the two sets of amplitudes merge. This behavior is shown in Figure 1.10 where the amplitudes as a function of horizontal distance for the two geometries have been calculated. The solid line shows the decay of amplitudes calculated for a planar surface. The triangles are amplitudes calculated for a mountain with a height of 2 kilometers and a width of 10 kilometers. The two sets of values

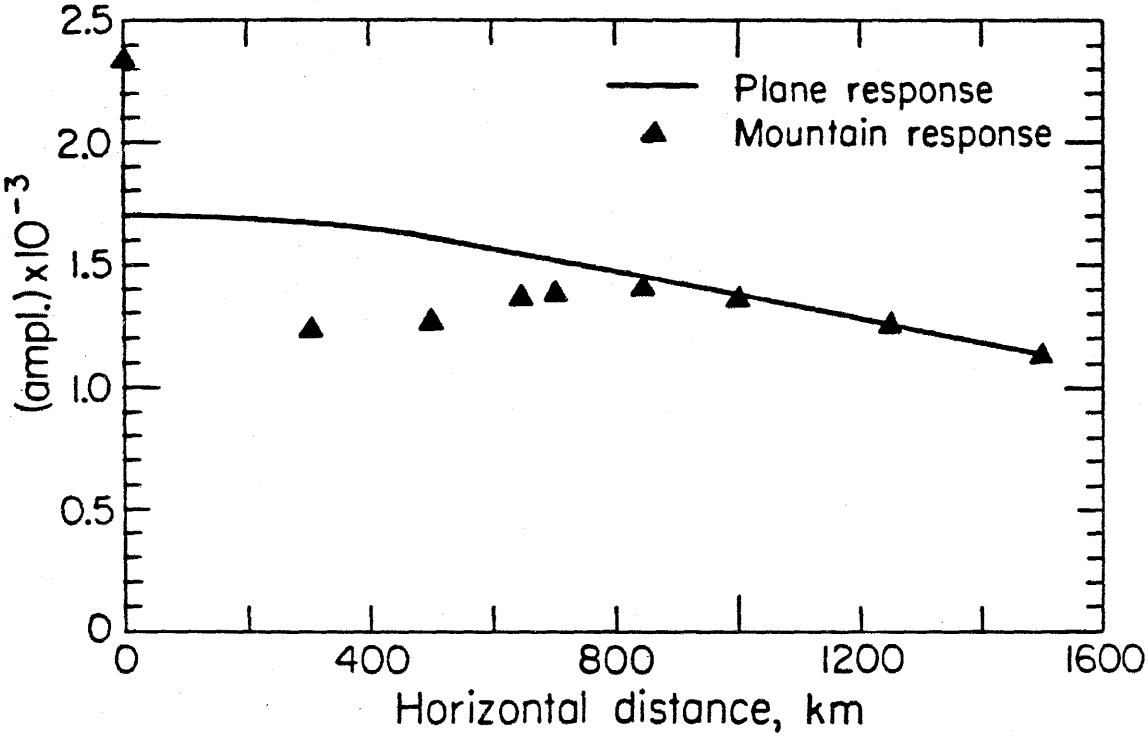

Figure 1.10. The maximum amplitude of the computed reflections from a planar surface (solid line) and a 2 kilometer high and 10 kilometer wide mountain (triangles), shown as a function of horizontal distance from the center of the grid. The source is 10 kilometers below the baseline. The receivers are at a depth of 1000 km.

coincide past 800 kilometers.

The Kirchhoff results for this experiment are gratifying because this technique nicely circumvents the infinite amplitudes or abrupt shadow zones predicted by optics. This experiment also demonstrates that this technique produces the requisite phase shifts in an extremely simple manner, unlike existing ray tracing techniques which must track the behavior of a ray tube along the propagation path.

The second application of the code is the calculation of reflections off an acoustic planar free surface where the reflection coefficients are allowed to vary as a function of position on the surface. These calculations demonstrate the flexibility of the code and again emphasize the differences between the Kirchhoff solution and optics. The wavespeed of the medium is 6 km/sec for all the following calculations.

Initially the reflection coefficient is zero for elements of the plane within a circular aperture of radius R and is -1 for elements outside this aperture. The source is directly underneath the center of the hole. From ray theory one expects that no reflected energy will arrive at a receiver directly underneath the source. Yet one calculates non-zero amplitudes for both long and short period WWSSN seismograms from the Kirchhoff code. These synthetics are displayed in Figure 1.11 as a function of the radius of the aperture for a receiver 1000 kilometers below the surface. Only the reflections are shown.

This pulse is systematically delayed as the radius of the hole increases from 1 to 5 kilometers. There is no change in the waveforms. Only the amplitudes of both sets of seismograms decrease. However, the amplitude of

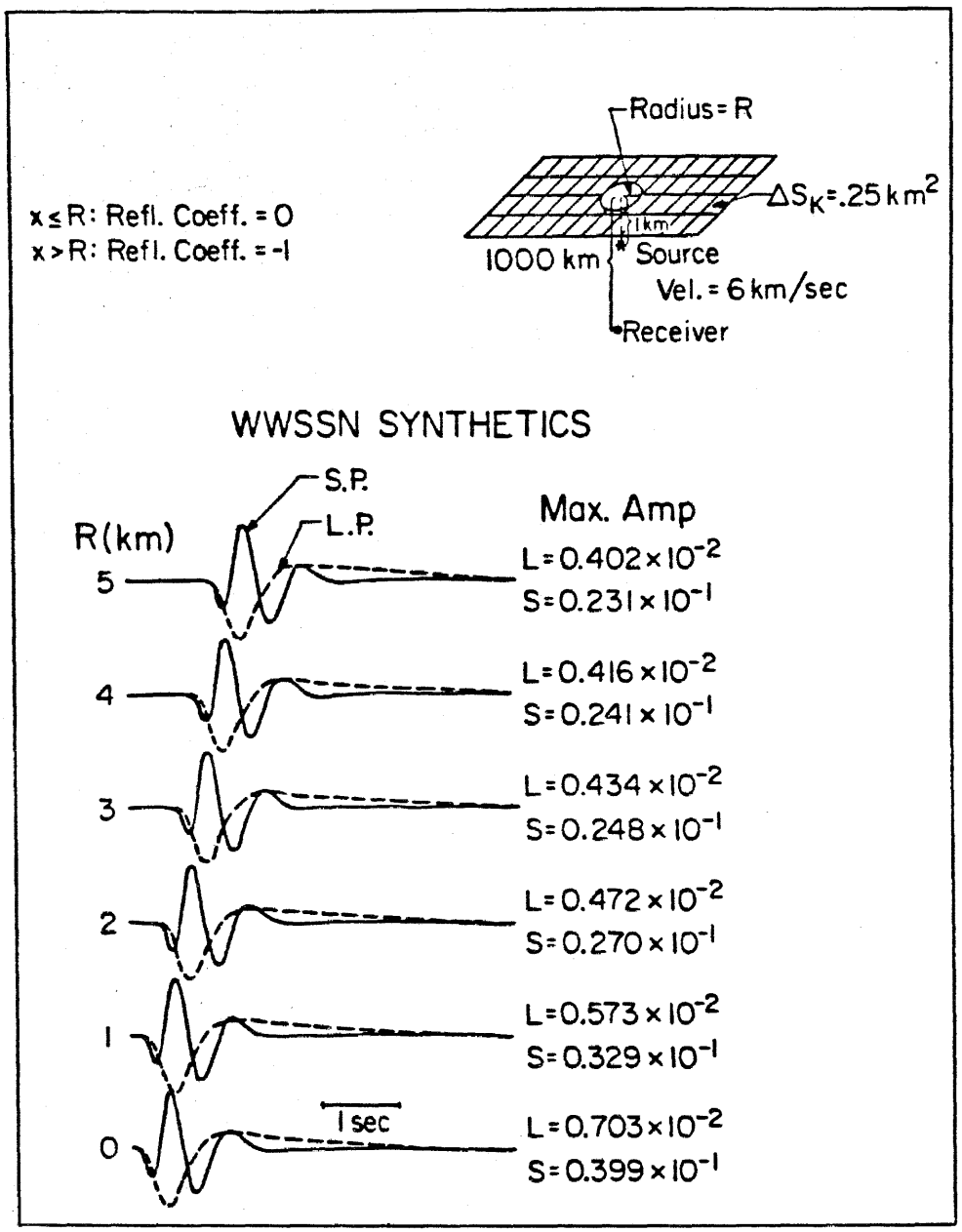

Figure 1.11. Long (dashed lines) and short (solid lines) period WWSSN seismograms calculated for the geometry shown at the top of the figure. The radius of the hole varies from 1 to 5 km.

reflections off an aperture with a five kilometer radius is more than half the magnitude of the reflections from a free surface without a hole. Clearly ray theory is not a good approximation to the solution to this problem.

In addition, ray theory fails to predict any dependence of the reflected amplitudes on frequency. Intuitively one expects, for an aperture problem, that the higher frequencies of a broad band signal will be reduced relative to the lower frequencies after reflection. This hypothesis is tested by calculating the reflected responses from sources of differing frequency content. In the following calculations the parameter B of the modified Haskell source representation equals zero; however, k varies from 5 to 25. An increase in k broadens the bandwidth of the incident signal (von Seggern and Blandford, 1972). In this experiment, we compute two responses for a given source pulse. The first response is a reflection off the plane with a hole and the second is a reflection off the plane without a hole. The amplitude of the latter response has no frequency dependence; hence, if the reflection from a hole has no frequency dependence, one predicts that the ratio of the amplitudes of the two reflections will be independent of the parameter k. However, if there is a frequency dependence, the ratios should vary systematically with k.

Numerical experiments confirm the frequency dependence of the reflected amplitudes. The ratios are shown in Figure 1.12. Specifically, the amplitude of the reflections from the aperture are always smaller than the amplitudes of planar reflections. Also the ratio of the two responses decreases when k decreases if the receiver is located at position 2, 68

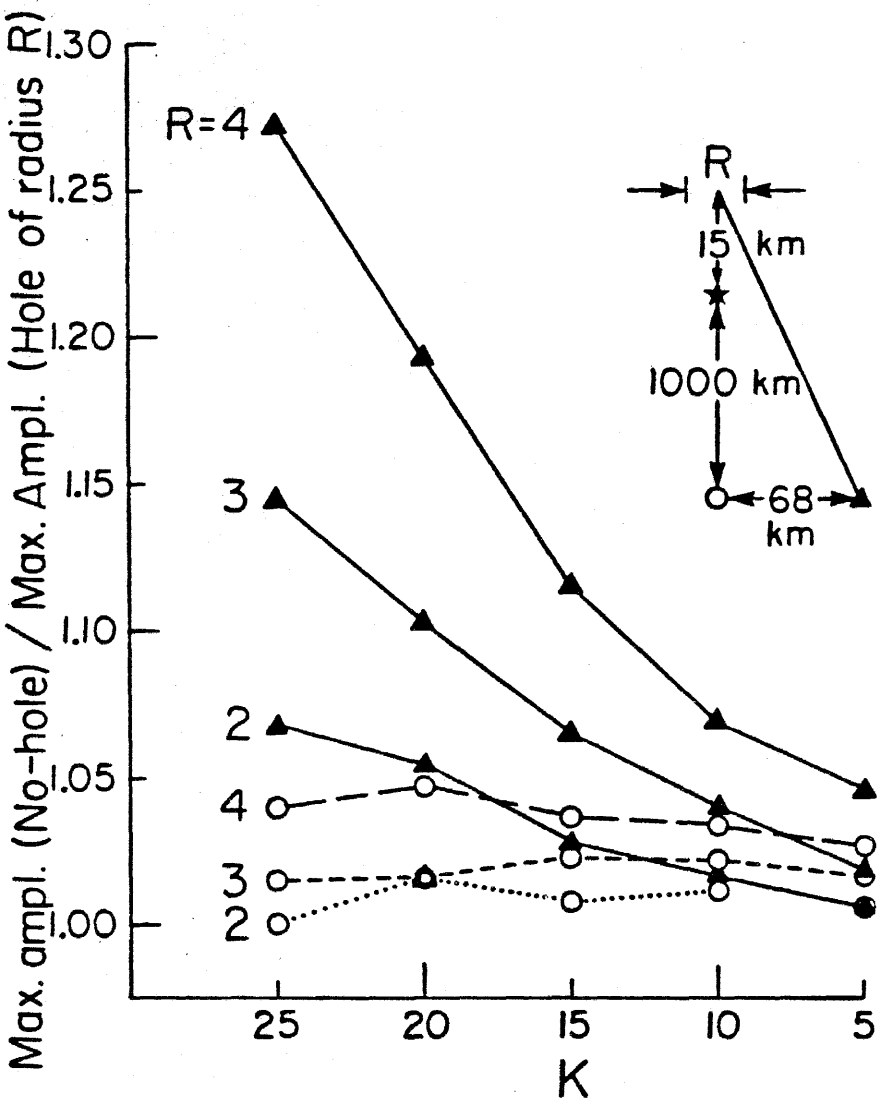

Figure 1.12. Ratio of maximum amplitude of reflections from a surface with and without a hole. The open circles are ratios measured at a receiver directly underneath the center of the aperture. The triangles are ratios measured at a receiver 68 km away from the center. The receivers are 1000 km below the free surface. The radius of the hole R is 2,3, and 4 kilometers. The ratios are plotted for these radii as a function of k.

kilometers off the center of the grid and 1000 kilometers directly below the source. This behavior is displayed for apertures with radii of 2, 3, and 4 kilometers.

However, the ratios are largely independent of k if the receiver is located at position 1, 1000 kilometers directly below the source. This observation indicates that at this position the reflected amplitudes from the aperture do not depend on the bandwidth of the signal. This result is typical of analytical solutions of Fraunhofer diffraction from apertures in an opaque screen (Born and Wolf, 1964). For example, the solution of the intensity of light transmitted through a rectangular aperture has the functional form of

$$\frac{\sin(A\omega x)}{A\omega x} \cdot \frac{\sin(B\omega y)}{B\omega y} \tag{1.27}$$

where A and B are geometric constants and x and y are the rectangular coordinates of the position of the receiver. The limit of the above function as x and y approach zero is 1 and is independent of the value of ω, the angular frequency. Clearly the interference patterns originating from the edges of the aperture cancel out due to the symmetry of the problem.

These numerical experiments, which vary the reflection coefficients on the free surface, may be applicable to the analysis of the effects of spallation generated by nuclear blasts on teleseismic P wave reflections. Spall is the physical separation of near surface layers during the explosion. Material above the bomb is either ejected or returns to produce an impact signal on near field instruments. This non-linear and non-elastic behavior of the material surrounding the source may result in amplitude and travel time

anomalies of reflected sP and pP phases.

The model used to simulate spall is one where the reflection coefficient is a cosine taper; that is,

$$D = \left[\cos\left(\frac{\pi x}{2R}\right) - 1\right] \qquad x \leq R \tag{1.28}$$

$$D = -1 \qquad x > R \ . \tag{1.29}$$

Here x is distance from the source epicenter on the free surface. One chooses this behavior of the reflection coefficient to simulate material reflecting more energy as the distance from the source increases. The model introduces complications into the short period waveforms but only broadens the long period waveforms. This effect and the source-receiver geometry is illustrated in Figure 1.13. The geometry is the same as used in the aperture calculations. Unlike the first model, this model causes the amplitudes of both the long and short period reflections to decay quite rapidly. The amplitude decay is greater for the short period reflections than for the long period reflections. Hence the long period energy is insensitive to the perturbation of the reflection coefficients relative to the short period energy.

The source-receiver geometry is changed for this particular model to test the hypothesis that asymmetries of spalling with respect to the source location can introduce observable azimuthal variations of amplitudes and waveforms of teleseismic records of nuclear blasts. Such variations have been documented for teleseismic recordings of Nevada Test Site blasts

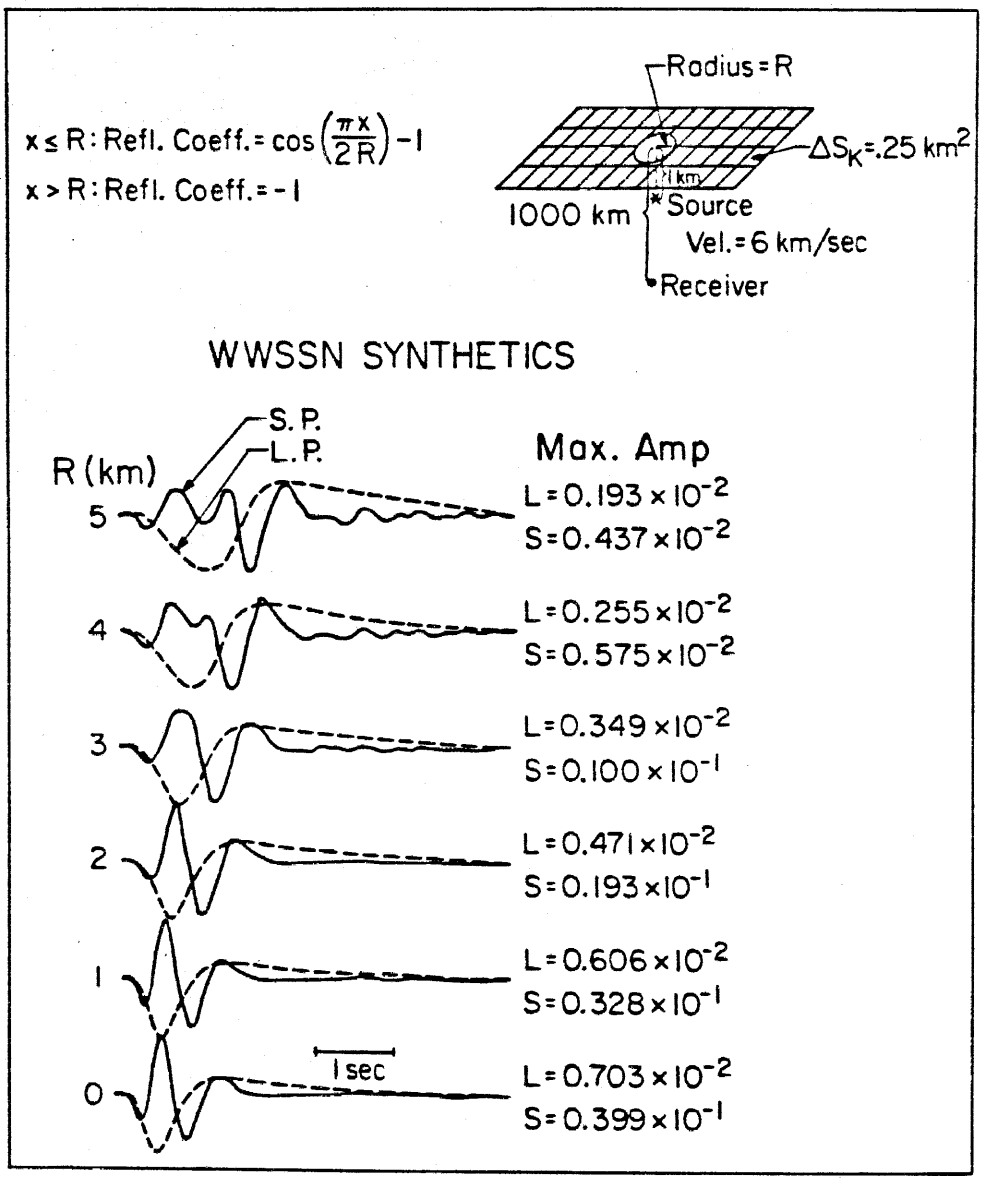

Figure 1.13. Long and short period synthetics for a cosine tapered reflection coefficient.

(Helmberger and Hadley, 1981). In addition, photographs of collapsed craters from NTS blasts suggest that processes such as spalling and subsidence occur along pre-existing planes of weakness which are not symmetrical with respect to the emplacement hole (Springer and Kinnaman, 1971). Figure 1.14 shows the results for stations at three azimuths. The source is placed 2 kilometers to the right of the center of the spall aperture and 1 kilometer below the free surface. The receivers are all at horizontal distance which corresponds to a takeoff angle of 20^0 for the direct P wave. One sees azimuthal variations of waveform and amplitudes for both long and short period reflections. The amplitude variations are not large, but the waveform changes are dramatic for short period records.

Clearly, this model is crude and one may genuinely question its relevance to the Earth. We do not simulate any conversion of P to S waves. As a consequence, our model reflects more P wave energy than is reflected for an elastic solid without a hole for incidence angles greater than 55^0 (A. Douglas, pers. comm., 1983). However, Shumway and Blandford (1980) report observing a systematic delay in arrival times of pP phases from explosions. The simple aperture experiment provides an explanation for that delay. In addition the Kirchhoff technique allows one to specify more realistic dynamical information on the free surface and calculate more realistic models in a straightforward manner.

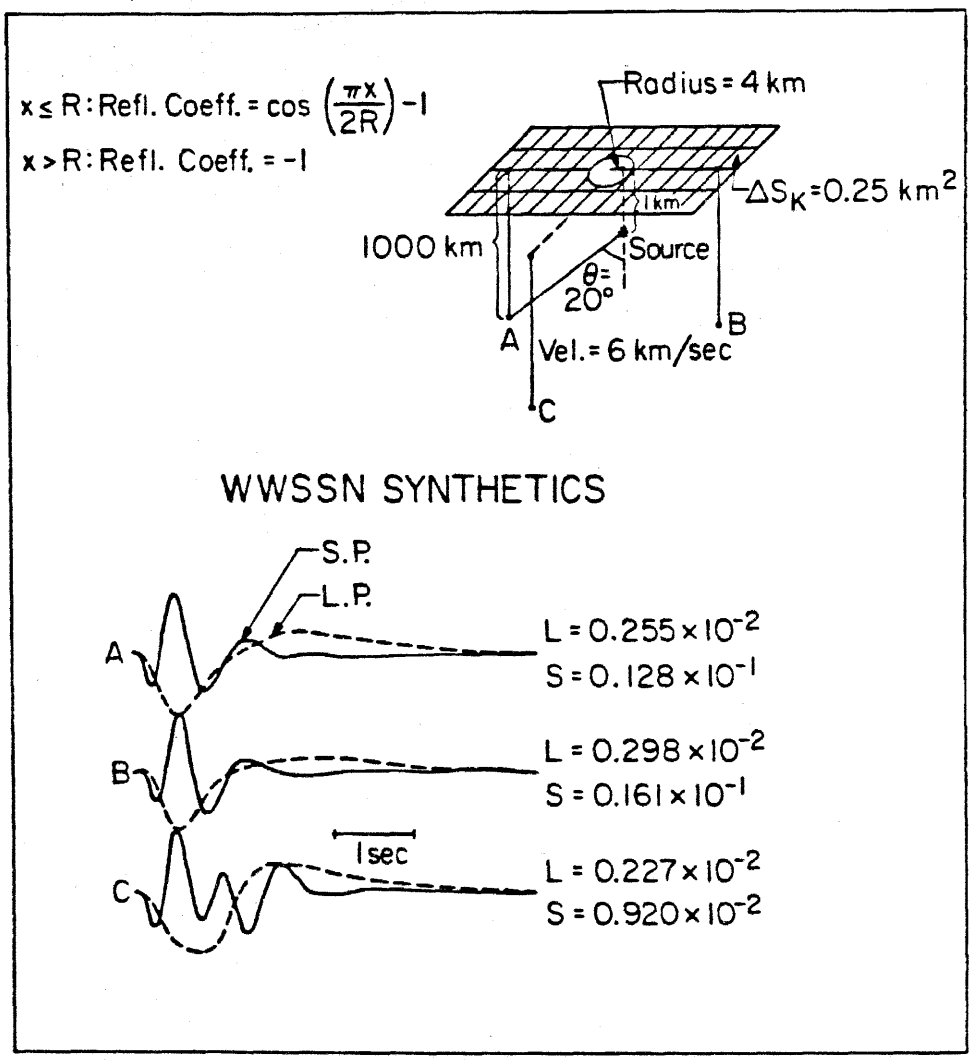

Figure 1.14. Long and short period synthetics from receivers located A, B, and C.

Conclusions

A numerical procedure has been presented for the evaluation of the Kirchhoff-Helmholtz integral assuming the tangent plane hypothesis. The method is a high frequency one and produces results which compare well with existing asymptotic first motion solutions. The technique has been applied to two problems and compared to classical ray theory results. First, the reflections off an idealized mountain are calculated and have phase shifts consistent with those predicted by optics; however, the amplitudes at triplications are finite, unlike the classical ray result. In addition, diffracted pulses are produced in the shadow zones. The second application is the calculation of reflections where the reflection coefficients vary as a function of position. For a hole in the free surface, the Kirchhoff method produces reflections where ray theory predicts no reflections. The method also produces amplitudes which are frequency dependent. The results are applied and extended to model the effects of spallation on teleseismic reflections. Travel time delays and amplitude anomalies are predicted. These anomalies are consistent with observations although the observations are not modeled.

In conclusion, the method has a broad range of applications. The method is inexpensive to run for modeling two- and three-dimensional rough surfaces. Although the method is appropriate for narrow angles of reflections and acoustic reflections, its range of applicability can be extended by assigning potentials on the boundary which are valid at critical angle. The code can be coupled with existing propagational techniques such as ray tracing, Cagniard-de Hoop methods, or full wave theory. This coupling

will enable one to handle more complicated and relevant seismological problems.

REFERENCES

Aki, K. and K. L. Larner (1970), "Surface motion of a layered medium having an irregular interface due to incident plane SH waves," J. Geophys. Res., 75, 933-954.

Berryhill, J. R. (1977), "Diffraction response for nonzero separation of source and receiver," Geophys., 42, 1158-1176.

Boore, D. M., K. L. Larner, and K. Aki (1971), "Comparison of two independent methods for the solution of wave scattering problems: response of a sedimentary basin to vertically incident SH waves," J. Geophys. Res., 76, 588-569.

Born, M. and E. Wolf (1964), *Principles of Optics*, The MacMillan Co., New York.

Claerbout, J. (1976), *Fundamentals of Geophysical Data Processing*, McGraw-Hill Book Co., New York

Cole, D. (1980), *A numerical boundary integral equation method for transient motions* (Thesis, California Institute of Technology).

Davies, H. (1954), "The reflection of electromagnetic waves from a rough surface," Proc. Inst. Elec. Eng., 101, 209-214.

Douglas, A. (1983), personal communication.

Gilbert, F. and D. V. Helmberger (1972), "Generalized ray theory for a layered sphere," Geophys. J. R. astr. Soc., 27, 57-80.

Given, J. and D. V. Helmberger (1980), "Upper mantle structure of Northwestern Eurasia," J. Geophys. Res., 85, 7183-7194.

Glover, P. and S. Alexander (1969), "Lateral variations in crustal structure

beneath Montana LASA," J. Geophys. Res., 74, 505-531.

Helmberger, D. V. (1979), personal communication .

Helmberger, D. V. and D. Hadley (1981), "Seismic source functions and attenuation from local and teleseismic observations of the NTS events Jorum and Handley," Bull. Seism. Soc. Am., 71, 51-67.

Hilterman, F. J. (1970), "Three-dimensional seismic modeling," Geophys., 35, 1020-1037.

Hilterman, F. J. (1975), "Amplitudes of seismic waves - a quick look," Geophys., 40, 745-762.

Hong, T. L. and D. V. Helmberger (1978), "Glorified optics and wave propagation in non-planar structure," Bull. Seism. Soc. Am., 68, 1313-1330.

Jiracek, G. (1972), *Geophysical studies of electromagnetic scattering from rough surfaces and irregularity layered structures* (Thesis, University of California at Berkeley).

Langston, C. (1978), "The February 9, 1971 San Fernando earthquake: a study of source finiteness in teleseismic body waves," Bull. Seism. Soc. Am., 68, 1-29.

Mitzner, K. M. (1967), "Numerical solution for transient scattering from a hard surface of arbitrary shape - retarded potential technique," J. Acoust. Soc. Am., 42, 391-397.

Mow, C. and Y. Pao (1971), *The Diffraction of Elastic Waves and Dynamic Stress Concentrations*, #R-482-PR, A report prepared for United States Air Force Project Rand.

Shumway and R. Blandford (1980), "On detecting and estimating multiple

arrivals from underground nuclear explosions," Earthq. Notes, 50, 34.

Smith, W. D. (1975), "The application of finite element analysis to body wave propagation problems," Geophys. J. R. astr. Soc., 42, 747-768.

Springer, D. L. and R. L. Kinnaman (1971), "Seismic source summary for U.S. underground nuclear explosions, 1961-1970," Bull. Seism. Soc. Am., 61, 1073-1098.

Trorey, A. W. (1970), "A simple theory for seismic diffractions," Geophys., 35, 762-784.

Trorey, A. W. (1977), "Diffractions for arbitrary source-receiver locations," Geophys., 42, 1177-1182.

von Seggern, D. and R. Blandford (1972), "Source time functions and spectra for underground nuclear explosions," Geophys. J., 31, 823-897.

Walck, M. C. and J. B. Minster (1982), "Relative array analysis of upper mantle lateral velocity variations in Southern California," J. Geophys. Res., 87, 1757-1772.

Chapter 2

Applications of the transmitted Kirchhoff-Helmholtz solution to transmitted body waves and structural effects at NTS

Introduction

Despite dramatic improvements in the level of sophistication of data analysis, seismologists still cannot deterministically predict many observed amplitude and travel time anomalies of body waves. One hypothesis to explain these anomalies is the presence of non-planar velocity discontinuities near the source or receiver such as sedimentary basins, mountains and faults. In order for us to assess the importance of these hypotheses, we need a technique for predicting the impact of near source and/or near receiver structural complexity on far field waves. In this chapter, we present such a method based on the numerical evaluation of the Kirchhoff-Helmholtz integral with use of modified tangent plane boundary conditions. This method calculates the response of a wave which is transmitted through a warped boundary between two acoustic media. It contrasts from Chapter 1 where the reflections from a warped boundary are calculated. Here we briefly describe the formalism of the Kirchhoff-Helmholtz method for the transmitted case. Then, as an example of the method, we model the observed azimuthal amplitude and travel time anomalies of short period P waves from NTS blasts as a result of a geologic structure at the Moho.

Formalism

The method in this work is based on the numerical evaluation of the Kirchhoff-Helmholtz integral equation. The formalism differs slightly from that presented in Chapter 1. Recall that we discussed the reflected wave solution; however, here, we state the Kirchhoff-Helmholtz solution for a transmitted potential. We also qualitatively discuss the assumptions involved in its use.

We wish to calculate a transmitted potential φ_2 at point $\underline{\varepsilon}$ in a homogeneous body V_2 resulting from an incident source potential located at point $\underline{x}_o$ in a homogeneous body V_1. The boundary between the two bodies is ∂V. The sound speeds and densities of V_1 and V_2 are α_1 and α_2 and ρ_1 and ρ_2, respectively. From the scalar integral representation theorem, we write the solution for φ_2 at a point $\underline{\varepsilon}$ off the boundary ∂V, within V_2, and at a time t as

$$\varphi_2(\underline{\varepsilon},t)=\int_{\partial V}[G_2(\underline{x},\underline{\varepsilon},t)*\underline{\nabla}\Phi(\underline{x},t) - \Phi(\underline{x},t)*\underline{\nabla}G_2(\underline{x},\underline{\varepsilon},t)]\cdot\underline{n}_2(\underline{x})dS \quad . \qquad (2.1)$$

Here * denotes convolution and $\cdot$ denotes a vector dot product. G_2 is the fundamental singular solution of the scalar wave equation.

$$\frac{1}{\alpha_2^2}\frac{\partial^2 G_2}{\partial t^2} - \nabla^2 G_2 = \delta(t-t_o)\delta(\underline{\varepsilon}-\underline{x}) \qquad (2.2)$$

In addition, $\underline{n}_2$ is the outward pointing normal of V_2. Φ and $\underline{\nabla}\Phi\cdot\underline{n}_2$ are the potential and the normal derivative of the potential on the surface ∂V in V_2. We display the geometry in Figure 2.1(a) for this problem.

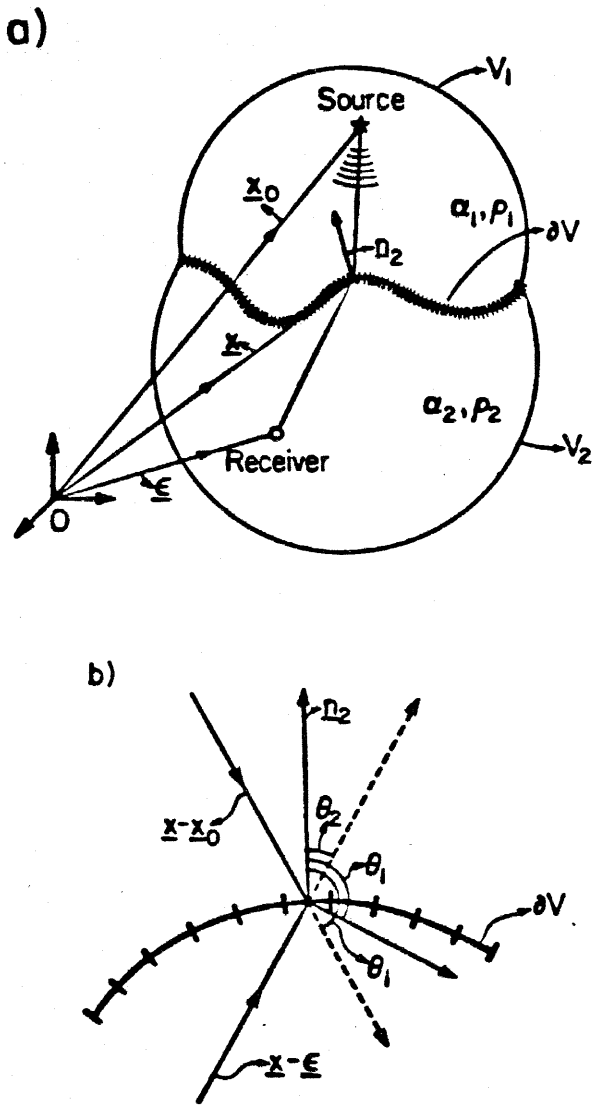

Figure 2.1. The geometry of the Kirchhoff-Helmholtz calculations for transmission across two acoustic media with sound speeds α_1 and α_2 and densities ρ_1 and ρ_2. The source is in V_1 at $\underline{x}_0$ and the receiver is in V_2 at $\underline{\epsilon}$. b) A close-up of a piece of the boundary which displays the angles.

Equation (2.1) is exact for the initial conditions that $\varphi_2(\underline{\varepsilon},0)$ and $\dot{\varphi}_2(\underline{\varepsilon},0)$ equal zero throughout V_2. The derivation can be found in Mao and Pao (1971) or Stratton (1941). To obtain equation (2.1), one requires that ∂V is a reasonably smooth surface.

We now specify G_2 and Φ. For a homogeneous medium, it is sufficient to use

$$G_2(\underline{x},\underline{\varepsilon},t) = \frac{\delta(t-\tau_2)}{4\pi|\underline{x}-\underline{\varepsilon}|};\ \tau_2 = \frac{|\underline{x}-\underline{\varepsilon}|}{\alpha_2}\ . \tag{2.3}$$

If the incident field in V_1 results from an isotropic point source at $\underline{x}_o$, then Φ is approximated by

$$\Phi = \frac{Tf(t-\tau_1)}{|\underline{x}-\underline{x}_o|};\ \tau_1 = \frac{|\underline{x}-\underline{x}_o|}{\alpha_1}\ . \tag{2.4}$$

Here T is the acoustic plane wave transmission coefficient for a flat interface and is dependent on the local incidence angle at each point. f(t) is the time function of the incident source function. The function in equation (2.4) approximates Φ well if the incident source field is of sufficiently high frequency such that every point on the surface transmits the incident pulse as though there were an infinite plane tangent to the surface at that point. Then the amplitude and the phase on the surface can be described locally by plane wave transmission coefficients and Snell's law. The value of the potential at one point is independent of the values at other points. Hence, the contributions to the potential of energy traveling along the surface is neglected.

We now estimate the normal derivatives $\frac{\partial \Phi}{\partial n_2}$ and $\frac{\partial G_2}{\partial n_2}$.

$$\frac{\partial \Phi}{\partial n_2} \cong \frac{-T\dot{f}(t-\tau_1)}{|\underline{x}-\underline{x}_o|}\frac{\partial \tau_1}{\partial n_2} \tag{2.5}$$

$$\frac{\partial G_2}{\partial n_2} \cong \frac{-\dot{\delta}(t-\tau_2)}{4\pi|\underline{\xi}-\underline{x}|}\frac{\partial \tau_2}{\partial n_2} \tag{2.6}$$

The dot over the functions in (2.5) and (2.6) signifies time derivative. We approximate the normal derivatives by assuming that the amplitudes of G_2 and Φ vary slowly on the surface relative to the phase. Hence, we can discard the terms $\frac{1}{4\pi}\delta(t-\tau_2)\frac{\partial}{\partial n_2}(\frac{1}{|\underline{x}-\underline{\xi}|})$ and $f(t-\tau_1)\frac{\partial}{\partial n_2}(\frac{T}{|\underline{x}-\underline{x}_o|})$. Substitution of equations (2.3), (2.4), (2.5) and (2.6) into equation (2.1) yields

$$\varphi_2 = \frac{1}{4\pi}\int_{\partial v}\frac{T\dot{f}(t-\tau_1-\tau_2)}{r_o r}(\frac{\partial \tau_2}{\partial n_2} - \frac{\partial \tau_1}{\partial n_2})dS \tag{2.7}$$

where $r = |\underline{x}-\underline{\xi}|$, the distance from the surface to the receiver, and $r_o = |\underline{x}-\underline{x}_o|$, the distance from the source to the surface. We note that the discarded parts of normal derivatives are proportional to $\frac{1}{r_o r^2}$ and $\frac{1}{r r_o^2}$. For problems computed in this study, the distance from the source to the surface averages 40 kilometers and the distance from the surface to the receiver averages 20,000 kilometers. The $\frac{1}{r_o r^2}$ and $\frac{1}{r r_o^2}$ terms are $6.25\text{x}10^{-13}$ and $3.1\text{x}10^{-9}$, respectively, and are small relative to the term $\frac{1}{r_o r}$ in equation (2.7), which is $1.25\text{x}10^{-7}$. We therefore discard these terms with confidence.

To estimate $\frac{\partial \tau_1}{\partial n_2}$ and $\frac{\partial \tau_2}{\partial n_2}$, we recall that the gradient of the phase is parallel to the normal of the wavefront and has units of slowness. Thus,

$$\frac{\partial \tau_1}{\partial n_2} = \frac{\cos\Theta_1}{\alpha_1} \tag{2.8}$$

$$\frac{\partial \tau_2}{\partial n_2} = \frac{\cos\Theta_2}{\alpha_2} \tag{2.9}$$

where $\cos\Theta_1$ is the cosine of the angle between the normal to the refracted wavefront and the normal to the surface $\underline{n}_2$. It is equal to

$$\cos\Theta_1 = (1 - \frac{\alpha_2^2}{\alpha_1^2}\sin^2\Theta i)^{\frac{1}{2}} \tag{2.10}$$

where Θ_i is the local incident angle calculated by

$$\cos\Theta_i = \frac{(\underline{x} - \underline{x}_o)}{r_o} \cdot \underline{n}_2 \ . \tag{2.11}$$

$\cos\Theta_2$ is the cosine of the angle between the normal $\underline{n}_2$ and a ray connecting the surface and the receiver. Thus

$$\cos\Theta_2 = \frac{(\underline{x} - \underline{\xi})}{r} \cdot \underline{n}_2 \ . \tag{2.12}$$

Figure 2.1(b) shows a detailed picture of these angles. Substitution of the cosine factors (2.10) and (2.12) yields

$$\varphi_2 = \frac{1}{4\pi}\int_{\partial v} T\dot{f}\,(t - \tau_1 - \tau_2)\left(\frac{\cos\Theta_2}{r_o r \alpha_2} - \frac{\cos\Theta_1}{r_o r \alpha_1}\right) dS \ . \tag{2.13}$$

The method for the calculation of equation (2.13) is the same as that of Chapter 1. We simply calculate the integral as a summation of single point evaluations of the integrand. This method of integration requires that the elements which comprise the surface be small in length compared to the incident source wavelength. As in Chapter 1 we obtain the numerical ramp response from this integration and convolve it with the analytical third derivative of a Haskell isotropic source. Thus we obtain $\dot{\varphi}_2$, the time derivative of the potential.

These calculations are appropriate for precritical transmissions in a linear acoustic medium. We do not allow the transmission coefficient to be complex. When the incident angle Θ_i exceeds the critical angle, Φ equals zero. This boundary value is consistent with geometric ray theory, but is not a realistic shadowing function. Rather one expects Φ and $\frac{\partial \Phi}{\partial n_2}$ to vary smoothly across the shadow boundary if the surface is reasonably smooth. However, we argue that, under the circumstances considered here, the postcritical incidence portions of the integral contribute to the summed response of the transmitted potential at times much later than the specular portions and are unimportant.

As a check of the method, we compute the transmitted response of a wave propagating through a planar boundary separating two volumes of different sound speeds. We then compare the numerical maximum amplitude with that obtained from the following first-motion formula:

$$\varphi_t = TLf\left(t - \frac{r_o}{\alpha_1} - \frac{r}{\alpha_2}\right) . \qquad (2.14)$$

Here L is the spreading coefficient (Langston, 1977; Hong, 1978).

$$L = \left\{ \left(\frac{z_1}{\eta_{v1}} + \frac{z_2}{\eta_{v2}} \right) \left(\frac{z_1}{v_1^2 \eta_{v1}} + \frac{z_2 \eta_{v1}^2}{v_2^2 \eta_{v2}^3} \right) \right\}^{1/2} \tag{2.15}$$

where z_1 and z_2 are the vertical distances of the source and receiver, respectively, from the boundary. η_{vi} is

$$\eta_{vi} = \left(\frac{1}{\alpha_i^2} - p_o^2 \right)^{1/2} \tag{2.16}$$

where p_o is the ray parameter.

Figure 2.2 shows examples of this comparison. We have computed transmitted potentials for an incident isotropic source which is the first derivative of a Haskell source with parameters (B=2, K=10). The velocity and density model used for the comparisons are shown in the top of Figure 2.2(b).

Figure 2.2(a) shows two Kirchhoff synthetics and demonstrates the nature of truncation phases which can contaminate the synthetics. These phases arrive approximately 3½ seconds after the first arrival in both synthetic A and synthetic B and they are artifacts of the technique. In synthetic A, the phase is a result of the finiteness of the grid. A diagram to the left of the synthetic shows this effect. The grid is a square with a length of 150 kilometers. The source is 500 kilometers above the center of the grid; the receiver is 1000 kilometers below the source. From this diagram, we observe that the edge interferes at a time $t_2 = \frac{r_{o2}}{\alpha_1} + \frac{r_2}{\alpha_2}$. The geometric ray arrives

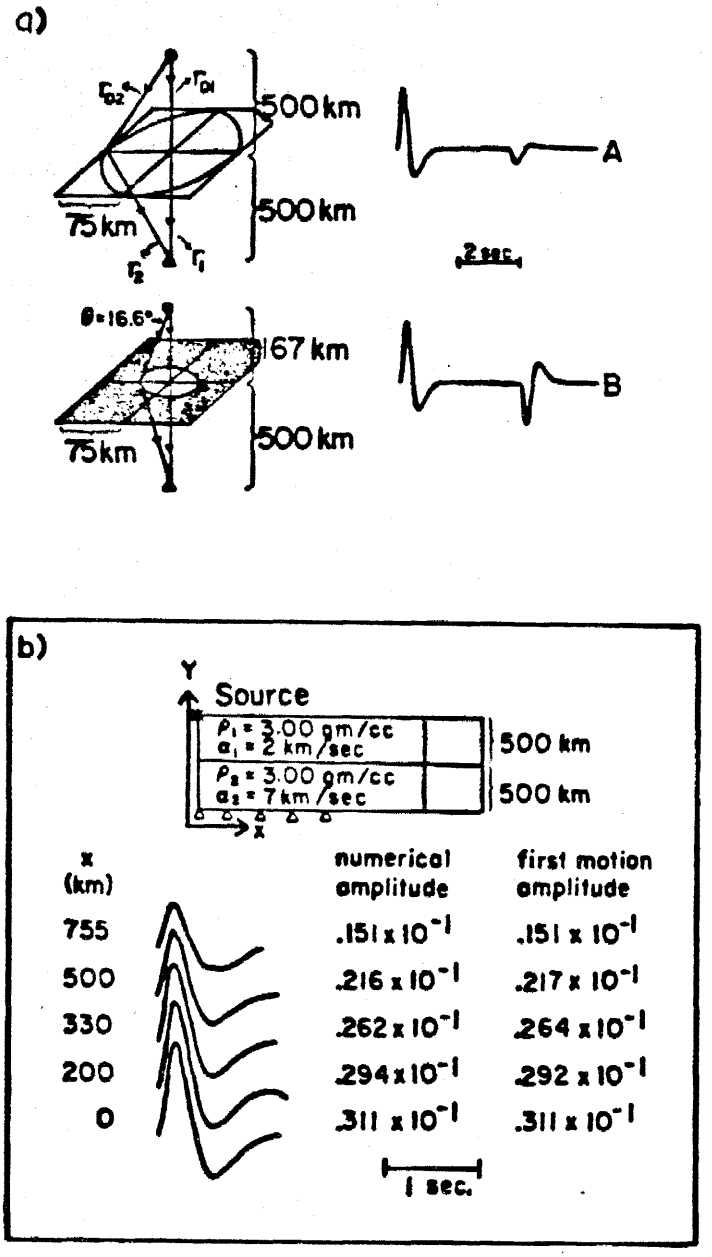

Figure 2.2. Two synthetics and the grid geometry used to compute them. Synthetic A is contaminated by a truncation phase which originates from the edge of the grid. Synthetic B is contaminated by a phase which originates from the abrupt change in boundary conditions. The grid next to synthetic B is gray when $\varphi = 0$ on the boundary. b) A comparison between Kirchhoff-Helmholtz and first-motion solutions. The input source is the first derivative of a modified Haskell function with parameters (B=2,K=10). The maximum dimensionless amplitude of the source input function is 45.1.

at a time $t_1 = \frac{r_{o1}}{\alpha_1} + \frac{r_1}{\alpha_2}$. Hence, the truncation phase arrives 3.6 seconds later than the first arrival in synthetic A.

In synthetic B, the phase is a result of the shadowing function. We use the same grid to calculate synthetic B as for synthetic A; however, the source is 167 kilometers above the interface. The local angle between the incident ray and the normal to the surface exceeds critical angle when the distance from the center of the grid exceeds 50 kilometers for the velocity model. Φ on the surface is 0 beyond this distance. This abrupt change in boundary conditions introduces a truncation phase into the synthetic. From the diagram to the left of synthetic, we can see that this phase will arrive 4 seconds later than the geometric arrival. The truncation phase in synthetic A caused by grid finiteness does not constitute a problem. If it contaminates the phase of interest, we can enlarge the grid appropriately. However, the truncation phase in synthetic B caused by the boundary conditions fundamentally restricts the source-receiver geometries we can investigate.

Figure 2.2(b) shows a profile of Kirchhoff synthetics for a source 500 kilometers above the interface and five receivers 500 kilometers below the interface. The horizontal distance, x, of the receivers ranges from 0 kilometers, directly underneath the source, to 755 kilometers. Two columns next to the synthetics contain the numerical peak amplitudes and the predicted amplitude from equation 15. The agreement is good. We cannot calculate a response past x=755 kilometers because a truncation phase resulting from the boundary conditions on the interface starts to interfere with the direct arrival. We must always take care to avoid such contamination.

NTS Structure (An Example of Near Source Effects)

We now apply the method by modeling the effects of idealized Moho structures on transmitted teleseismic P waves generated by nuclear tests in Pahute Mesa, Nevada Test Site. We wish to ascertain whether focusing-defocusing by structure on the Moho explains the unusual behavior of amplitudes from these tests.

We review these anomalous observations of short period P waves from Pahute Mesa. Figure 2.3 is a plot of ab amplitude measurements from 25 tests within Pahute Mesa as a function of station location from Lay et al. (1983a). The ab amplitudes are measured from the first peak to the first trough of the short-period seismogram. They are corrected for geometric spreading, the instrument gain at 1 second and event size, following a procedure developed by Butler (1984). The amplitudes are relative to a master event selected to minimize the overall scatter of the data.

The data have two important features. First, the relative amplitudes range from .13 at station TRI to 5.1 at station SHK. This variation is nearly a factor of 40. Most stations between the azimuths 0° and 60° have significantly lower amplitudes than those between 60° and 120°. Secondly, the relative amplitudes at a given station vary by a factor of 2½ as a function of event location within the mesa. The latter variation clearly originates from a near source mechanism because the events are separated by, at most, 15 kilometers.

If one calculates the mean relative amplitude at each station, then the overall amplitude variation with azimuth reduces to a factor of 12 (Lay et al.,

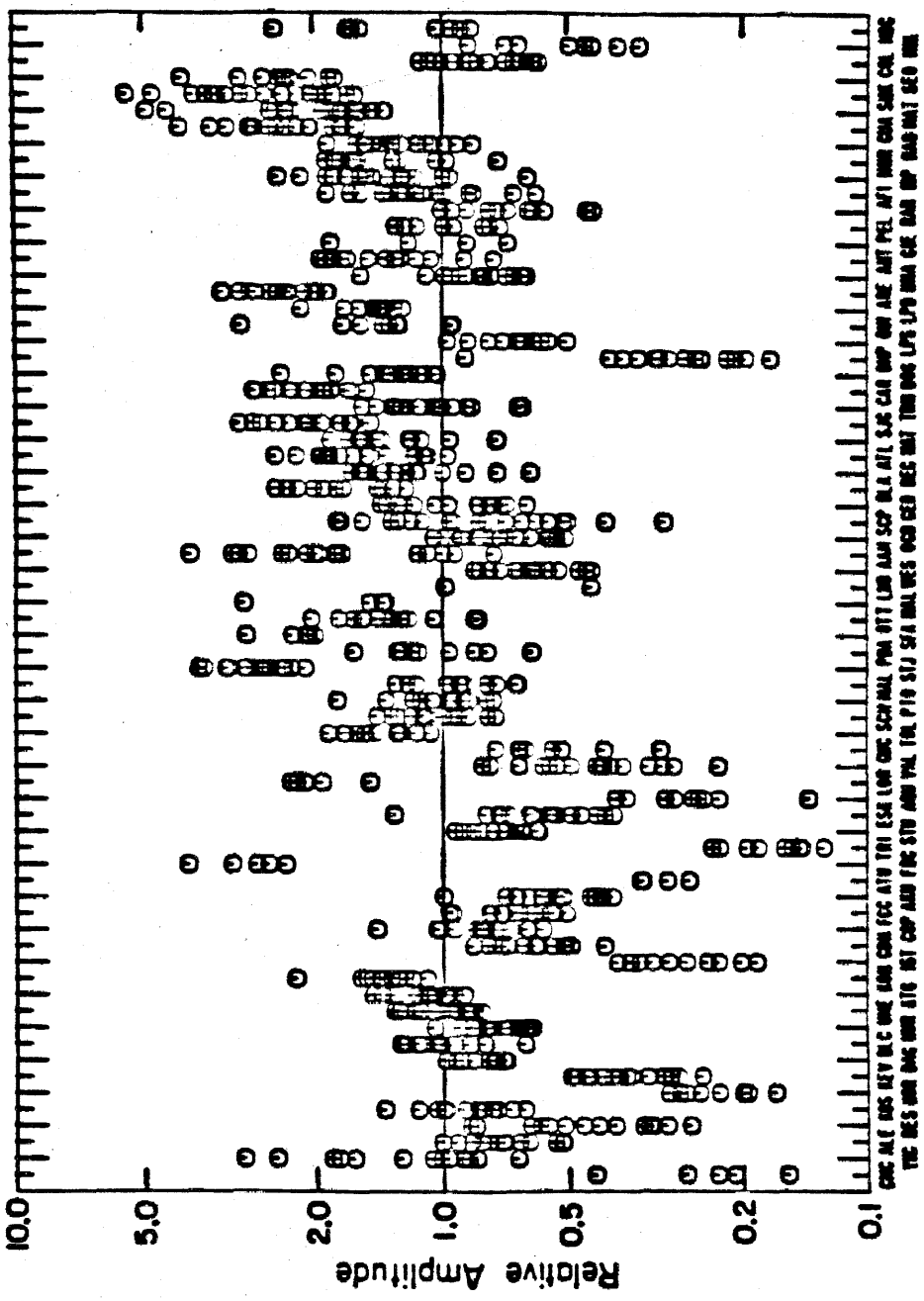

Figure 2.3. The short period P wave ab amplitude data set for 25 Pahute Mesa events plotted as a function of station location. The amplitudes are corrected for event size, geometric spreading and instrument gain at 1 second and are plotted relative to a master event (from Lay et al.,1983a).

1983a). The next two figures suggest that this large amplitude scatter is also a product of a near source mechanism. Figure 2.4, from Lay et al. (1983a), shows the azimuthal pattern of relative amplitudes for GREELEY, an event within the mesa, and FAULTLESS, an event 100 kilometers outside the mesa. Although both events have comparable yields, their azimuthal patterns differ substantially. This difference is particularly obvious between 0° and 90°. Figure 2.5 displays plots from Lay et al. (1983b) which enhance the difference between patterns of events in the mesa and events outside the mesa. These plots are ratios of amplitudes of three events outside the mesa (FAULTLESS, PILEDRIVER, and BILBY) divided by the average mesa amplitudes. These ratios are an approximate measure of a near source anomaly if the FAULTLESS, PILEDRIVER, and BILBY patterns are only influenced by path and receiver effects and are, therefore, constant as a function of azimuth. Furthermore, the path and receiver effects must be characterized by multiplicative factors. Because the ratio patterns for all three events are similar, these assumptions are probably true. Therefore, the factor of 13 variation of these ratios between 0° and 120° is roughly an estimate of the near source anomaly at the mesa.

To see if this amplitude variation correlates with waveform changes, we display in Figure 2.6 several seismograms at stations between 30° and 100° which recorded both FAULTLESS and GREELEY. The top and bottom seismograms are recordings of FAULTLESS and GREELEY, respectively, with their absolute ab amplitudes in millimicrons, corrected for instrument gain only. There is no obvious waveform differences in GREELEY records which

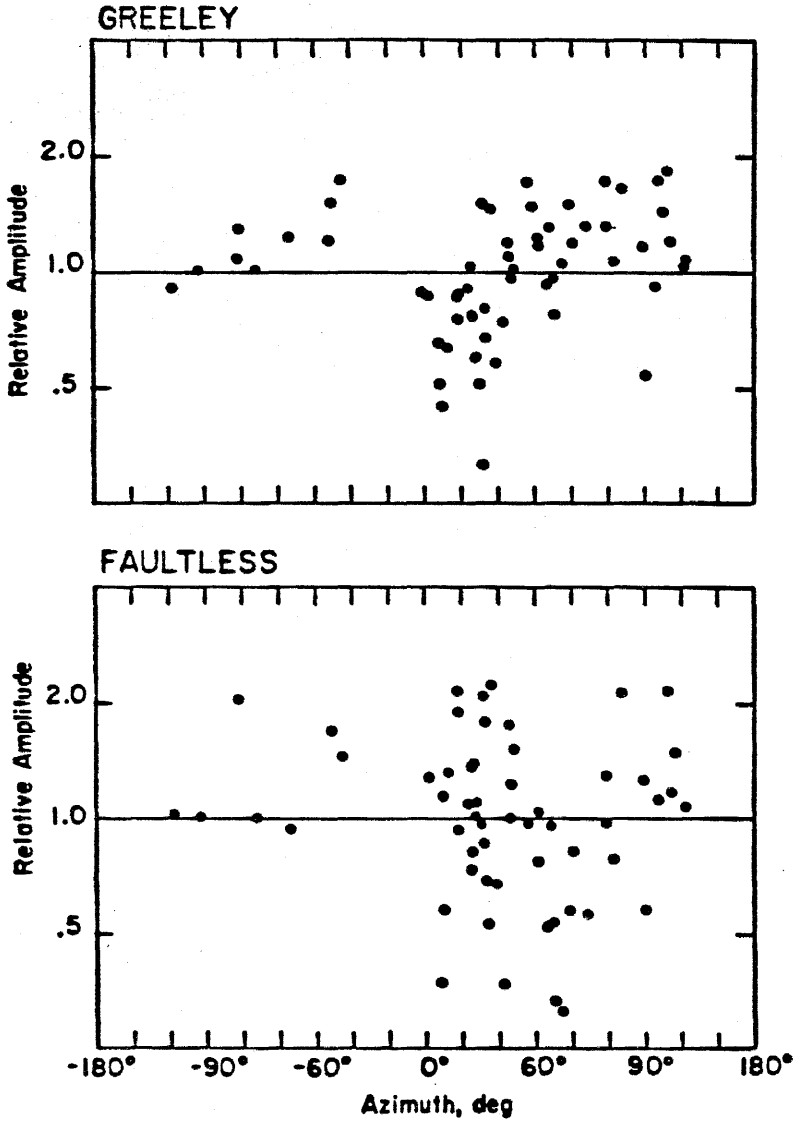

Figure 2.4. The relative ab amplitudes of GREELEY and FAULTLESS as a function of station location (from Lay et al., 1983a).

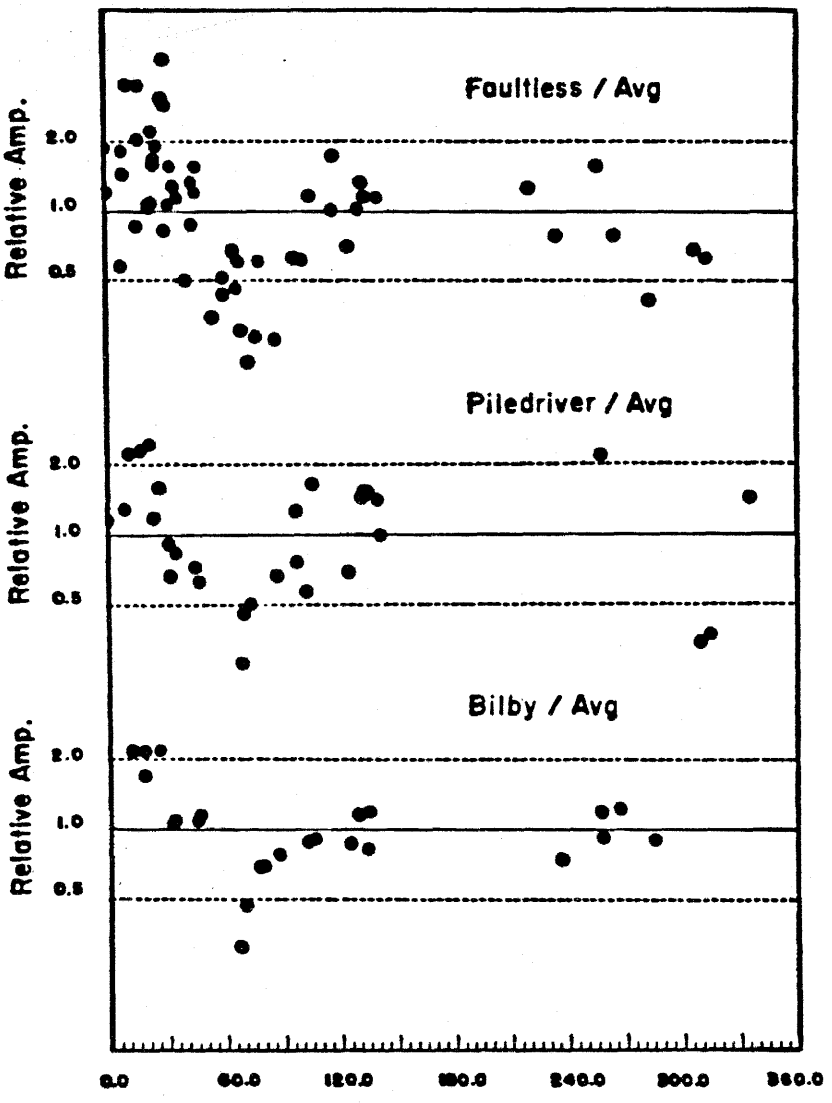

Figure 2.5. Ratios of relative ab amplitudes of FAULTLESS, PILEDRIVER, and BILBY divided by the average relative ab amplitudes of the mesa events (from Lay et al.,1983b).

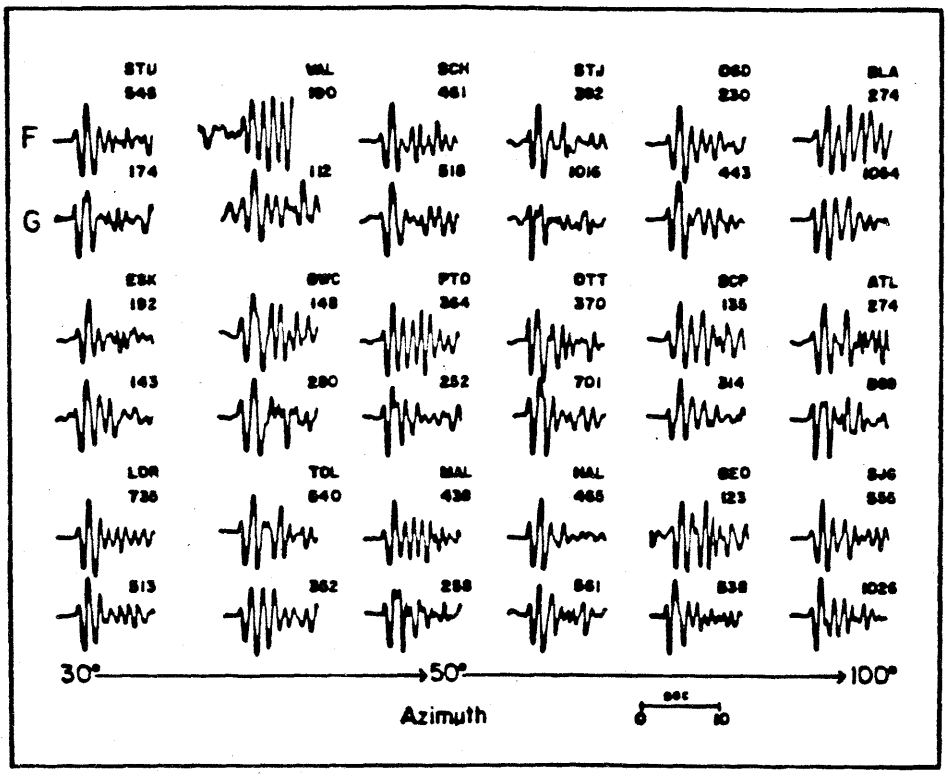

Figure 2.6. Seismograms from FAULTLESS (top record) and GREELEY (bottom record) displayed in order of increasing azimuth in the range of 30° to 100°. Also shown are the absolute ab amplitudes in millimicrons, corrected only for instrument gain at 1 second.

correlate with the dramatic ab amplitudes. Furthermore we do not see any obvious difference in frequency content and/or complexity between low stations and high stations for either event. However, there are some systematic differences between GREELEY and FAULTLESS seismograms. A shoulder occurs 2 to 3 seconds after the first arrival on GREELEY records (e.g., STU, PTO, MAL, STJ, OTT, GEO, and ATL). Lay has also seen these arrivals for other mesa events (Lay et al., 1983b). No such arrival is apparent on the FAULTLESS seismograms. Also the width of the first pulse of GREELEY seismograms is narrower than those of FAULTLESS seismograms at a few stations (e.g., SJG, ATL, BLA, GEO, SCP, and STU). Both phenomena, though, occur throughout the azimuthal range and do not correlate with the ab amplitude changes.

We conclude from the data that near source anomalies cause a variation of 2½ of relative ab amplitudes at a given station as a function of event location within the mesa. Moreover, near source anomalies also cause part of the large ab amplitude variation with azimuth (or station location) from mesa events. We cannot completely eliminate contamination of the azimuthal pattern by path and near receiver effects. Certainly, near receiver effects can be as large as those observed for the Pahute mesa tests (Butler, 1984). Yet the similarity of the ratio patterns of FAULTLESS, BILBY, and PILEDRIVER suggests that the pattern for mesa tests, seen in Figure 2.3, is dominated by a near source mechanism. Finally the variation of relative ab amplitudes with azimuth does not correlate with any obvious waveform changes for a typical mesa event, GREELEY. There is no definitive evidence to determine whether

ab variations correlate with travel time residuals.

In this study we assume that all the observed amplitude anomalies result from near source mechanisms. We then test the hypothesis that structure on the Moho, consistent with travel time residuals, focuses or defocuses P waves enough to produce the magnitude of the amplitude anomaly. We note that there are alternative near source explanations for these anomalies. In addition, to the focusing-defocusing hypothesis, workers (Lay et al., 1983; Wallace et al., 1983) postulate that the movement of faults associated with nuclear blasts causes a superposition of distributed or point double-couple sources with the isotropic bomb source. The amplitude anomalies are, then, the radiation pattern caused by a double-couple source. Longer period studies of Love/Rayleigh ratios, Pnl, P and S waves (Aki and Tsai, 1972; Wallace et al., 1983; Nuttli, 1969) generated by these blasts support the latter hypothesis. However, we speculate that, as the frequency content of the signal increases, the role of lateral near source structure in distorting amplitudes becomes more important. From travel time residual studies (Minster et al., 1981; Spence, 1974) workers have deduced that there is a high velocity zone directly beneath the Silent Canyon Caldera in the mesa which extends down to 100 kilometers. Such a velocity structure may cause amplitudes which deviate from those predicted by a spherically symmetric Earth model.

To investigate how geology can affect amplitudes, we presume that the apparent velocity variations deduced from the travel time residuals are a manifestation of Moho topography. We exclude from consideration the

impact of the Silent Canyon volcanics on transmitted P waves because both Spence (1974) and Minster et al. (1981) correct the residuals statically for these low velocity rocks; thus the residual patterns are not a result of the caldera. In any case, we cannot readily model a feature so close to the source. If we place a strong velocity discontinuity, such as that between volcanic and granitic rocks, closer than 10 kilometers to the source, we generate a truncation phase which interferes with the transmitted P phase.

We describe the Earth with a two-layer crust-mantle velocity model. The velocity of the upper layer is 6.5 km/sec and that of the lower layer is 8 km/sec. The depth of the interface is 45 kilometers. The receivers are located at distances such that the $\frac{1}{R}$ amplitude decay corresponds to spreading at teleseismic distances between 60° and 70° for a JB Earth (Langston and Helmberger, 1975).

The number of ways to distort the Moho is infinite. We, therefore, restrict ourselves to a few three-dimensional topographies where the maximum height of the anomaly is 10 kilometers and the maximum width is approximately 25 kilometers. The choice of these values is based on both the Minster et al. (1981) and Spence (1974) studies. They find an advance of ≈.25–.4 seconds for nearly vertical rays from shots within the caldera. As these rays become shallow, this advance lessens or disappears completely. From crude calculations, we estimate that 10 kilometers of upward relief on the Moho will produce the required timing anomalies of these rays. Furthermore, we confine the upwarp laterally so that rays exiting the mesa at shallow angles are unaffected by the anomaly. We recognize that these

structures are extreme. However, if we cannot produce the observed amplitude anomalies with these topographies, we can discard structure on the Moho as the dominant cause of these anomalies.

Of the infinite number of upwarps, we arbitrarily select four examples with height c = 10 kilometers and width w = 25 kilometers. These topographies are described by simple analytical formulas and are convenient to use. The topographies with their labels are as follows:

$$\textit{Upwarp}: \quad Z = Z_{con} + \frac{c}{2}(\cos(2\pi((r - w/2)/w)) - 1) \text{ if } r \le \frac{w}{2}, \quad Z = Z_{con} \text{ if } r > \frac{w}{2} \tag{2.17}$$

$$\textit{Exponential}: Z = Z_{con} - ce^{-4.605r/\frac{w}{2}} \tag{2.17a}$$

$$\textit{Plug}: Z = \begin{cases} Z_{con} - c & \text{if } r \le \frac{w}{2} \\ Z_{con} + \frac{c}{2}(\cos(2\pi((r - \frac{w}{2} - 5)/w)) - 1) & \text{if } \frac{w}{2} < r \le \frac{w}{2} + 5 \\ Z_{con} & \text{if } r > \frac{w}{2} + 5 \end{cases} \tag{2.17b}$$

$$\textit{Sinc}: Z = Z_{con} - c\ sinc\left[\frac{21.991r}{w}\right]. \tag{2.17c}$$

Here $r = \sqrt{(x - x_0)^2 + (y - y_0)^2}$ and is the horizontal distance of each point on the surface from the center of the grid. Z_{con} is the baseline level of the Moho and is 45 kilometers for all the calculations. The values of the constants in the exponential and the sinc bumps confine the anomaly's width to approximately 25 kilometers. A schematic cross section of each topography is shown in Figure 2.7. All the structures are symmetric with azimuth.

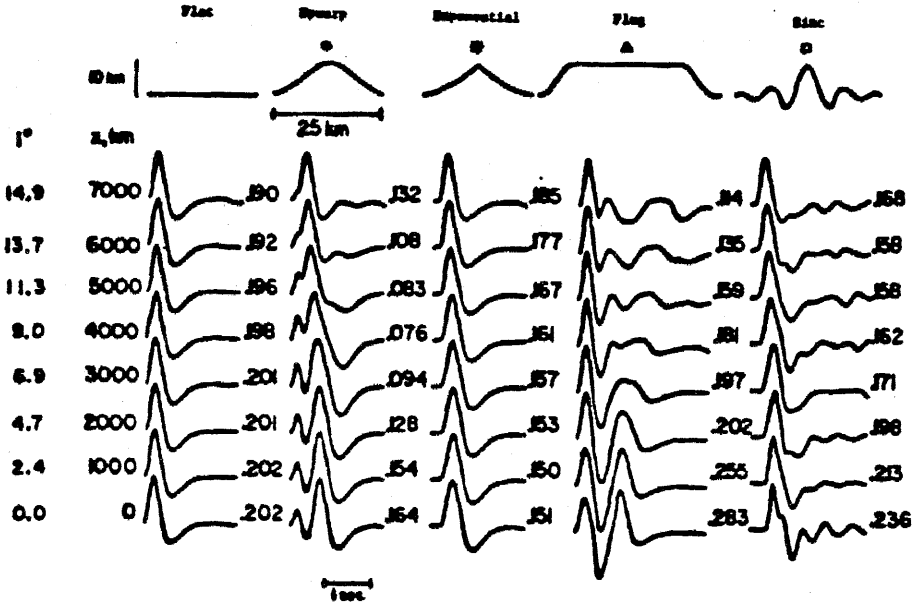

Figure 2.7. Transmitted potentials from sources 35 kilometers above the center of the structure. The cross sections of the structure upwarp, exponential, plug and sinc are above the synthetics. For comparison potentials which propagate through a flat boundary are also shown in the first column. The potentials are from receivers which are 20,000 kilometers below the source and which vary from 0 to 7000 kilometers horizontally away from the source. All amplitudes are multiplied by .01.

Initially an isotropic source is directly above the center of the structure; thus, the transmitted potential is only a function of x and z. The source is 45 kilometers above the baseline of the Moho. The transmitted potential is calculated at receivers which are 20,000 kilometers below the source. The horizontal distance of the receivers from the center of the topography ranges from 0 to 7,000 kilometers. Figure 2.7 shows the transmitted potential and the peak amplitude as a function of x in increments of 1,000 kilometers for each of the four topographies. In addition, the responses for a wave which transmits through a planar boundary are displayed in the first column. The corresponding takeoff angle for the flat boundary synthetics are to the left of the column. By comparing these synthetics with those in the other columns, we can determine how much distortion of the waveform is caused by each structure. The synthetics in Figures 2.7 and 2.10 do not include a Q and instrument operator or a reflected pP phase. Although these effects are important, we want to examine amplitude and waveform distortions caused by structure with a simple input pulse. The ringing caused by an instrument or pP may mask the presence of multiple arrivals caused by the topography.

All the structures cause intriguing changes in the waveforms and arrival times of the synthetics. The waveform features originate from timing changes caused by each topography. Each point of the Kirchhoff synthetic originates from elements which are illuminated by the source and, in turn, illuminate the receiver at a total travel time, $\sigma=\tau_1+\tau_2$. We can associate, with each element of the grid, a value of total travel time, $\sigma(x,y)$. The total travel time function on the surface depends on the source location, the

receiver location, and the surface geometry. Figure 2.8 shows examples of this function. Here we calculate $\sigma(x,y)$ for elements which make up a flat interface 2.8(a), an upwarped interface 2.8(b), a plug 2.8(c), and a sinc function 2.8(d). In each example the source is directly above the center of the structure and is 45 kilometers above the baseline of the interface. The receiver is 20,000 kilometers directly below the source. The contours of constant total travel time are projected onto the topography (top figure in 2.8(a),(b),(c), and (d)). We also display these contours as a function of x and y (bottom figure in 2.8(a),(b),(c), and (d)) The contours are circles because of the particular source-receiver geometry. For the sake of brevity, we only show that portion of the grid which contributes to the initial second of each Kirchhoff synthetic. The synthetics which correspond to these total travel time functions are also shown. (middle figure in 2.8(a),(b),(c),and (d)) These figures show how structure on the interface distorts the total travel time contours and, as a result, produces multiple arrivals in the synthetic.

We examine this effect in detail. The contours are in intervals of .125 seconds as are the tick marks below the synthetics in Figure 2.8. The geometric arrival time occurs at the center of the contour plot. Thus, by counting the contours, we can estimate the cumulative area of the surface which contributes to the synthetic at a given time. We deduce, from Figure 2.8, that, approximately,

$$A(t) \alpha \left. \frac{dS}{dt} \right|_t . \qquad (2.18)$$

A(t) is the amplitude of the response at time t. S is the total area of the

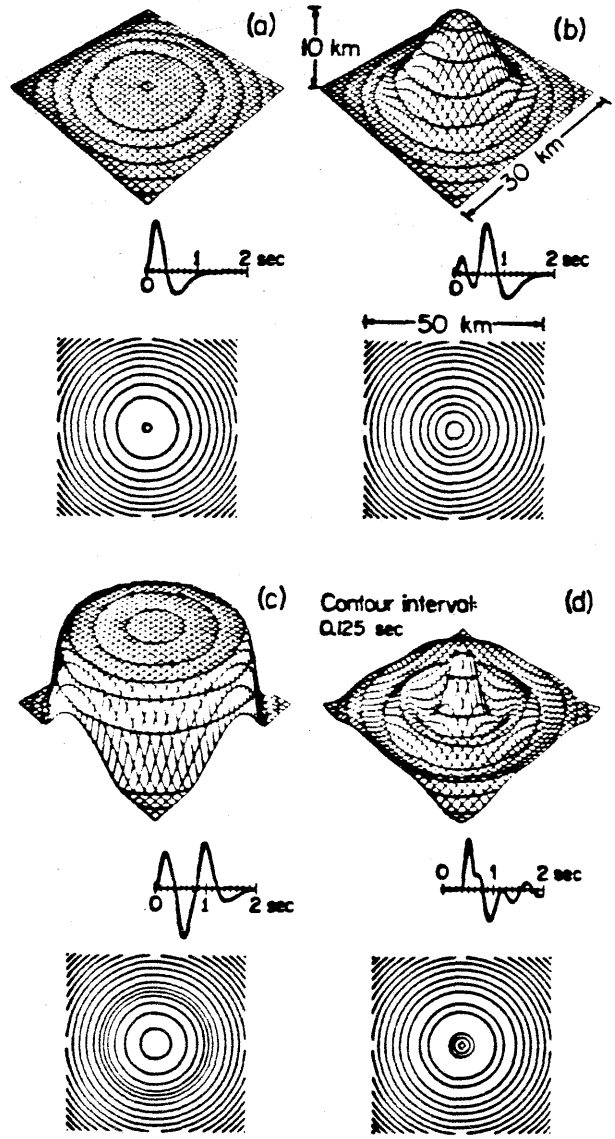

Figure 2.8. Travel time contours for a source 35 kilometers directly above the structure and receivers 20,000 kilometers directly below the source. The four structures are a) a plane , b) an upwarp, c) a plug, and d) a sinc function. The contours are projected onto the topographies and flat grids. The synthetics which correspond to each travel time projection are in between the two projections. The contour interval is .125 seconds as are the tick marks of the synthetics. The geometric arrival time is the center of the contours.

surface which contributes to the response at time t. For example, the initial .375 seconds of the synthetic from a flat interface results from a rapid increase in the cumulative area of the surface which is illuminated between t=.125 sec and t=.25 sec. After t=.25 seconds, the area of the surface is illuminated at a constant rate. Thus, the resultant synthetic can be viewed as a convolution of the source time function with a step function which starts between t=.125 sec and .25 sec.

We quantify this statement by following an approach developed by Hilterman (1975) and Haddon and Buchen (1981). The symmetry of the source-receiver geometry and the surface geometry allows us to recast the integral (2.13) as a one-dimensional integration with respect to total travel time, σ. If the transmission coefficient varies slowly over the surface, then

$$\varphi_2 \cong \frac{T}{4\pi} \dot{f} * \left(\frac{\dot{\Omega}_2}{\alpha_2} - \frac{\dot{\Omega}_1}{\alpha_2} \right) \tag{2.19}$$

where

$$d\Omega_1 = \frac{\cos\Theta_1}{r_0 r} dS$$

and

$$d\Omega_1 = \frac{\cos\Theta_2}{r_0 r} dS$$

$\dot{\Omega}_1$ and $\dot{\Omega}_2$ are the time derivatives of modified solid angles. Ω_1 is a modified solid angle with vertex at the source subtended by the surface S, and Ω_2 as a modified solid angle with vertex at the receiver subtended by S.

We now examine the origins of the multiple arrivals in the potentials which propagate through interfaces with structure. For example, the amplitude and frequency content of synthetics from the upwarp (column 3 of Figure 2.7) are controlled by the interference of two pulses. The travel time contours in Figure 2.8(b) for the upwarp differ considerably from those of a flat interface 2.8(a). Far less of the upwarped surface is illuminated within .25 seconds of the geometric arrival time. Furthermore, the upwarp topography causes subtle changes of the width between travel time contours. There are two locations where this change occurs: 1) at the top of the upwarp and 2) at the edge of the upwarp. The first pulse in this synthetic originates from the elements in the first location while the second pulse originates from the second location. Because the ring of elements which contribute to the second pulse has a larger area than that of elements which contribute to the first pulse, the second pulse is larger than the first pulse.

As the receivers move away from the center, the maximum amplitudes decrease as a result of the interference of the two pulses. We destroy the symmetry of the surface illumination by moving the receivers horizontally. The illumination of elements, which initially was simultaneous, now occurs at slightly different times and causes destructive interference; this destructive interference causes a reduction in peak amplitudes and the broadening of the pulse widths for both phases. Moreover, as the receiver moves out laterally, the planar part of the boundary becomes more important in controlling the amplitude of the transmitted pulse. Hence the amplitudes, travel times, and the waveforms of distorted pulses approach those of a pulse

which has propagated through a flat boundary. This phenomenon is present in almost all the top synthetics in Figure 2.7.

Other intriguing features are present in the synthetics shown in Figure 2.7. The potentials transmitted through the sinc and exponential bumps shown in columns 3 and 5 have an apparent delay which is not seen in the other synthetics. These two topographies drop in height near the peak more rapidly than does the upwarp topography. Consequently, fewer elements are illuminated and contribute to the transmitted potential at times near the geometric arrival time. This is illustrated for the sinc topography in Figure 2.8(d). Hence, the amplitude near the geometric arrival time is lower than amplitudes at later times.

The opposite is true for the synthetics of waves which are transmitted through a plug. They are displayed in column 4 of Figure 2.7. The topography and travel time contours for the bottom synthetic from this column are shown in Figure 2.8(c). This figure shows that more elements are illuminated and contribute to the response near the geometric arrival time for this topography than for the upwarp, sinc, and exponential topographies. The resultant synthetic is made up of two pulses of equal size. Each pulse has the amplitude and shape of a wave which has transmitted through a planar interface. The plug is essentially comprised of two planar interfaces, one at z = 45 kilometers and the other at z = 35 kilometers. The edges of the plug have been tapered to avoid a shadowing problem. While the difference in the interface depths does not alter the amplitudes of the pulses, it does change the arrival times. This slight separation in arrival time causes the observed

interference pattern. As the receiver moves out laterally, the timing between the two pulses changes. The pulse width of the first arrival narrows while the width of the second one broadens. By transmitting a wave through such a structure, we vary the maximum amplitude of the synthetics by a factor of 2½.

We confirm that these structures are approximately producing the correct travel time anomalies. We plot the residuals, in addition to the peak amplitudes of the synthetics, as a function of distance to discern any systematic relationship between the two parameters. We also plot the amplitude of the first pulse if the synthetic is made up of multiple arrivals. This amplitude is measured from the start of the synthetic to the first peak. The plots are displayed in Figure 2.9. The travel time "residuals" are defined by the difference between the arrival times of transmissions through a bumpy surface and the times of transmissions through a flat surface. Where there is an apparent delay in the synthetics such as in those from the exponential and sinc bumps, we measure the arrival time at the start of the upswing. The amplitudes are uncorrected for geometric spreading. The change of amplitude from spreading, seen in the synthetics in column 1, is negligible in the distance range of interest; hence no correction is necessary.

The "residuals" in Figure 2.9 produced by these structures behave in a predictable fashion. The transmitted potentials which propagate vertically to stations between 0 to 4,000 kilometers experience the most advance. The exceptions to this behavior are residuals from the sinc and exponential synthetics. We know there is some energy arriving at these nearly vertical

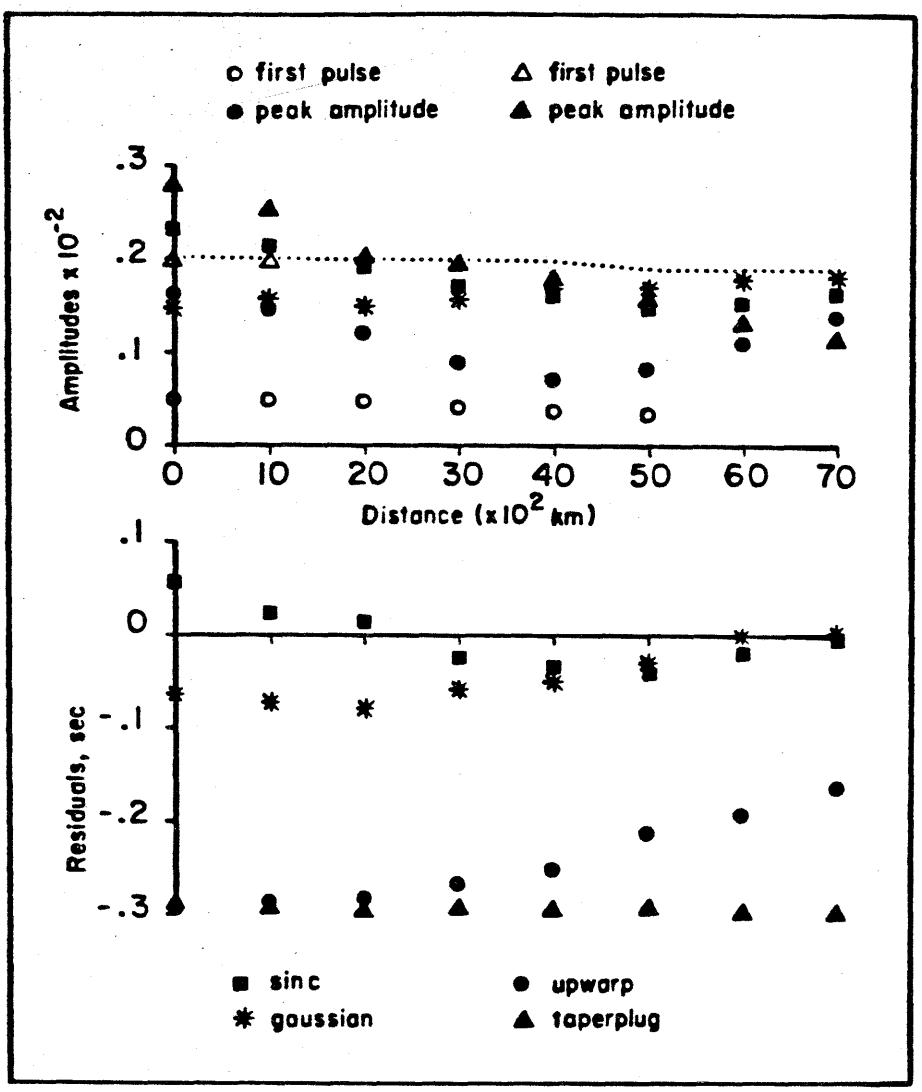

Figure 2.9. Plots of peak amplitudes, amplitudes of first pulses, and travel time residuals as a function of distance from synthetics in Figure 2.7. The different symbols correspond to different topographies and are at the bottom of the figure. Where first-pulse amplitudes are different from peak amplitudes, the values of first pulse amplitudes are plotted with open symbols and the peak amplitudes are plotted with closed symbols. The dotted line corresponds to the peak amplitudes from synthetics which propagate through a planar interface.

stations with -.3 second advance from the previous discussion. However, because the energy is so small relative to later pulses, these synthetics appear to have delays.

When the paths of the potentials become shallower, we see that the advance disappears. The planar part of the interface begins affecting the travel times and waveforms. The arrival times of the transmissions through the bumps approach those of transmissions through a flat interface. The exception to this pattern is the residuals of the plug synthetics. These synthetics have an advance of .3 seconds which is constant as a function of horizontal distance. This behavior results from the constant height of the plug across the entire width of the bump.

What is the relationship between the travel time anomalies and the amplitude anomalies? We predict that as the magnitude of the travel time anomalies decreases the magnitude of the amplitude anomalies decreases also. The amplitudes, as well as the arrival times, will be controlled by the planar part of the surface. This relationship is observable in Figure 2.9. The amplitudes, except in one case, start to approach the value of .002 at distances ranging from 5,000 to 7,000 kilometers. The exception is the maximum and first-pulse amplitudes of the synthetics from the plug topography. These values appear to decrease systematically with distance. However, these values do approach the planar amplitudes at distances beyond 7000 kilometers.

Furthermore, waves which arrive earlier than is predicted by planar calculations also have lower amplitudes than is predicted. Contrarily, the

synthetics from the sinc topography arrive late and have anomalously high amplitudes. Indeed, the pattern of residual variation is precisely mimicked by the pattern of amplitude variation for this structure. The mimicking of amplitude and travel time anomalies also occurs for synthetics from the exponential bumps.

This mimicking does not occur for synthetics from the upwarp and plug topographies. Each of these synthetics consists of multiple arrivals. Thus, if we take the maximum amplitude as a measure of amplitude anomaly and compare with travel time anomalies, we do not see an obvious correlation between the two parameters. The travel time is perturbed by a relatively small part of the surface. The maximum amplitude is perturbed by a much larger part of the surface. It is a less local property of the topography. If we allowed a broader band time function to interact with the surface we would change the amplitude anomaly but not the travel time anomaly. To improve the correlation, we measure the amplitude of the first pulse of the synthetic if it is different from the maximum amplitude. These values are shown in Figure 2.9 by the open circles and triangles for the upwarp and plug synthetics. We do not improve the visual correlation significantly.

The modeling of a symmetric structure demonstrates that such a structure on the Moho, consistent with travel time residuals, can produce a factor of 2½ in maximum amplitude variation as a function of distance. The variation of amplitudes of first pulses is somewhat less. Neither variation is as large as the observations of amplitude changes between stations for a given test at NTS. Furthermore, where there is a large amplitude variation, there

is significant waveform distortion of the synthetics. For the most part, low amplitudes are produced by the upwarps. However, the mesa data set has both anomalously high and low amplitudes. The low amplitude synthetics arrive early. However, any relationship between amplitude anomalies and travel time anomalies is dependent on frequency because the effect of a structure on a wave is dependent on frequency.

The modeling to this point produces anomalies which are dependent only on distance because the structures are symmetric. We now introduce asymmetry into the problem by allowing the source to move off the center of a symmetric upwarp. We do these calculations because observed travel time and amplitude anomalies are presented as a function of azimuth. Yet we do not know if these anomalies arise from azimuthal or delta heterogeneities. We want to examine whether a trend with delta or azimuth is stronger. Additionally, there is a variation of amplitude at a given station with a change in source position in the mesa. If we change the source position across a sample structure, can we reproduce the factor of 2½ seen in Figure 2.3? We also wish to examine whether there is any systematic relationship between amplitude and travel time anomalies as a function of azimuth as we have done previously with these parameters as a function of distance.

The modeling experiment is quite similar to the previous one. The receivers are 1000 to 7000 kilometers horizontally away from the center of the topography and 20,000 kilometers below the source. The sources are 45 kilometers above the baseline of the Moho. To produce the azimuthal anomalies in the synthetics, we move the source off the center of the upwarp

in one direction in increments of two kilometers. The responses are calculated for seven distances at five different azimuths. We select the topography upwarp for this experiment. The choice of topography is somewhat arbitrary; however, we make this particular choice because this topography causes substantial variation in amplitudes as a function of distance. If this topography fails to produce much azimuthal variation, then the other topographies will fail to do so, also.

Figure 2.10 shows our results. A cross section of the source-receiver configuration and the geometry of the upwarp is in the center of the figure. In addition, a topographic map of the center portion of the grid is displayed. The contours are in kilometers and the maximum height of the bump is 10 kilometers. The topography map also shows the source locations and the azimuthal lines along which the calculations are done. The resulting waveforms and maximum amplitudes surround these diagrams. Each group of 28 waveforms is calculated for the corresponding azimuth. The groups are made up of four columns of synthetics corresponding to calculations done with the source location designated at the top of each column. Sources A, B, C, and D are, respectively, 2, 4, 6 and 8 kilometers from the center. The rows correspond to calculations done at the horizontal distances shown next to the row. In Figures 2.11, 2.12, and 2.13 we plot the travel time residuals, peak amplitudes, and amplitudes of the first pulse obtained from these synthetics as a function of azimuth for each distance.

There is a change in overall complexity of the synthetics as a function of azimuth. The waveforms from the group at $\theta = 0°$ are simple and impulsive

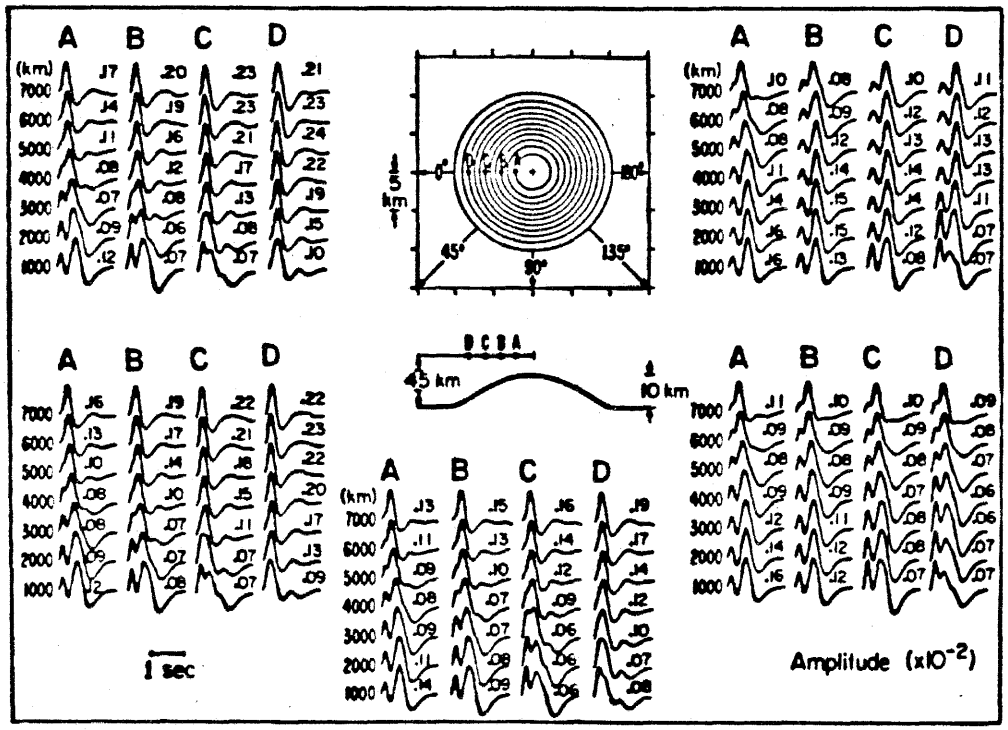

Figure 2.10. Synthetics from the topography upwarp calculated for four source positions, five azimuths and seven distances. The topography map and cross section with source positions are in the center. The contour interval is 1 kilometer. The corresponding distances angles and azimuths are also shown.

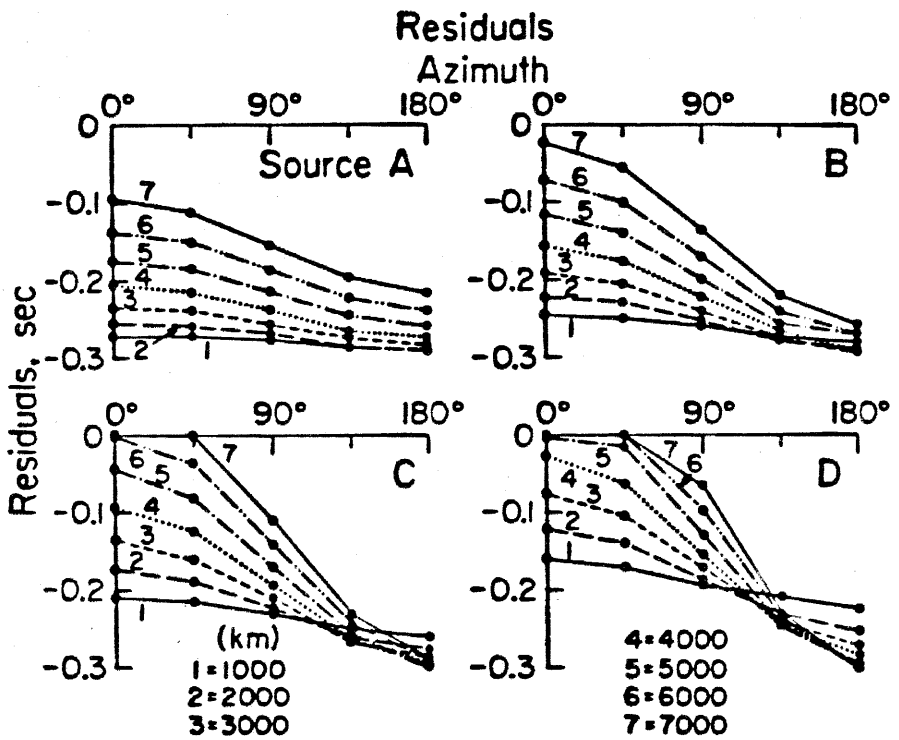

Figure 2.11. Travel time residuals for source locations A, B, C, and D plotted as a function of azimuth and distance.

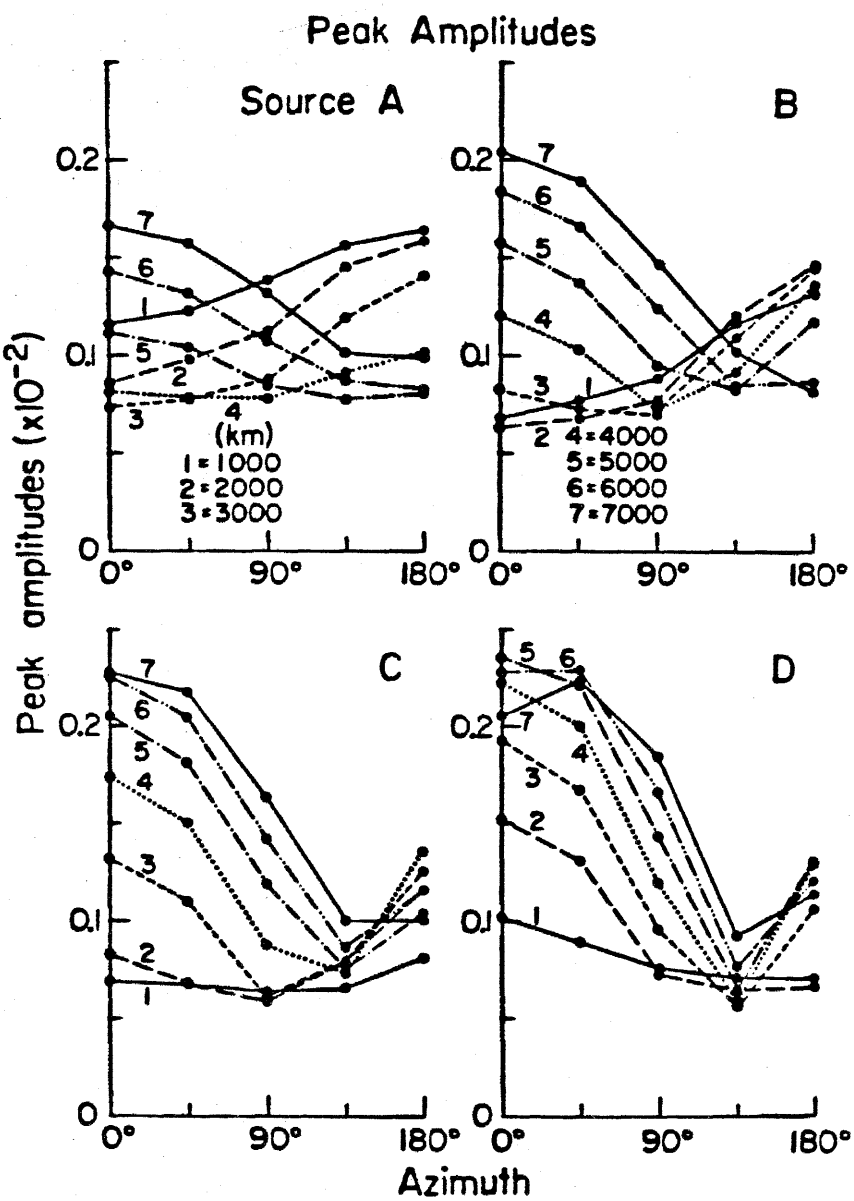

Figure 2.12. Peak amplitudes for source locations A, B, C, and D plotted as a function of azimuth and distance.

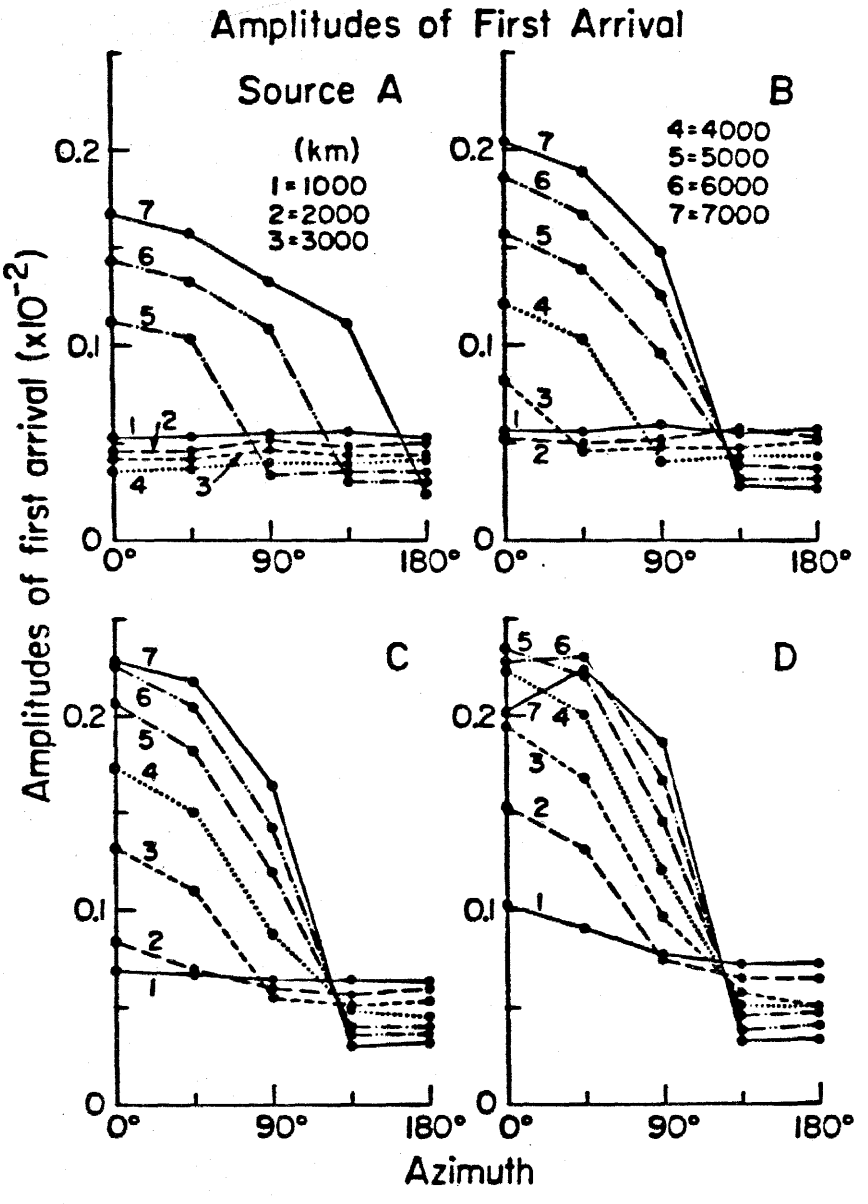

Figure 2.13. Amplitudes of the first pulse for source locations A, B, C, and D plotted as a function of azimuth and distance.

with relatively high amplitudes. Only the stations at 1,000 or 2,000 kilometers have multiple arrivals. As we rotate counter clockwise around the structure, a greater number of the synthetics in each group have multiple arrivals, and, consequently, low amplitudes. Synthetics at $\theta = 135°$ and 180° all have multiple arrivals. The reason for this trend is the same as in the previous modeling study. As the sources move in the direction of a line along $\theta = 0°$, a greater proportion of the elements which constitute the planar part of the grid contribute to the potentials calculated in the direction of this line. Hence, synthetics of this line become more impulsive as the source migrates from position A to position D. By contrast, the synthetics at $\theta = 135°$ and 180° remain complex. The elements which contribute to these potentials are largely from the non-planar part of the boundary.

We examine the maximum amplitudes, first amplitudes, and travel time residuals in Figures 2.11, 2.12, and 2.13 for systematics as a function of distance or azimuth. The behavior of maximum amplitudes with distance and azimuth is the most variable of the three parameters. The maximum amplitudes as a function of azimuth do not appear to correlate very well with the travel time residuals. The rapid change of this parameter with azimuth and source position reflects the sensitivity of maximum amplitudes to slight changes in relative timing between the two arrivals which make up the synthetics. We observe the smallest range of maximum amplitudes with distance and azimuth from synthetics calculated with source position A, the closest source to the center of the symmetric source. We increase this variation with azimuth and distance when we remove the source further away

from the center to positions B, C, and D.

The maximum amplitudes at $\theta = 135°$ for source positions B, C, and D are lower than the amplitudes at other azimuths. This trend is a result of 1) the degree to which the planar part of the grid contributes to the response and 2) the degree of symmetry of the source and receiver locations with respect to the structure. Stations along $\theta = 0°$ and $\theta = 180°$ are in positions of symmetry with respect to the sources. Elements on either side of a line which divides the grid contribute simultaneously to the responses at these stations and ,consequently, cause higher maximum amplitudes. Stations along $\theta = 90°$ and $\theta = 45°$ are not symmetrically positioned with respect to the source; however, the planar part of boundary largely contributes to these responses; thus, they have high maximum amplitudes. But receivers along $\theta = 135°$ are placed asymmetrically which causes elements to illuminate at different times; in addition, these elements are largely in the perturbed part of the boundary. These two factors combine to produce the overall lower maximum amplitudes of receivers at $\theta = 135°$.

Although we do not discern any relationship between the maximum amplitudes and the travel time residuals as a function of azimuth, we do see a correlation between the amplitudes of the first pulses and the travel time residuals. Synthetics which have a constant first amplitude as a function of azimuth also have approximately constant travel time residuals. The travel time advances increase as a function of azimuth. Similarly, the first amplitudes decrease with azimuth. Thus, early arrivals have lower first amplitudes than the later arrivals. Recall that this particular topography will not

produce a delay; all the travel time anomalies are advances. The trend of early arrivals with low amplitudes and late arrivals with high amplitudes holds true for all azimuths, distances, and source positions.

The travel time residuals decrease as a function of distance at all azimuths except for $\theta = 135°$ and $\theta = 180°$ for sources C and D. Here we see a reversal whereby residuals increase as the distance increases. Clearly if we pull the source off the center far enough, the shallower rays will interact with the upwarped part of the topography while the steeper rays interact with the flat part of the grid.

As we remove the source off the center, the range of variation of first amplitudes and travel time residuals as a function of azimuth exceeds the range of these parameters with distance; that is, the trends of these parameters are stronger in azimuth than in distance. Thus, stronger variation of travel time and amplitude anomaly with azimuth than with distance may be an indicator of lateral variation with azimuth, as well as with distance, despite an uneven station distribution of the existing data set.

What conclusions can we draw from this modeling experiment? Firstly, we create a variation of 2½ of first amplitudes as a function of azimuth and source position. The change of amplitude with source position is largest at $\theta = 0°$ and 45° and is the least at $\theta = 180°$. However, the variation at 0° and 45° is created at the cost of considerable distortion of the waveform. This feature of low amplitude waveforms with complex or broadened pulses and high amplitude waveforms with simple narrow pulses is not apparent in the mesa data set.

Secondly, we produce a trend in the first pulse amplitudes with azimuth. Specifically, we cause high amplitudes at $\theta = 0°$, 135° , and 180°. However, if we remove the source far enough away from upwarp, we will produce no amplitude anomalies. Thus, structure can produce a systematic azimuthal trend in amplitudes. But we must be cautious about pushing this interpretation too far. Our azimuthal trend is an artifact of the moveout of the source in one direction with respect to the lines of receivers. If we imagine distributing sources all over the upwarp and then calculating the averages of the first amplitudes at each azimuth for all the sources, we undoubtedly eliminate any trend with azimuth. Thus, the stability of the amplitude pattern of all mesa events with azimuth location is not easily explained by structure on the Moho or any unusual velocity plug unless the sources are fortuitously located to one side of the heterogeneity.

Thirdly, we do see a visual correlation between travel time residuals and amplitudes of first pulses, but do not see any between residuals and peak amplitudes. This correlation may be diagnostic of structure as opposed to tectonic release.

Discussion and Conclusions

We show from the previous two modeling experiments that we can produce variations of 2½ as a function of delta, azimuth, and source position with a structure on the Moho that produces travel time residuals compatible with the Minster et al. (1981) and Spence (1974) studies. The variation is created at the cost of considerable distortion of the waveform. Furthermore, the

travel time residuals correlate with first-pulse amplitudes but not with peak amplitudes. To determine whether these initial results are applicable to the Pahute Mesa data, we must now include a pP phase, a Q operator and an instrument operator in a few Kirchhoff synthetics.

We select two sets of five Kirchhoff-Helmholtz synthetics calculated previously for the azimuthal study to incorporate a pP, Q and a short period instrument. They are the responses at a distance of 4000 kilometers. The two sets correspond to the source positions A and D at five azimuths. This choice represents two extremes of source positions relative to a structure and may give us a reasonable idea of what to expect in amplitude and waveform variation as test sites move within the mesa.

We put pP into the Kirchhoff-Helmholtz synthetics by convolving these synthetics with a boxcar function of unit height and a width corresponding to the pP-P lag time. This convolution yields the impulse response of P and pP if the incident source is a modified Haskell function rather than its time derivative. We justify this simple modeling of pP by assuming that the reflection coefficient of this phase is -1. Lay et al. (1983a) estimate the reflection coefficient as .96 for pP. We further argue that pP interacts with the same part of the surface as does P. This assumption is good for the depths of the mesa tests which range from .5 to 1.4 kilometers. The width of the boxcar is .85 seconds; this estimate of the pP - P lag is taken from Lay et al. (1983a). We further convolve a short period instrument and a Futterman Q operator in these synthetics. We use a Haskell function with parameters (B = 2,K = 10) while Lay et al. (1983a) use slightly different values (B = 1,K = 8).

In Figure 2.14 we display the results of the convolutions. The first column contains the initial Kirchhoff-Helmholtz synthetics with peak amplitudes taken from Figure 2.10. The second column shows these synthetics convolved with a WWSSN short period instrument and a boxcar. We introduce apparent additional complexity into the waveform but do not change the range of peak amplitudes significantly when we include an instrument and pP. The structural complexity of the waveform is masked by the dominant interference between P and pP.

We next convolve these synthetics with Futterman Q operators with a t^* = .5 and 1. The waveforms and their ab amplitudes are displayed in columns 3 and 4. We plot the ab amplitudes as a function of azimuth for both sources and t^* values in Figure 2.15. We remove the complexity of the waveform for both sources with the two t^* values. However, there are some observable differences in the first and third peaks of the waveforms as a function of azimuth. The first peak widens as the azimuth increases. The third peak becomes smaller and disappears altogether. Moreover, we produce a variation of ab amplitudes as a function of azimuth of 2½ for source D if t^* is .5, as seen in Figure 2.15. However, when t^* is 1, this variation reduces to a factor of 1.7 as a function of azimuth. Notice that we also obtain a variation of 2½ of ab amplitudes with respect to source position if t^* is .5. This occurs at $\theta = 0°$ and $\theta = 45°$; however, the difference between ab amplitudes for the two sources decreases as the azimuth increases.

Thus we cannot predict the observed ab amplitude variation as a function of azimuth or station location if we use a structure on the Moho 10

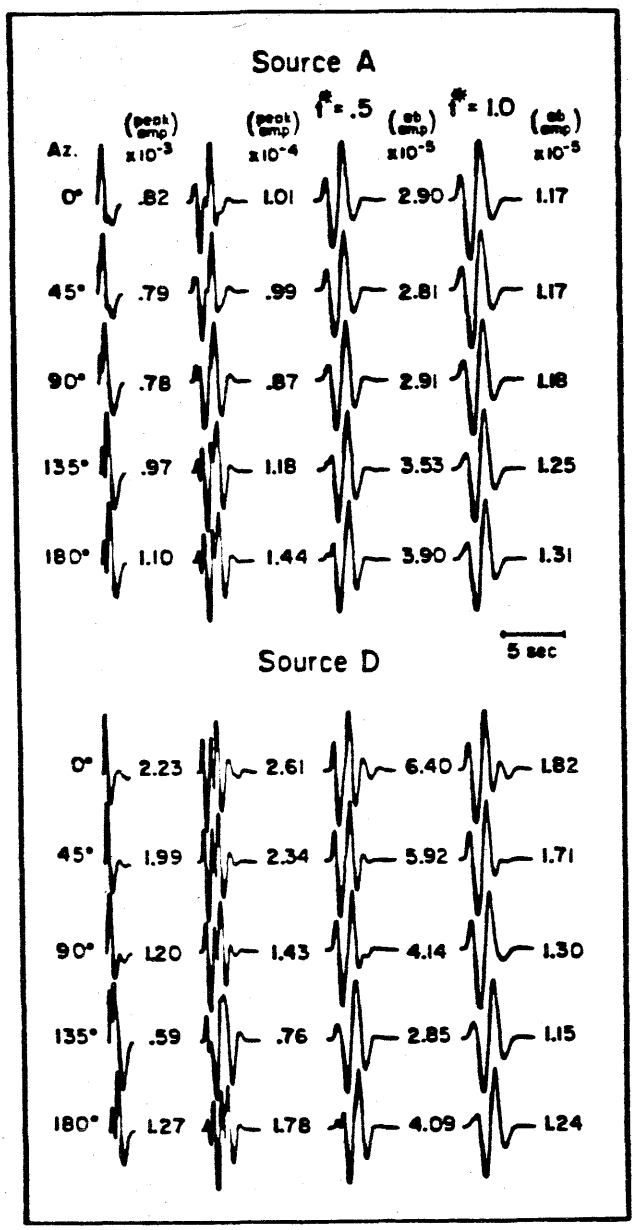

Figure 2.14. Kirchhoff-Helmholtz responses (first column) convolved with a box-car of width .85 seconds and a short period WWSSN instrument (second column) and, then, a Q operator with t* values of .5 (third column) and 1 (fourth column). Responses are from a distance of 4000 kilometers, azimuth range of 0° to 180° and source locations A and D.

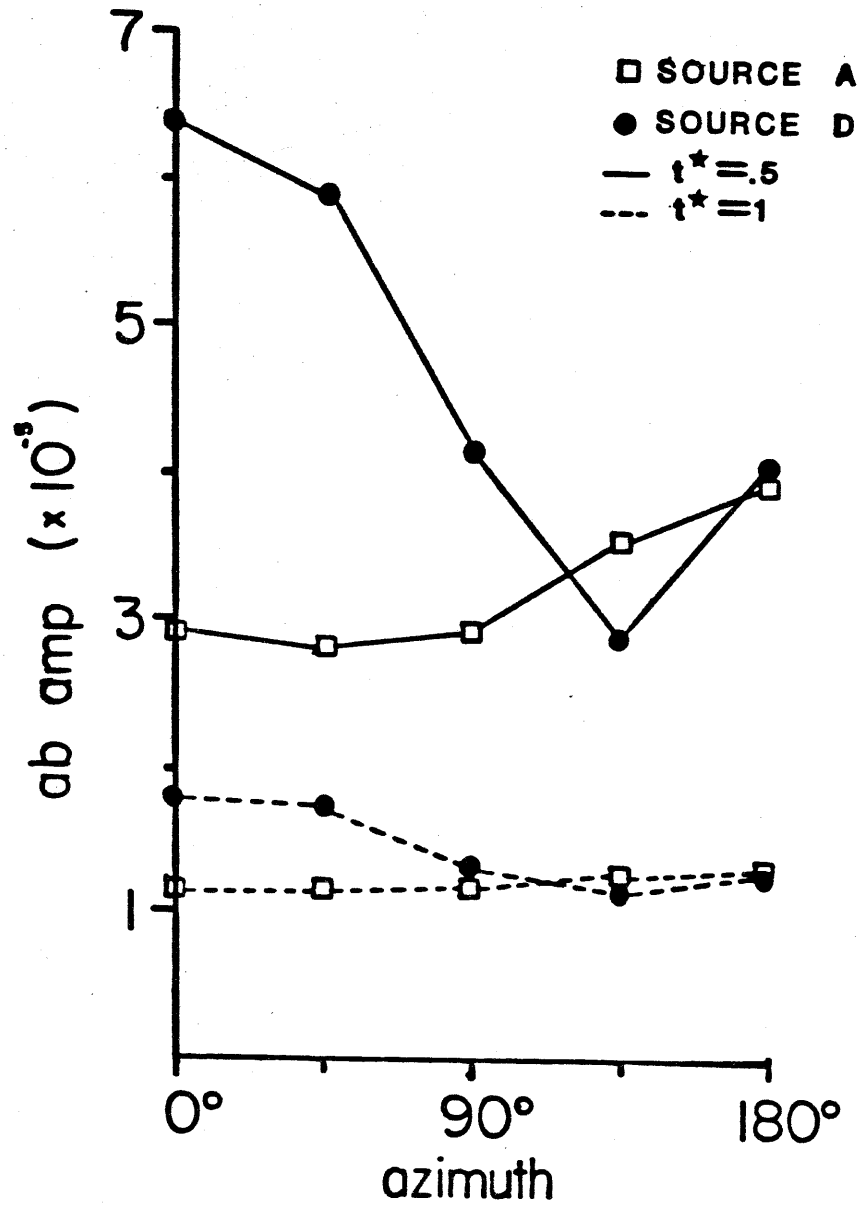

Figure 2.15. ab amplitudes from synthetics in Figure 2.14 plotted as a function of azimuth for both source locations A and D and both t^* values.

kilometers high and approximately 25 kilometers wide. If one believes that the factors of 12 or 40 in Figures 2.3, 2.4, and 2.5 are true measures of a purely near source phenomena, then one requires a structure several hundred kilometers in scale on a boundary to match these factors. This structure would distort the waveform considerably. Yet there is no obvious evidence in the seismograms for a correlation between low amplitudes and complicated and/or broadened waveforms or high amplitudes and simple, impulsive waveforms. We speculate that, rather than a large structure on a single boundary, a small velocity or density perturbation along a several hundred kilometer ray path may produce the desired amplitude change. However, we have no way of testing this speculation with our method.

On the other hand, we do predict the factor of 2½ in ab variation with respect to source location if t* is .5. This variation is not accompanied by any significant waveform distortion. Although we only produce a factor of 2½ at two azimuths, this result is an artifact of the source moveout across the structure. If sources were uniformly distributed over the structure, we would produce this same magnitude of variation at all the azimuths. Furthermore, no source would be systematically higher in ab amplitudes than another source at all the azimuths. Unfortunately, we cannot tell from Figure 2.3 whether there are any systematics with respect to source location. The data should certainly be examined for such trends.

We also note that the travel time residuals do not correlate with the ab patterns. The convolution with two t* values demonstrates the frequency dependence of the phenomena. If t* is larger than 1, we will produce a flat

pattern with azimuth but the travel time residuals will not change. Thus we do not expect a systematic relationship between travel time and amplitude anomalies because the ab amplitudes are sensitive to Q but the travel times are relatively stable. This is an unfortunate result because such a correlation would be diagnostic of structure as opposed to tectonic release. We do not expect fault slip to produce travel time anomalies. As yet, there has been no study which definitively demonstrates a relationship or lack thereof. The data sets of amplitude and travel time measurements do not have a one-to-one correspondence. Lay et al. (1983a) measure the ab amplitudes off short period WWSSN instruments while Minster et al. (1981) and Spence (1974) use culled travel time measurements from the ISC catalogs. We clearly need a study which compares the travel time and amplitude from the same seismogram.

The largest overall variation in ab amplitude with azimuth in Figure 2.15 occurs because of differences in t* values. Yet any corresponding changes in the waveform are unnoticeable. Thus the ab amplitudes are far more sensitive than waveforms to Q differences. Perhaps a lateral variation of Q with path can produce the extreme scatter of ab amplitudes for both tests inside and outside the mesa. However, it cannot explain the differences in patterns between these different test site areas. If the near mesa anomalies are at least a factor of 10, then structure on the Moho which is compatible with travel time residuals cannot produce these large variations of amplitude with azimuth. However, such a structure could explain the observed variation of ab amplitudes with source position at a given station.

REFERENCES

Aki, K. and Y.-B. Tsai (1972), "Mechanism of Love-wave excitation by explosive sources," J. Geophys. Res., 77, 1452-1475.

Butler, R. (1984), "Azimuth, Energy, Q and Temperatures: Variation on P wave amplitudes in the United States," Review of Geophysics and Space Physics, 22, 1-36.

Haddon, R. and P. Buchen (1981), "Use of the Kirchhoff"s formula for body wave calculations in the Earth," Geophys. J. R. astr. Soc., 67, 587-598.

Hilterman, F. (1975), "Amplitudes of seismic waves - A quick look," Geophys., 40, 745-762.

Hong, T. L. (1978), *Elastic Wave Propagation in Irregular Structures* (Thesis, California Institute of Technology).

Langston, C. and D.V. Helmberger (1975), "A procedure for modelling shallow dislocation sources," Geophys. J. R. astr. Soc., 42, 117-130.

Langston, C. (1977), "The effect of planar dipping structure on source and receiver responses for constant ray parameter," Bull. Seism. Soc. Am., 67, 1029-1050.

Lay, T., T.C. Wallace, and D.V. Helmberger (1983a), "The effects of tectonic release on short-period P waves from NTS explosions," submitted to Bull. Seism. Soc. Am..

Lay, T., L.J. Burdick, D.V. Helmberger, and C.G. Arvesen (1983b), "Estimating seismic yield and defining distinct test sites using complete waveform information," Woodward-Clyde Report, WCCP-R-84-01.

Minster, J.B., J.M. Savino, W.L. Rodi, T.H. Jordan, and J.F. Masso (1981),

"Three-Dimensional velocity structure of the crust and upper mantle beneath the Nevada test site," Systems, Science, and Software Report, SSS-R-81-5138.

Mow, C. and Y. Pao (1971), *The Diffraction of Elastic Waves and Dynamic Stress Concentrations*, #R-482-PR, A report prepared for United States Air Force Project Rand.

Nuttli, O. W. (1969), "Travel times and amplitudes of S waves from nuclear explosions in Nevada," Bull. Seism. Soc. Am., 59, 385-398.

Spence, W. (1974), "P-wave residual differences and inferences on an upper mantle source for the Silent Canyon volcanic centre, Southern Great Basin, Nevada," Geophys. J. R. astr. Soc., 38, 505-523.

Stratton, J. A. (1941), *Electromagnetic Theory*, First Edition, McGraw-Hill Book Company, Inc., New York.

Wallace, T.C., D.V. Helmberger, and G.R. Engen (1983), "Evidence of tectonic release from underground nuclear explosions in long-period P waves," Bull. Seism. Soc. Am., 73, 593-813.

Chapter 3

The gradient Kirchhoff-Helmholtz solution as a tool for modeling CMB relief

Introduction

The degree of irregularity of the core-mantle boundary (CMB) is still unknown. Short and long period seismic phases which interact with the core, such as P_{diff}, PcP, ScS, PKP, PKIKP, and PKKP frequently have travel time and amplitude anomalies or unusual precursors. These anomalies cannot be interpreted uniquely as a result of CMB topography. The existence and extent of undulations of the CMB has implications for understanding of coupling of the Earth's magnetic and gravitational field (Hide and Malin, 1970), the nature of convection in the Earth's interior (Hager et al., 1984), and the history of the Earth's accretion (Stevenson, 1981; Schloessin, 1974). A more acute examination of this explanation of the anomalous seismic data requires an ability to quantitatively model the impact of CMB shapes on seismic waves. The CMB shapes must be mechanically feasible. If the CMB shapes inferred from modeling are too extreme to exist, it must be concluded that the seismic data under consideration are primarily influenced by other factors and have no bearing on the CMB shape question.

In the present study we investigate the size of CMB undulations needed to produce observed travel time and amplitude anomalies of long and short period SHcSH reflections. The propagation of this phase is relatively simple to model because the potentials and displacements in both homogeneous and inhomogeneous media are governed either exactly or approximately by the

scalar wave equation. Furthermore, the amplitude and travel time anomalies of these waves are well documented and, in many cases, the gross upper mantle and crustal effects have been removed (Jordan and Lynn, 1974; Lay, 1983; Mitchell and Helmberger, 1973; Hales and Roberts, 1970b). As in the previous chapters, the Kirchhoff-Helmholtz integral is used to model these waves. In addition to using the half-space reflected Kirchhoff-Helmholtz method discussed in Chapter 1, we implement a modification of the technique that includes a variable velocity in the medium which contains the source and receiver. The Kirchhoff-Helmholtz technique integrates potentials over an intermediate surface between the source and receiver; thus, it is a natural choice for modeling topography on a major physical discontinuity of the Earth. Moreover, the technique provides insight into the relative effect of CMB bumps on short and long period body waves.

Description of the Modeling Technique

This section describes the method used to calculate SH waves which propagate through a medium with a radially symmetric velocity function and reflect off a distorted boundary. A detailed description of the method for an acoustic isovelocity half space Kirchhoff-Helmholtz solution can be found in Chapter 1. The relevant result from that study is that numerical Kirchhoff-Helmholtz solutions for SH reflections from a rigid sphere compare well with high frequency analytical solutions. Consequently, we can use this technique to model SH waves interacting with an irregular CMB with confidence.

The previous approach is extended here to allow an inclusion of velocity gradients in the propagating medium. Although one can expect the two K-H solutions to give similar results for SHcSH phases, such a modification allows us to model core phases with more complicated propagational paths such as SKKS and PKIKP. This section outlines a practical procedure for implementation of the gradient K-H method.

Sobolev (1930) shows that the Kirchhoff formula can be generalized for propagation in heterogeneous material. The formalism here is similar to that of Haddon and Buchen (1981) and Sinton and Frazier (1982). We differ from Haddon and Buchen in that we allow the surface over which we integrate to deviate from spherical symmetry. In contrast to Sinton and Frasier, we integrate in the time domain. We suppose the existence of a potential φ in a heterogeneous volume V which obeys the wave equation.

$$\frac{1}{\beta(x,y,z)^2}\frac{\partial^2\varphi}{\partial t^2} - \nabla^2\varphi = \Phi \tag{3.1}$$

From the scalar integral representation theorem, we write the potential as a linear surface integral over ∂V, the surface of V,

$$\varphi(\underline{\varepsilon},t) = \int_{\partial V}[G(\underline{x},\underline{\varepsilon},t)*\underline{\nabla}\Phi(\underline{x},t) - \Phi(\underline{x},t)*\underline{\nabla}G(\underline{x},\underline{\varepsilon},t)]\cdot\underline{n}(\underline{x})dS + f(\underline{\varepsilon},t) \tag{3.2}$$

where $\varphi(\underline{\varepsilon},t)$ is not on the surface and $f(\underline{\varepsilon},t)$ is the direct wave which is dependent on the source. The form of this equation is identical to the half-space Kirchhoff-Helmholtz integral. The difference is that G, the Green's function , is governed by

$$\frac{1}{\beta(x,y,z)^2}\frac{\partial^2 G}{\partial t^2} - \nabla^2 G = \delta(t - t_o)\delta(\underline{\xi} - \underline{x}) \quad . \tag{3.3}$$

We emphasize that the propagation of shear and compressional waves in a heterogeneous medium is approximately governed by two wave equations if the fractional variation of ρ, μ, and λ over a wavelengtn of the disturbance is small (Ewing et al., 1957) everywhere except over material boundaries. If these conditions are not met, equation (3.1) and (3.2) are invalid.

We invoke a further approximation and use geometric ray theory to estimate Φ and G on the reflective surface. This assumption is appropriate for precritical high frequency SHcSH reflections which are far field disturbances and have paths with no turning points. The preceding theory does not exclude phases which go through turning points and are described by WKBJ solutions. However, for SHcSH, geometric ray theory is sufficient. Therefore, the Green's function on the surface ∂V is approximated by

$$G = \frac{\delta(t - \tau_\varepsilon)}{4\pi S_\varepsilon} \tag{3.4}$$

where S_ε and τ_ε are the spreading factor and travel time , respectively, of a ray traveling from $\underline{x}$, a point on the surface ∂V, to $\underline{\xi}$, the receiver. Similarly, Φ on the surface is well approximated by

$$\Phi = \frac{D\, f(t - \tau_o)}{S_o} \tag{3.5}$$

S_o and τ_o are the spreading and travel time of a ray traveling from $\underline{x}_o$, the source location, to $\underline{x}$, a point on the reflecting surface. Figure 3.1 shows the

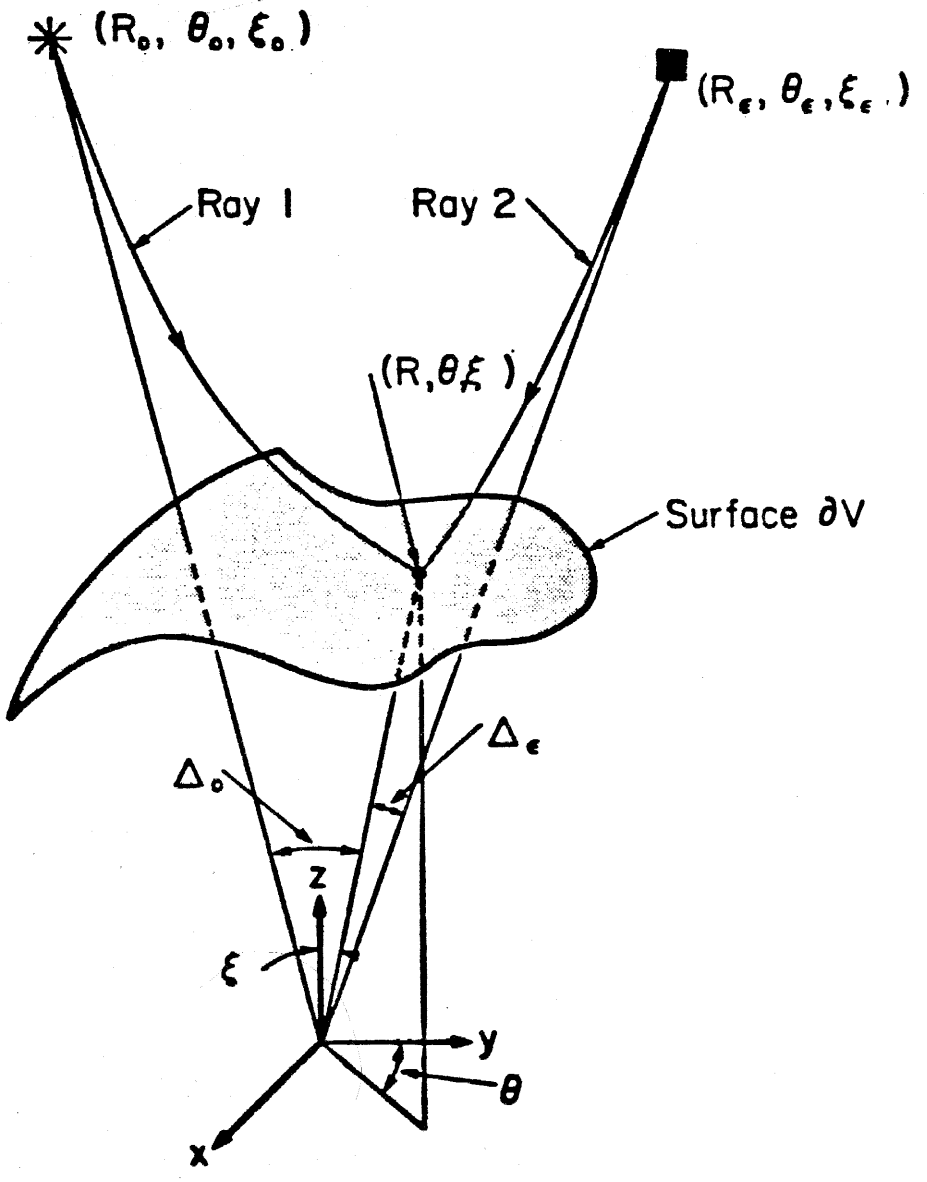

Figure 3.1. Display of source-receiver geometry showing the source position $\underline{x}_o = (R_o, \theta_o, \xi_o)$, the receiver position $\underline{x} = (R_\epsilon, \theta_\epsilon, \xi_\epsilon)$, and the surface position $\underline{x} = (R, \theta, \xi)$ coordinates. These angles are defined with respect to the coordinate system shown below the surface. Δ_o and Δ_ϵ are also shown.

source, receiver and surface position and the relevant ray paths. $f(t)$ is the source time function and is specified to be the first derivative of an isotropic Haskell source, as in Chapters 1 and 2. D is a plane wave reflection coefficient dependent on the angle between the local normal to the surface and the incident angle of the ray impinging on the surface. Here we have invoked the tangent plane hypothesis as discussed in Chapters 1 and 2. $\frac{\partial G}{\partial n}$ and $\frac{\partial \Phi}{\partial n}$ are estimated as follows:

$$\frac{\partial \Phi}{\partial n} \cong \frac{D\dot{f}(t-\tau_o)}{S_o} \underline{\nabla \tau_o} \cdot \underline{n} \tag{3.6}$$

$$\frac{\partial G}{\partial n} \cong \frac{\dot{\delta}(t-\tau_\varepsilon)}{4\pi S_\varepsilon} \underline{\nabla \tau_\varepsilon} \cdot \underline{n} \quad . \tag{3.7}$$

These estimates are obtained by assuming that the amplitude factors S_o, S_ε, and D vary slowly over the surface compared to the phase.

The Eikonal equation

$$\underline{\nabla \tau} \cdot \underline{\nabla \tau} = \frac{1}{\beta(x,y,z)^2} \tag{3.8}$$

states that $\underline{\nabla \tau_o}$ and $\underline{\nabla \tau_\varepsilon}$ are vectors which are parallel to the normal of the wavefront at all points along the ray paths and which have lengths of $\frac{1}{\beta(x,y,z)}$. Hence,

$$\underline{\nabla \tau_o} \cdot \underline{n} = \frac{\cos\psi_o}{\beta(x,y,z)} \tag{3.9}$$

$$\underline{\nabla \tau_\varepsilon} \cdot \underline{n} = \frac{\cos\psi_\varepsilon}{\beta(x,y,z)} \tag{3.10}$$

where ψ_o and ψ_ε are the angles between the rays and the local normal and $\beta(x,y,z)$ is the velocity just above the surface. Substitution of expressions (3.4), (3.5), (3.6), (3.7), (3.9) and (3.10) into the integral (3.2) yields

$$\varphi(\underline{\varepsilon},t) = \frac{1}{4\pi\beta}\int_{\partial V}\frac{D}{S_o S_\varepsilon}\dot{f}\,(t-\tau_o-\tau_\varepsilon)(\cos\psi_o + \cos\psi_\varepsilon)dS \quad . \qquad (3.11)$$

We evaluate equation (3.11) numerically. Haddon and Buchen (1981) evaluate the identical equation but they select the two-way travel time and azimuth to parameterize ∂V. Their choice reduces integral (3.11) to a one-dimensional convolution. This transformation can be accomplished only for symmetric surfaces. In their approach, the Jacobian associated with the two-way travel time and azimuth was analytically calculated assuming spherical symmetry of the surface. This specialization is inappropriate for the problem at hand and the integral is parameterized using the spatial coordinates on the CMB.

The method of integration is a summation of single point evaluations of the integrand and requires estimations of D, τ_o, τ_ε, S_o, S_ε, $\cos\psi_o$, and $\cos\psi_\varepsilon$ as a function of position on ∂V. The reflection coefficient is 1 everywhere on the surface. This value is appropriate for a plane SH reflection from a flat interface between a solid and fluid. The same reflection coefficient is used for the isovelocity half-space Kirchhoff-Helmholtz modeling. This reflection coefficient ignores the possibility that topography on the CMB polarizes SH displacements into P or SV displacements. This assumption is probably justified here because the surface normal does not greatly differ from the radial direction in the topographies we model. If polarization is important. it is expected that the amplitude anomalies calculated here due to focusing-

defocusing by the boundary provide a lower bound on the effect of CMB topography.

The velocity of the propagational medium is a function of radius. Thus, we can use conventional ray theory for spherically symmetric Earth (Bullen, 1965) to calculate τ_o, τ_ε, S_o, S_ε, $\cos\psi_o$, and $\cos\psi_\varepsilon$ at each point on the surface. Then the travel times, spreading factors, and ray parameters are dependent only on R, R_o , R_ε , Δ_o, and Δ_ε. These parameters are displayed in Figure 3.1.

We integrate equation (3.11) in the following manner. The surface is described by a Cartesian function z(x,y) as in previous chapters. ΔS, the discretized area element of ∂S, and $\underline{n}$ are calculated from z(x,y) with simple calculus formulas. The topography is converted to spherical coordinates (R,θ,ξ) . Given these coordinates and the source location (R_o,θ_o,ξ_o) and the receiver location $(R_\varepsilon,\theta_\varepsilon,\xi_\varepsilon)$ we calculate Δ_o and Δ_ε with these identities:

$$\cos\Delta_o = \sin\xi_o \cos\theta_o \sin\xi \cos\theta + \sin\xi_o \sin\theta_o \sin\xi \sin\theta + \cos\xi_o \cos\xi \quad (3.12)$$

$$\cos\Delta_\varepsilon = \sin\xi_\varepsilon \cos\theta_\varepsilon \sin\xi \cos\theta + \sin\xi_\varepsilon \sin\theta_\varepsilon \sin\xi \sin\theta + \cos\xi_\varepsilon \cos\xi \quad (3.13)$$

We next search through a table containing travel times, spreading factors, and ray parameters as a function of R and Δ, given the quantities R, Δ_o, and Δ_ε. R_o is equal to R_ε in all calculations of this study. The table is searched twice for each surface point; these two searches find 1) the ray which goes from the source to the surface and 2) the ray which goes from the surface to the receiver. We obtain the ray information and compute the two-way travel time $\tau=\tau_o+\tau_\varepsilon$, the product of the spreading factors $\frac{1}{S_o S_\varepsilon}$, and the sum of

the cosine factors $\cos\psi_o + \cos\psi_\varepsilon$ for all points on the surface. The cosine factors are calculated from the ray parameters and the direction of the local normal with the following expressions:

$$\cos\psi_o = \cos\alpha \left[1-(\frac{\beta p_1}{R})^2\right]^{\frac{1}{2}} - (\frac{\beta p_1}{R}) \sin\alpha \qquad (3.14)$$

$$\cos\psi_\varepsilon = \cos\alpha \left[1-(\frac{\beta p_2}{R})^2\right]^{\frac{1}{2}} + (\frac{\beta p_2}{R}) \sin\alpha \ . \qquad (3.15)$$

The angles ψ_o, ψ_ε, and α are shown in Figure 3.2. α is the complementary angle of $\underline{n} \cdot \underline{R}$. Formula (3.15) is based on a coplanar assumption and is sufficiently accurate for the surfaces and source-receiver positions in this chapter.

The ray information is generated by tracing a family of rays through an Earth comprised of several 100 kilometer thick homogeneous shells. Table 3.1 shows the velocity model used to calculate this information. For all the calculations in this chapter the density of the receiver and source, ρ_o and ρ_ε, is 3 gm/cc and the density of the medium just above the surface, ρ, is 5 gm/cc. We obtain $\frac{dp}{d\Delta}$ by differencing and using the following expression from Ben-Menahem and Singh (1981) to compute spreading of the up and downgoing ray at a given radius R:

$$S_i^{-1} = C_i \left[\frac{p_i}{\sin\Delta_i} \left| \frac{dp_i}{d\Delta_i} \right| (\eta_i^2 - p^2)^{-1/2} (\eta^2 - p^2)^{-1/2}\right]^{\frac{1}{2}} \qquad (3.16)$$

where

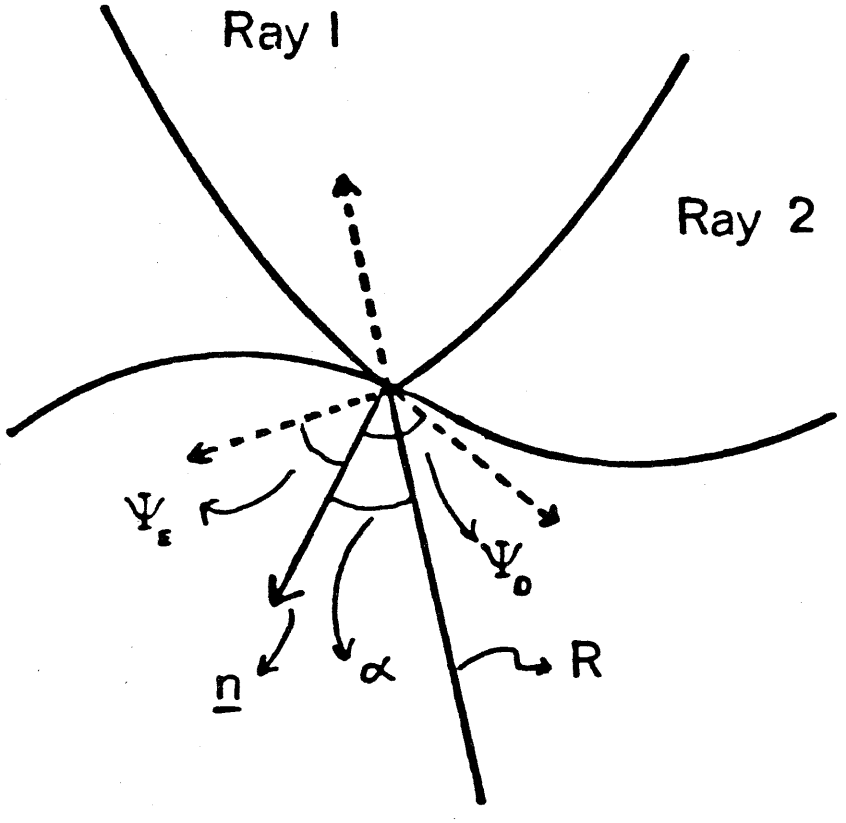

Figure 3.2. Close up of angles ψ_o, ψ_e, α and the normal $\underline{n}$.

Table 3.1

Radius (km)	velocity km/sec
6371	4.36
6271	4.45
6171	4.60
6071	4.76
5971	4.96
5871	5.10
5771	5.66
5671	5.90
5571	6.13
5471	6.23
5371	6.36
5271	6.45
5171	6.50
5071	6.55
4971	6.62
4871	6.66
4771	6.73
4671	6.78
4571	6.83
4471	6.88
4371	6.93
4271	6.97
4171	7.02
4071	7.07
3971	7.12
3871	7.17
3771	7.21
3671	7.26
3571	7.30

$$C_o = \left(\frac{\eta}{R\eta_o}\right)\left[\frac{R_o\rho_o}{R\rho}\right]^{1/2} \text{ and } C_\varepsilon = \left(\frac{\eta_\varepsilon}{R_\varepsilon\eta}\right)\left[\frac{R\rho}{R_\varepsilon\rho_\varepsilon}\right]^{1/2}.$$

Here $\eta_i = \frac{R_i}{\beta_i}$ and ρ_i is the density. p is equal to $\frac{R_o \sin i}{\beta}$.

When the local angle between the normal and the incident ray exceeds the critical angle, the surface is not illuminated. This constraint places a limit on the area of the integrated surface as a function of source-receiver separation. Figure 3.3 demonstrates this fact. A ray traveling through a JB Earth reaches critical at 44°. The maximum area of illuminated surface occurs when the source and receiver are coincident. As the source and receiver separate, the integrated surface shrinks. We are unable to calculate a synthetic past a source-receiver separation of 70°.

The range of takeoff angles and the increment of angle Δi of the ray family depend on the source and receiver positions and the density of ray information needed to produce a smooth solution. The ray information is retained at a prescribed range of R and increment ΔR. The range of R is based on the maximum height of the topography. In practice, we constrain the topography to be less than or equal to 100 kilometers above the CMB. The velocity within this 100 kilometer shell is a constant 7.3 km/sec. The underlying medium is a fluid core. The increment ΔR must alsc be fine enough to produce a smooth answer. The functions $S_o^{-1}, S_\varepsilon^{-1}$, τ and takeoff angle as a function of R and Δ are shown in Figure 3.4. The ray information is retained for 10 kilometer subshells starting at R equal to 3571 kilometers and ending at R equal to 3471 kilometers and is displayed for every other

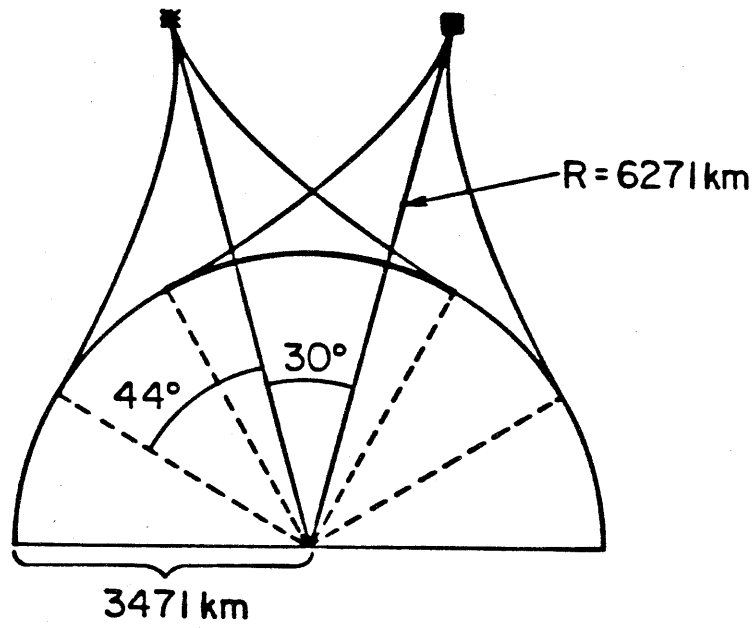

Figure 3.3. A diagram which displays the progressive shrinking of the surface area over which we integrate geometric ray information as the source and receiver separate.

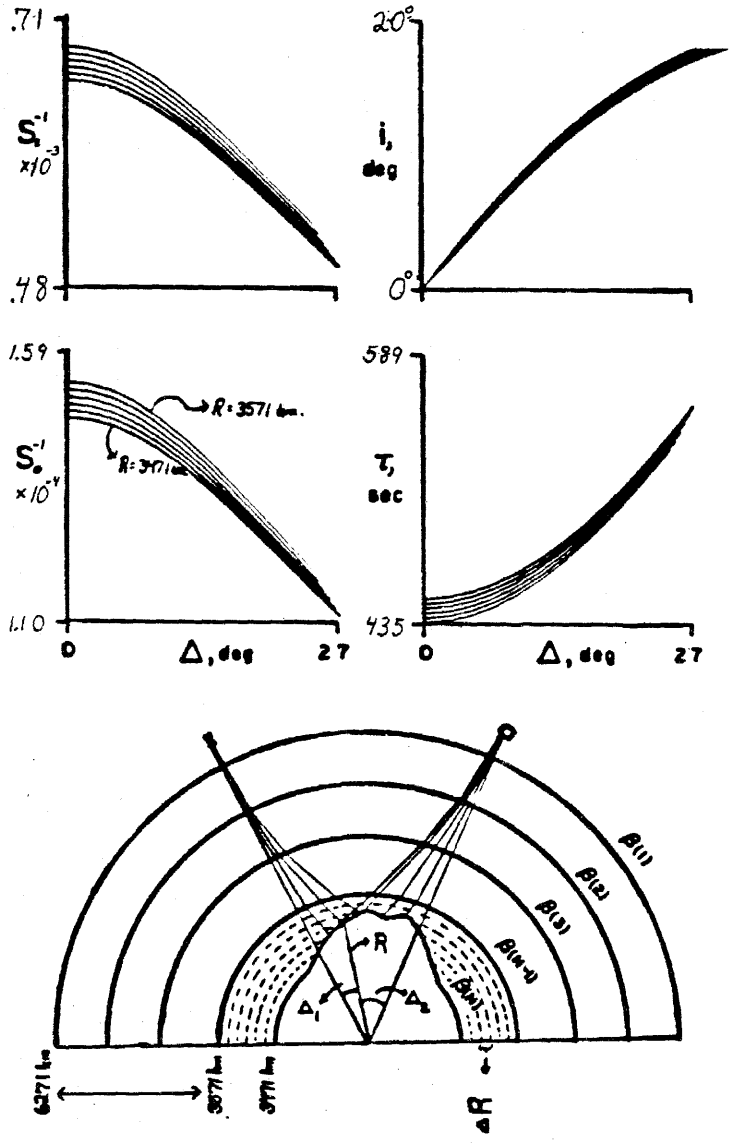

Figure 3.4. Plots of functions of S_t^{-1}, S_o^{-1}, $i°$, and τ as a function of Δ and R. R ranges from 3571 to 3471 kilometers, shown in increments of 20 kilometers. Below the graphs is a schematic diagram demonstrating how the ray information is determined for each point on the bumpy surface.

subshell in this figure. A schematic diagram below these functions shows the final 100 kilometer shell broken into subshells and the intersection of the topography with these subshells.

After obtaining the spreading factors, the two-way travel times, the cosine sums, and ΔS, we calculate the contributions to the integral at each point. We then sort and add the contributions according to increasing τ to construct a numerical ramp response. Finally, we convolve the third derivative of a Haskell isotropic source with this numerical ramp response to obtain the time derivative of φ as in previous chapters.

Examples and Comparisons

The modified Kirchhoff-Helmholtz method is tested in three ways. First, we specify an isovelocity model and a spherical CMB. Then the modified K-H technique should give the same results as the first motion solution of Chapter 1 for an SH wave reflecting off a rigid sphere. Secondly, we now allow the SH wave to propagate through a JB Earth; the CMB remains a sphere. Then the modified K-H solution should be the same as geometric ray solutions for a core reflection. Finally, we input an isovelocity model but allow the CMB to deviate from spherical symmetry. Then both the modified K-H solution and the half-space K-H solution should be the same. These three tests are not absolute measures of accuracy but do verify the self-consistency of the method. Moreover, the tests highlight some difficulties with the modified K-H technique.

A profile of synthetics generated for the first test is shown in Figure 3.5. These waveforms are SHcSH reflection which travel through a homogeneous Earth with a velocity of 7.3 km/sec. and reflect off a spherical CMB. The peak source strength, calculated by convolving the third derivative of a Haskell source (B = 0, k = 2) with a pure ramp, is 0.448 . The spreading formula used to calculate theoretical amplitudes is taken from equation (1.21) in Chapter 1. The parameters of that formula are shown in the diagram above the synthetics. The numerical and theoretical peak amplitudes adjacent to the synthetics compare well. As the source and receiver separate, the noise increases until it significantly contaminates the solution at 70°.

There is a simple explanation for the progressive jitter in the synthetics as the source and receiver separate. Unlike the half-space K-H method, the modified technique depends on a sufficient number of rays and a fine ΔR as well as an adequate discretization of the topography. We calculate a simple reflection off a sphere to assess the relative impacts of the coarseness of the gridding of the topography versus the number of rays and increment of takeoff angle. The source signal wavelength is 35 kilometers which exceeds the grid length of the surface elements in all cases. Figure 3.6 demonstrates that the ray density controls the numerical noise of the seismogram much more than the coarseness of the grid. The seismograms calculated with 197 rays at an increment of .1° are all badly contaminated with noise because the ray family does not illuminate the sphere with a sufficient density of ray information for a smooth solution. The length of an element comprising the surface varies from 4.49 kilometers (seismogram A) to 9.03 kilometers

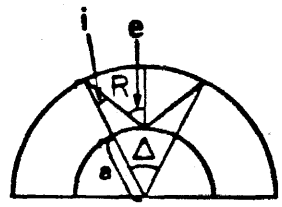

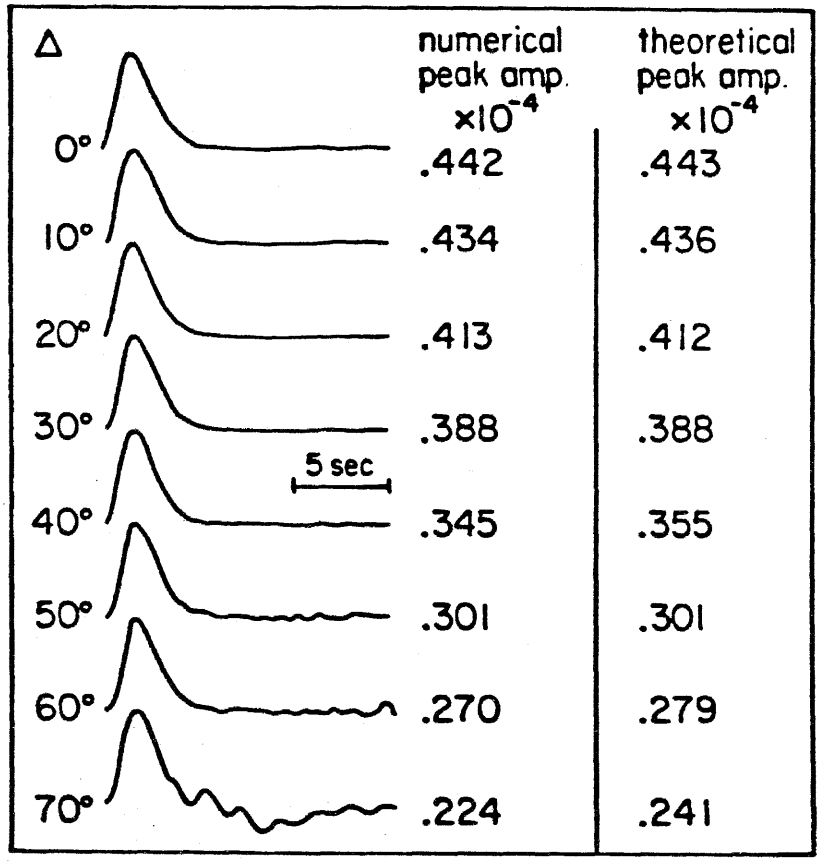

Figure 3.5. Reflections off a sphere which have propagated through a constant velocity Earth ($\beta = 7.3$ km/sec). Parameters from equation (1.21) used to calculate the theoretical amplitude are defined in the top diagram. Source-receiver radius is 6271 kilometers and CMB radius is 3471 kilometers.

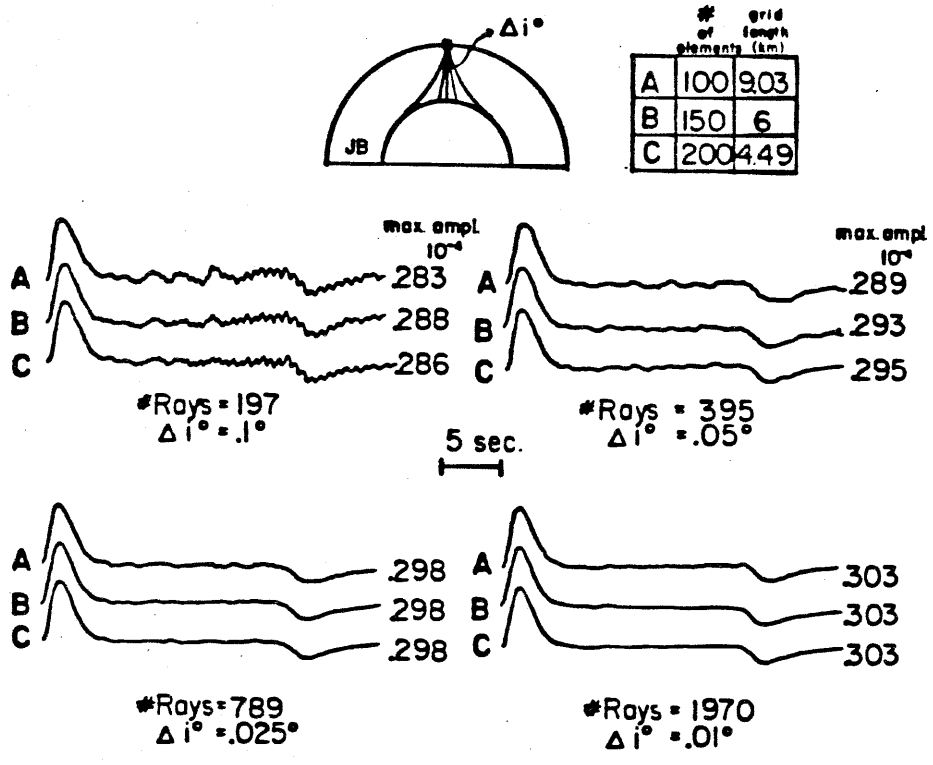

Figure 3.6. Four sets of synthetics which correspond to calculations performed with the number of rays and increment of takeoff angle shown below the set. Synthetics A, B, and C corresponds to calculations done with the number of elements and grid size shown in the upper right table. Source-receiver radius is 6271 kilometers. CMB radius is 3471 kilometers.

(seismogram C). However, the increment of arclength subtended by Δi = .1° varies from 7 kilometers for the surface illuminated by near vertical rays to 50 kilometers for the surface illuminated by near grazing incidence rays. For this particular source-receiver geometry, the elements which are illuminated by grazing incidence rays contribute to the response at a later time. Thus the numerical noise in the synthetic increases as a function of time. In contrast, synthetics computed with 1970 rays at an increment of Δi of .01° are smooth. The arclength subtended by .01° varies from .7 kilometer to 6.8 kilometers. There is also a longer period truncation phase at the end of all the synthetics in Figure 3.6. This truncation phase originates from the finiteness of the grid, as discussed in Chapter 2.

We next calculate synthetics which propagate through a JB Earth and reflect off a spherical CMB and verify that the peak amplitudes of the Kirchhoff synthetics are predicted by spreading. The expression for the spreading of a reflected core phase is from Ben-Menahem and Singh (1981). The amplitude of a reflected phase at the free surface is, assuming the source and receiver are several wavelengths away from the CMB,

$$u = P_0 ZGF \tag{3.18a}$$

where P_0 is the source strength. Z is the square root of the ratio of the energy transported to a unit area of the CMB by the incident wave and the energy transported away from the CMB by the reflected wave. F is the radiation function and is equal to 1 since we specify an isotropic source. Because there is no mode conversion, Z is also equal to 1. Therefore, the expression

reduces to

$$G = \frac{1}{R_o}\left[\frac{\rho_o \beta_o}{\rho_\varepsilon \beta_\varepsilon}\,\frac{\sin i_o}{\sin\Delta\cos i_\varepsilon}\left|\frac{di_o}{d\Delta}\right|\right]^{1/2} . \qquad (3.18b)$$

The results of the second test are shown in Figure 3.7. As in the first test, the source strength is 0.448 . The two sets of numbers agree. Table 3.2 gives the grid and ray family parameters used to calculate these synthetics.

Table 3.2

Δ (°)	# of elements	element size (km)	# of rays	Δi
0	150 x 150	6 x 6	788	.025
10	150 X 150	6 x 6	788	.025
20	150 x 150	6 x 6	788	.025
30	150 x 150	6 x 6	788	.025
40	150 x 150	6 x 6	1967	.010
50	200 x 200	6 x 6	1967	.010
60	200 x 200	6 x 6	1967	.010

In addition to prescribing a greater density of rays, we also enlarge the grid at larger values of Δ to eliminate a truncation phase. This phase cannot be avoided when Δ is equal to 70° because the code computes 4 seconds of response at this distance.

Finally, the third test establishes that the modified K-H code and the half-space code produce the same result if the surface deviates from spherical symmetry and the velocity model is constant. The results are shown in

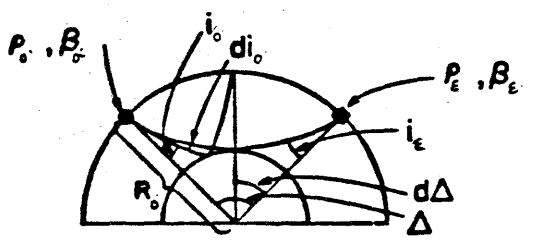

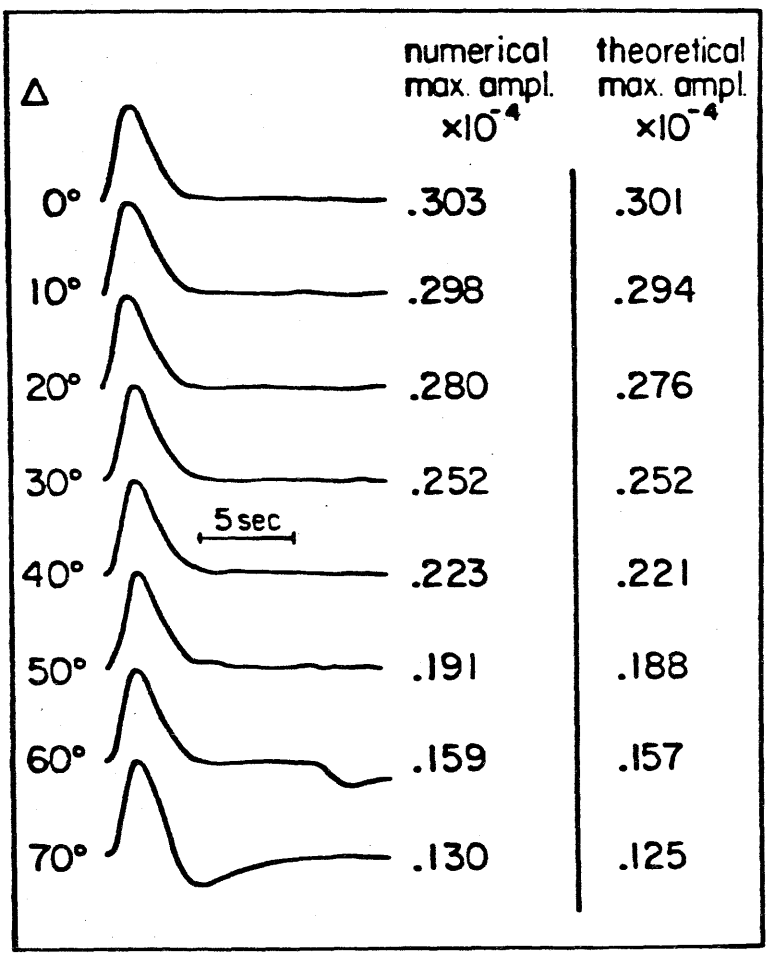

Figure 3.7. Reflections off a sphere which propagate through a JB Earth. Parameters from equation (3.18) are defined in diagram above. Source-receiver radius is 6271 kilometers. CMB radius is 3471 kilometers.

Figure 3.8. The SHcSH synthetic propagates through a medium with a velocity of 7.3 km/sec and reflects off a plateau 10 kilometers high and 100 kilometers wide. The solutions are almost the same at 0°. However, the peak amplitudes differ by 10 to 30% as Δ increases because of inadequate interpolation in the modified K-H technique.

These three tests demonstrate the consistency of the modified K-H solution with geometrical optics solutions and with half-space K-H solutions. We now present some solutions of SHcSH waves propagating through a JB Earth and reflecting off a distorted CMB. The first example is shown in Figure 3.9. The topography on the CMB is described by

$$z = \left[3471^2 - (x^2 + y^2)\right]^{\frac{1}{2}} \quad \text{if} \quad (x^2 + y^2)^{\frac{1}{2}} > \frac{w}{2} \tag{3.19}$$

and

$$z = \left[3471^2 - (x^2 + y^2)\right]^{\frac{1}{2}} + c \quad \text{if} \quad (x^2 + y^2)^{\frac{1}{2}} \leq \frac{w}{2} .$$

The height, c, is 10 kilometers and the width, w, varies from 0 to 200 kilometers. This formula describes an abrupt plateau centered at the midpoint on an otherwise spherical CMB. The plateau causes a precursory reflection which arrives 2.66 seconds early. The precursor grows in amplitude as the width of the plateau increases. There is no anomaly in amplitude or travel time in the synthetic reflection from the plateau with w equal to 50 kilometers. Thus there is a characteristic size of a shape which is undetectable by short period data. Overall there is not much reduction in the peak amplitudes. Clearly, much broader topographies are required to produce

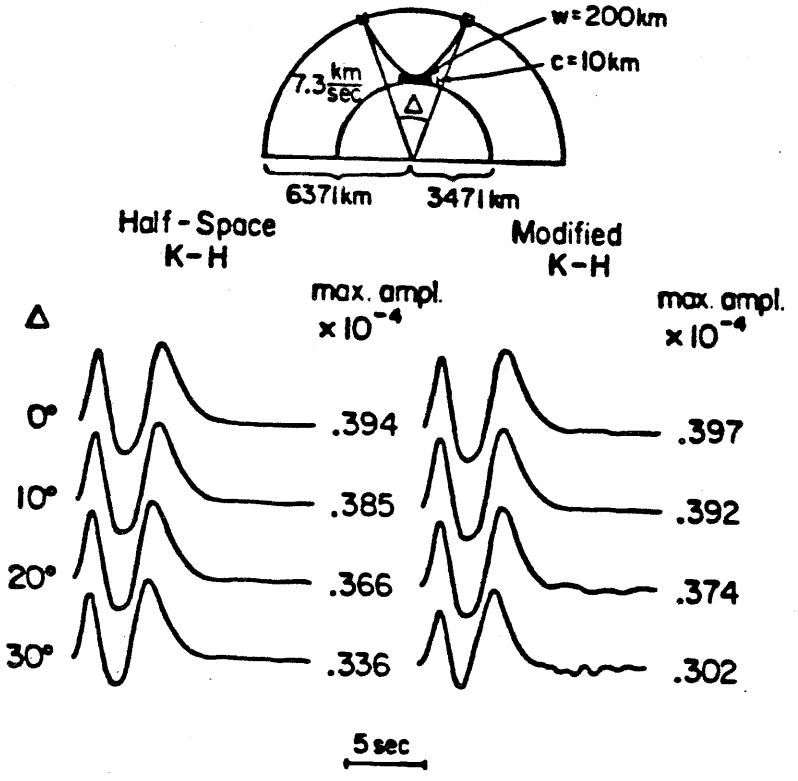

Figure 3.8. Synthetics computed with isovelocity K-H and modified K-H code for reflections off a plateau on the CMB 200 kilometers wide and 10 kilometers high. Reflections travel through a constant velocity medium of 7.3 km/sec. Source-receiver radius is 6371 kilometers and CMB radius is 3471 kilometers.

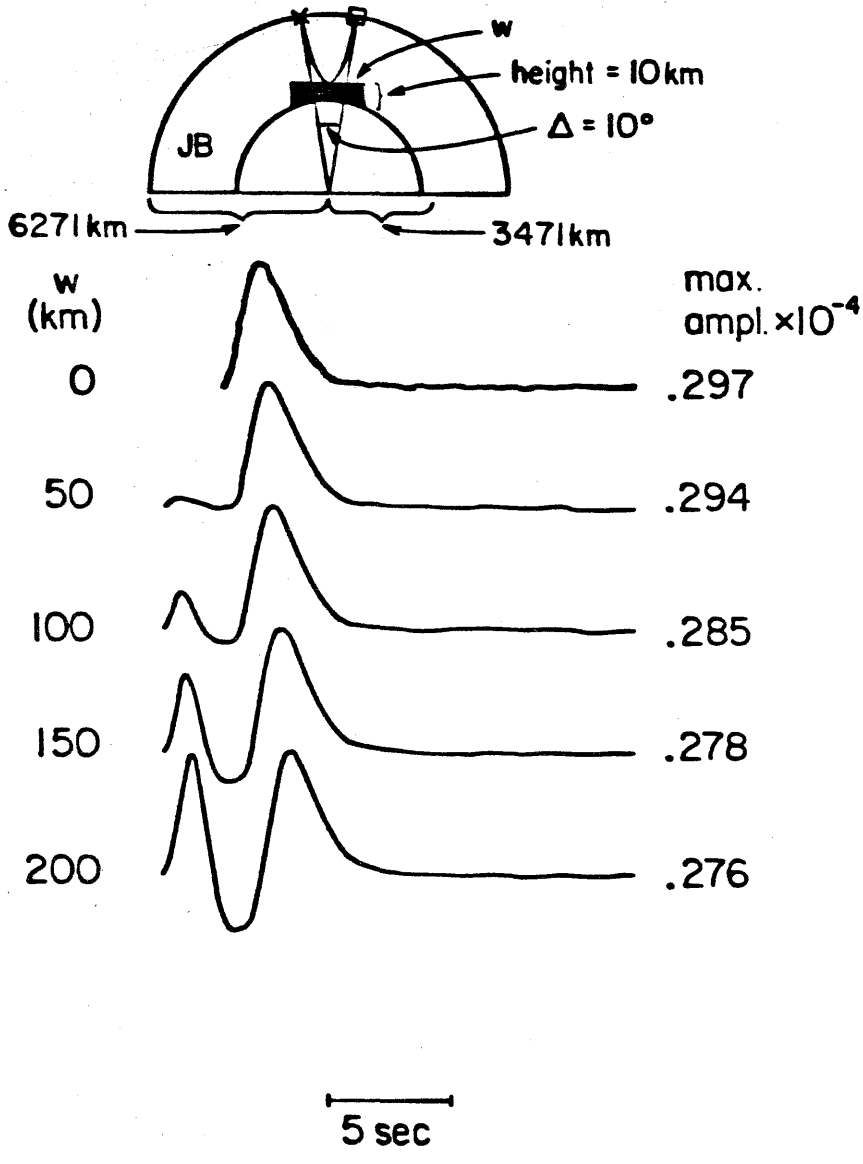

Figure 3.9. Reflections off a plateau 10 kilometers high and 0 to 200 kilometers wide, propagated through a JB Earth. Source and receiver are separated by 10° and are at a radius of 6271 kilometers. CMB radius is 3471 kilometers.

significant amplitude changes. In Figure 3.10 the shape constant is held constant but the angular separation of the source and receiver varies from 0° to 50°. The center of the topography is always at the bounce point. The waveforms do not change much with Δ. The amplitude reduction results primarily from $\frac{1}{R}$ decay rather than defocusing. The travel time residuals decrease from -2.66 seconds at 0° to -1.6 seconds at 50°. Again the waveform degenerates at the larger values of Δ because of the lack of equidistant interpolation of the ray information. There is also a longer period truncation phase at 50°.

We also calculate reflections off a gentler relief described by the following formula:

$$z = \left[3471^2 - (x^2 + y^2)\right]^{\frac{1}{2}} \text{ if } (x^2 + y^2)^{\frac{1}{2}} > \frac{w}{2} \qquad (3.20)$$

and

$$z = z - (\frac{c}{2})\left[\cos(W) - 1\right] \text{ where } W = 2\pi(\frac{(x^2 + y^2)^{\frac{1}{2}} - \frac{w}{2}}{w})$$

Here c is 20 kilometers and, as a result, causes the reflection to arrive 5.48 seconds early. The width, w, varies from 100 to 500 kilometers. The synthetics are shown in Figure 3.11. Such a bump causes similar effects as the plateau. There is a width of this relief which cannot be detected by a 5 second pulse. There is also the development of a precursory reflection. A reflection off a bump of width 500 kilometers has its peak amplitude reduced by a $\frac{1}{3}$

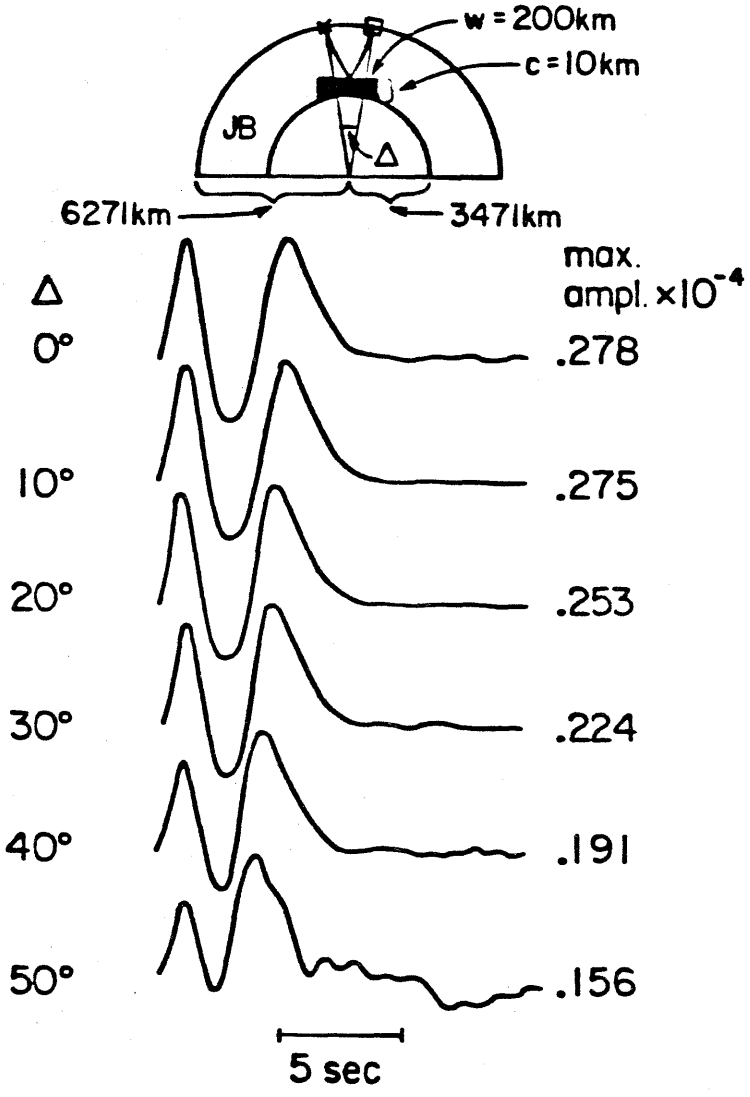

Figure 3.10. Reflections off a plateau 10 kilometers high and 200 kilometers wide, propagated through a JB Earth. The source-receiver separation varies from 0° to 50° and the radius is 6271 kilometers. CMB radius is 3471 kilometers.

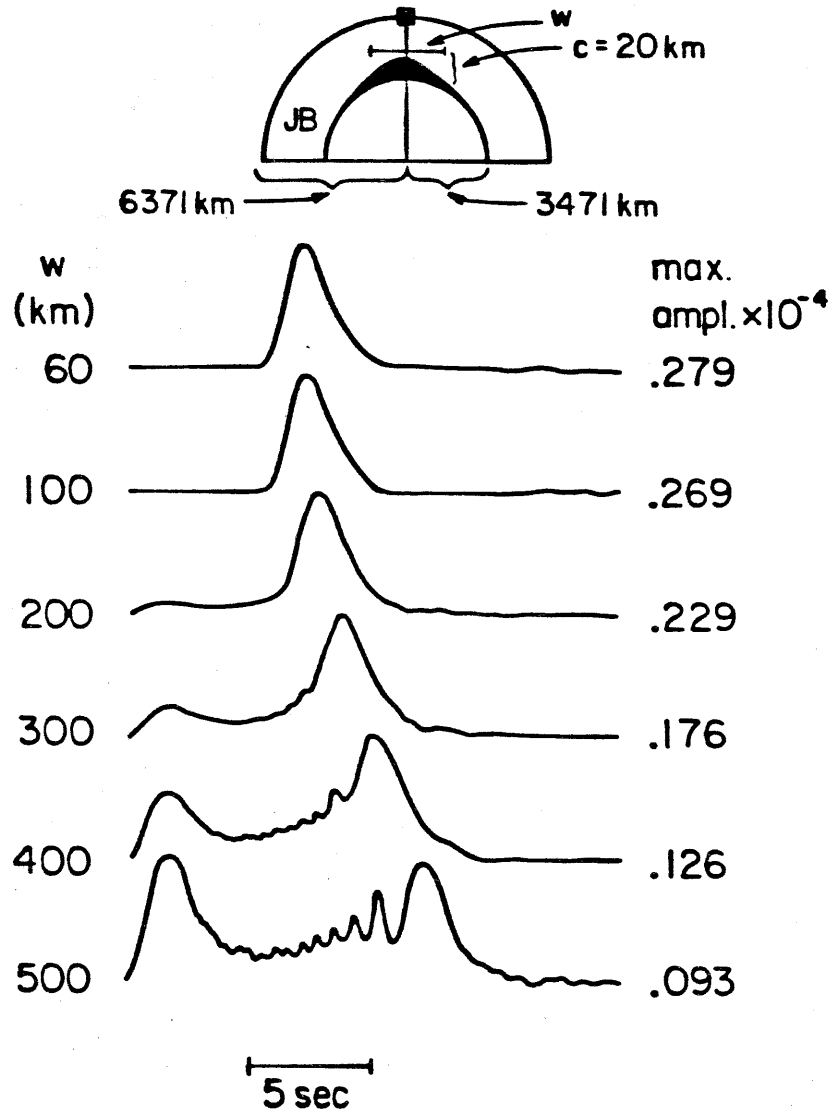

Figure 3.11. Reflections off a gentle bump 20 kilometers high and variable width, propagated through a JB Earth. The source and receiver are coincident at a radius of 6371 kilometers. CMB radius is 3471 kilometers.

Unfortunately noise contaminates this same synthetic due to interpolation problems in the integrand.

These examples of the modified K-H solutions yield promising results but also highlight some noise problems. This noise stems from an insufficiently smooth interpolation of the ray information on the surface. This is correctable. Synthetics from isovelocity models in Figure 3.8 and JB models in Figure 3.10 demonstrate that the half-space solutions give similar relative amplitude and travel time anomalies as the gradient solution for SH waves reflecting off a bumpy CMB. Thus, from here on, we will use the half-space technique to model the effect of shape on ScS waves with good assurance that significant propagational effects are not being neglected.

Modeling CMB topography with the half-space Kirchhoff-Helmholtz method

What size of CMB topography is compatible with the ScS data set? This phase has amplitude and travel time anomalies and precursors. Mitchell and Helmberger (1973), Lay (1983), and Lay and Helmberger (1983a) report anomalous long period ScS/S ratios which cannot be predicted with a smooth JB earth model at North American stations for Argentine and Sea of Okhotsk events. Both data sets are approximately SH polarized. Lay's data are shown in Figure 3.12 as a function of delta and azimuth. These ratios scatter from .8 to .1 and appear to be a function of delta and azimuth. Short period ratios scatter by the same magnitude but do not obviously correlate with the long period patterns. It is not clear whether the anomalous ratios are caused by heterogeneities along the path of S or ScS. Mitchell and

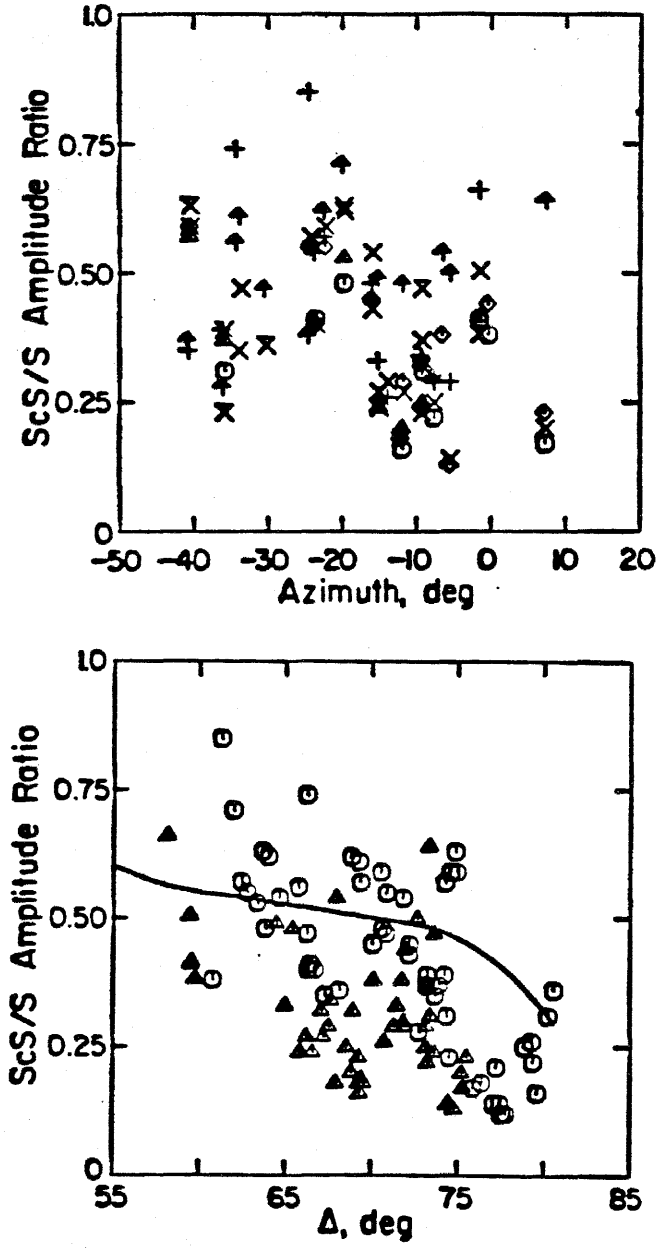

Figure 3.12. Observed long period peak-to-peak ScSH/SH amplitudes for Argentine events recorded in North America as a function of delta and azimuth. Patterns are corrected for radiation pattern only. Solid lines are ratios predicted for JB values (from Lay and Helmberger, 1983a).

Helmberger (1973) place the heterogeneity along the SHcSH path but Lay places it along the S path. We explore here the proposition that the anomalous behavior occurs along the ScS path.

There is a further ambiguity as to where the heterogeneity lies along the ScS path. Mitchell and Helmberger (1973) interpret the anomalous ratios as a result of a 60 kilometer thick high velocity gradient at the base of the mantle. This gradient causes SHcSH to bottom in the transition zone in D'' rather than reflect off the CMB. Long and short period SHcSH waves have precursors which support the view that D'' has unusual structure (Lay and Helmberger, 1983b). These precursors are observed at Δ between 70° and 80° for specific source-receiver geometries. Examples of this phase in the short and long period band are shown in Figure 3.13, from Lay and Helmberger (1983b). An alternative explanation for the anomalous ratios and precursors is that SHcSH reflects off an undulating CMB which causes focusing and/or defocusing and multiple arrivals.

The proposed relief on the CMB should produce the travel time residuals of ScS-S. These residuals are not contaminated by crustal and upper mantle structure and originate from the S and/or ScS paths. Again we assume that these anomalies arise from ScS interacting with a bumpy CMB. Figure 3.14 shows examples of ScS-S residuals as a function of azimuth and delta from Lay (1983). The maximum scatter of the residuals is approximately 6 seconds. The mean value of the residuals scatter by 2 and 4 seconds as a function of delta and azimuth, respectively.

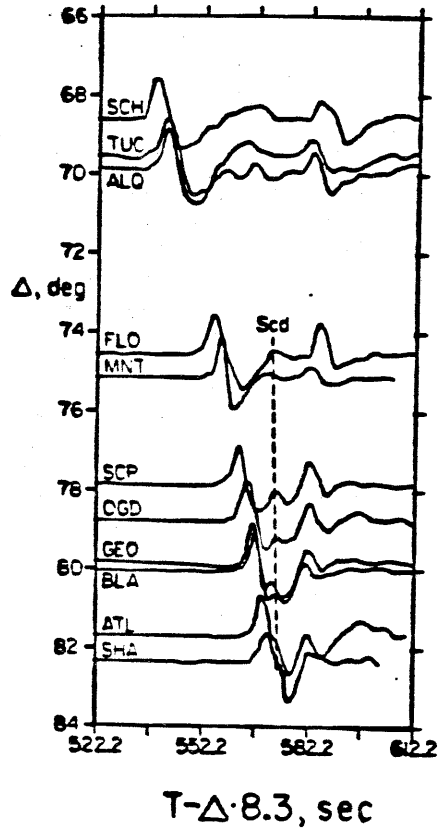

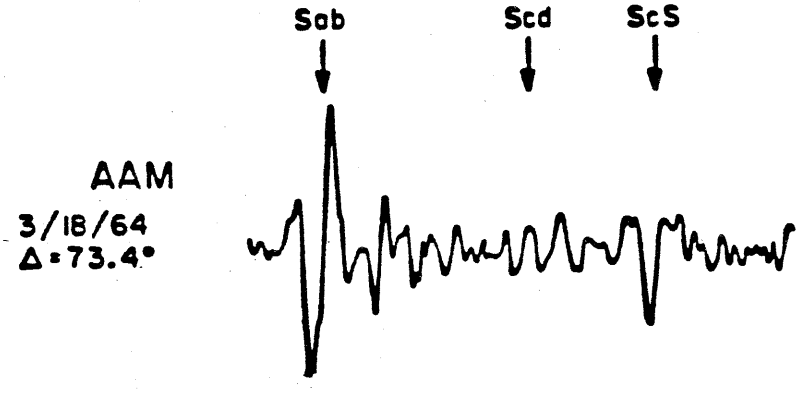

Figure 3.13. a) Observed profile of long period SH seismograms for a Sea of Okhotsk event recorded at North American stations. b) a typical short period record from this area (from Lay and Helmberger, 1983b).

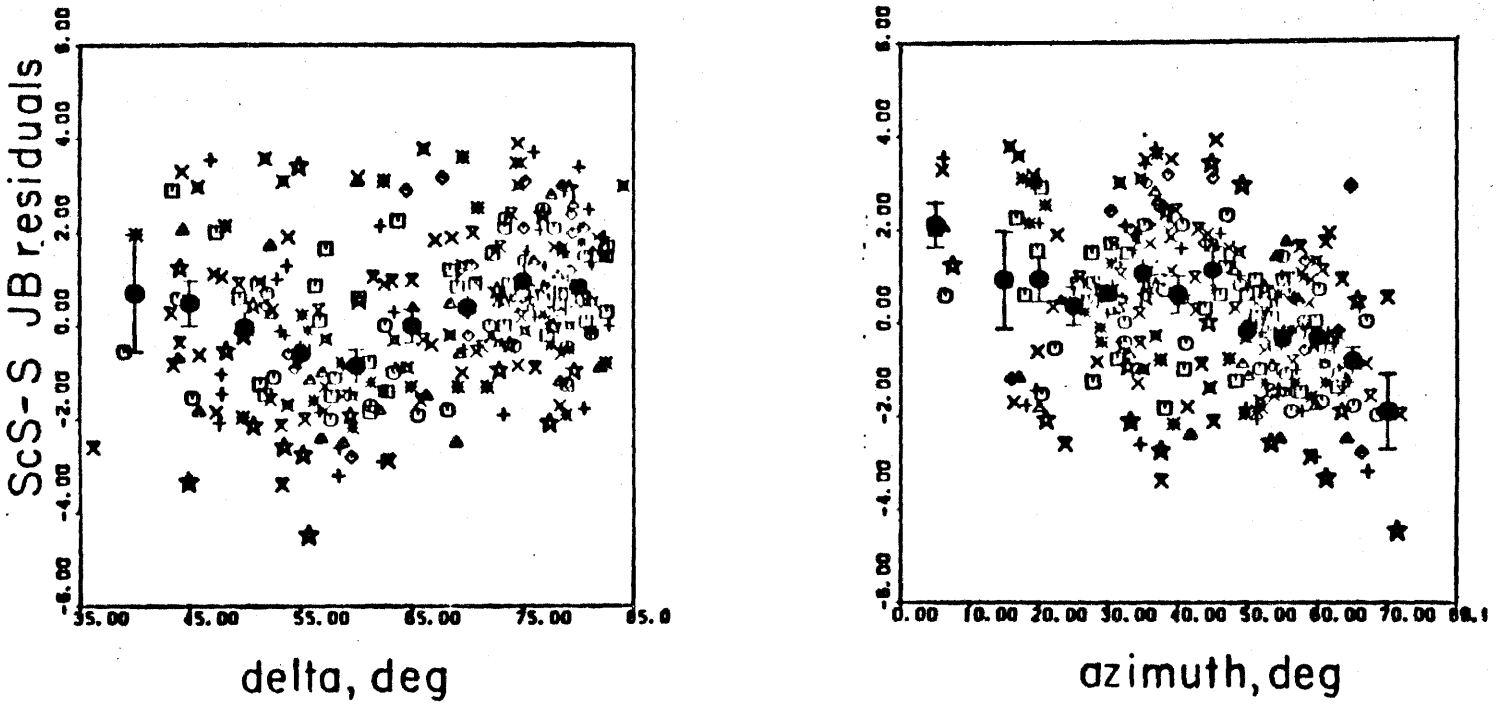

Figure 3.14. Plots of ScS-S residuals at North American stations from Sea of Okhotsk events as a function of delta and azimuth. Mean and standard deviations are also shown. (from Lay and Helmberger, 1983)

We assume that the residuals are caused by a bump described by equation (3.20). The choice is arbitrary; however, this gentle shape is more physically reasonable than an abrupt plateau. Figure 3.15 displays reflections at several distances from upwarps with heights of 10 kilometers and widths from 100 to 700 kilometers. No instrument is included. The center of the bump is always at the bounce point of the reflections. The travel time residuals range from -2.7 seconds at 0° to 2 seconds at 40°.

This figure has two important features. First, an upwarp with a width of 100 kilometers creates no amplitude or travel time anomalies in the synthetics. The Kirchhoff-Helmholtz code predicts some energy arrives early because of the upwarp. However, this energy is significantly lower in amplitude than the later pulse. Thus, the synthetics have an apparent delay. This pulse arrives at the time of an ScS reflection off a spherical CMB. Clearly, this upwarp is too small laterally to cause the perturbation of the two-way travel time of many elements which comprise the CMB.

The two-way travel time of an increased number of elements are altered as the upwarp widens. More elements are illuminated and contribute to the initial portion of the reflection. The overall impact of these timing changes is the broadening of the pulse until it is made up of two arrivals. Simultaneously, the peak amplitude decreases. The pulse starts to lose its multiple arrival appearance when the width of the bump exceeds 400 kilometers. Enough elements contribute to the response at an early time so that the first pulse is larger than the second one. For upwarps 600 and 700 kilometers wide, the resulting reflection is simple and has a slight long period tail. Also,

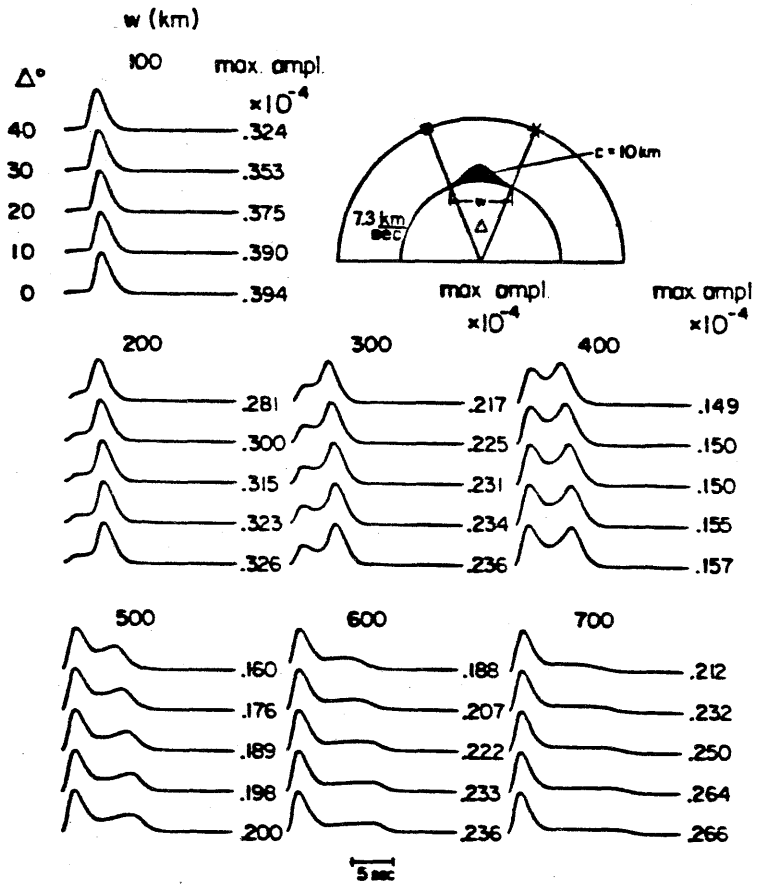

Figure 3.15. Reflections off a 10 kilometer high bump as a function of Δ and width. Peak amplitudes are adjacent to synthetics (isovelocity Kirchhoff model).

the peak amplitude increases. The upwarp is so wide that, in effect, it acts like a spherical surface. The trend of amplitudes indicates that reflections from a large enough width would have only a travel time anomaly and not a waveform anomaly.

The second feature is that the waveforms vary only slightly as a function of source-receiver separation. The maximum amplitude decreases with distance because of geometric spreading. Then we need only calculate the responses to a bump when the source and receiver are coincident. The impact of the topography at wider angles is easily extrapolated from synthetics at this source-receiver position.

To better assess the relative effect of CMB relief on the observable bands, we calculate long and short period synthetics for reflections from a wide variety of bump sizes, shown in Figures 3.16 and 3.17. In all cases, the source and receiver are coincident. The range of heights is designed to reproduce the range of scatter of ScS-S residuals. These upwarps produce negative residuals whereas the observed ScS-S residuals are both positive and negative. However, a simple model is sufficient because we are interested in length and height scales rather than precise shapes. These synthetics are distorted in the same way as the synthetics in Figure 3.15. There is always an upwarp with a width below which long and short period synthetics reflections cannot detect. As the upwarp widens, a precursor develops and is especially obvious in the short period band. At widths of 300, 400, 500, and 600 kilometers, there are two arrivals of equal magnitude and the peak amplitude is at a minimum. Then, as the bump widens further, the peak

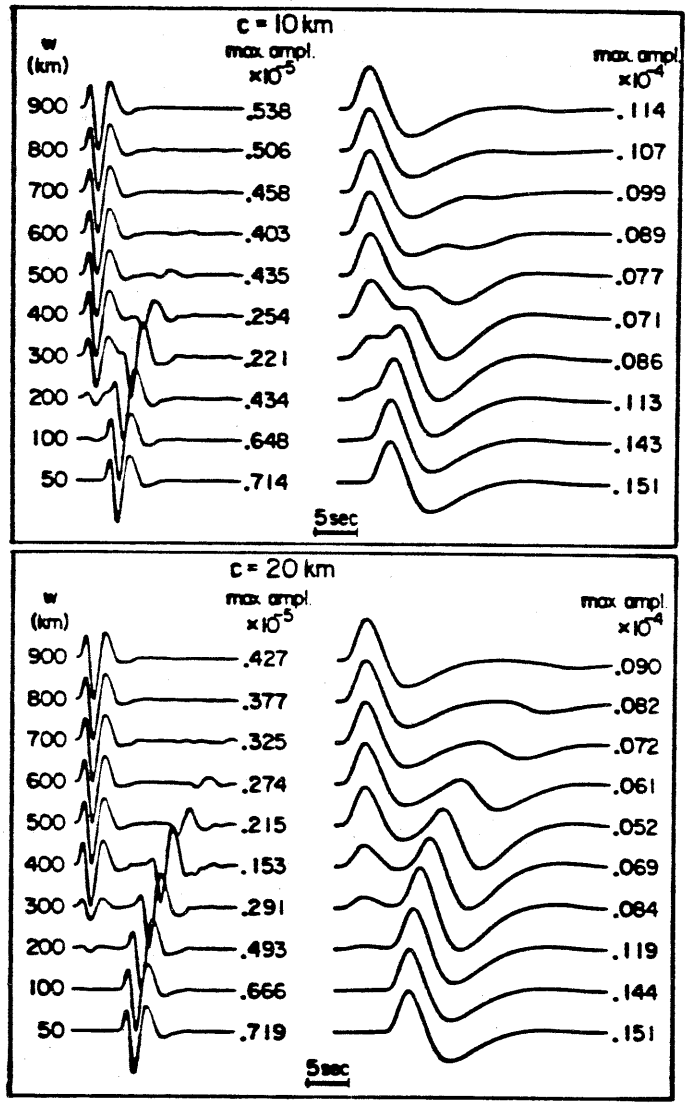

Figure 3.16. Short and long period reflections from relief with height 10 to 20 kilometers and widths 50 to 900 kilometers (isovelocity Kirchhoff model).

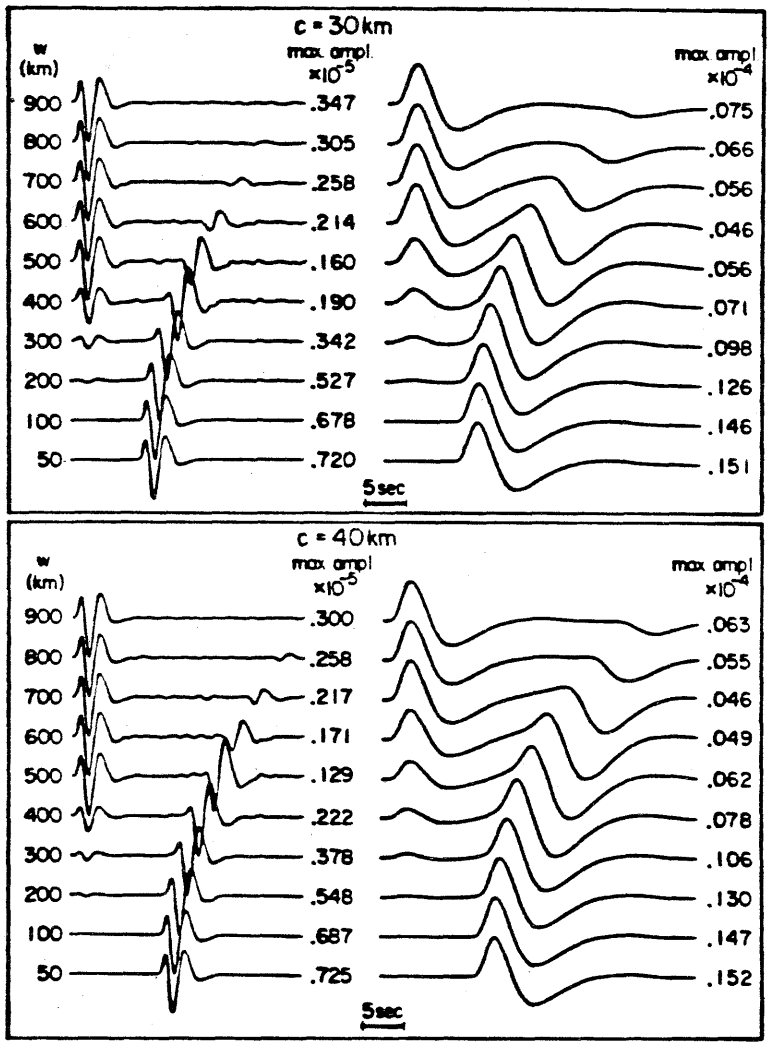

Figure 3.17. Short and long period reflections from relief with height 30 to 40 kilometers and width 50 to 900 kilometers (isovelocity Kirchhoff model)..

amplitude increases until the synthetics have only travel time anomalies. The ratios of the peak amplitudes of these synthetics divided by peak amplitudes of reflections from a spherical CMB in Figure 3.18 suggest that the topography impacts both frequency bands similarly. The long period synthetics is only slightly less depleted in energy than the short period synthetics.

These experiments show that upwarps with widths less than 100 or 200 kilometers fail to cause either a travel time or amplitude anomaly in SHcSH reflections in the long and short period band. Upwarps with widths exceeding 600 or 700 kilometers do not cause any obvious waveform distortion in these synthetics. The trend of the amplitude ratios suggests that a broad enough bump on the CMB will cause no amplitude defocusing. Furthermore, the peak amplitude of the ScS reflections can be reduced to .2 of the peak amplitude predicted for a reflection off a spherical CMB. Thus, if the predicted JB ratio of ScS/S is approximately .5 at teleseismic distances, then we can reduce it to .13 with a bump 40 kilometers high and 500 kilometers wide by defocusing. This number is almost the lowest ratio observed by Lay and Helmberger (1983a,b).

The modeling also predicts precursors to ScS reflections, a phenomenon observed by Lay and Helmberger (1983a,b). If we interpret the observations as a result from an upwarp on the CMB, then we must conclude from Figures 3.16 and 3.17 that the height of the bump is at least 20 kilometers and the width of the bump ranges from 300 to 500 kilometers. Such upwarps produce a precursor which is less than half the size of ScS and which arrives 10 to 15 seconds before ScS; these characteristics roughly match those of the

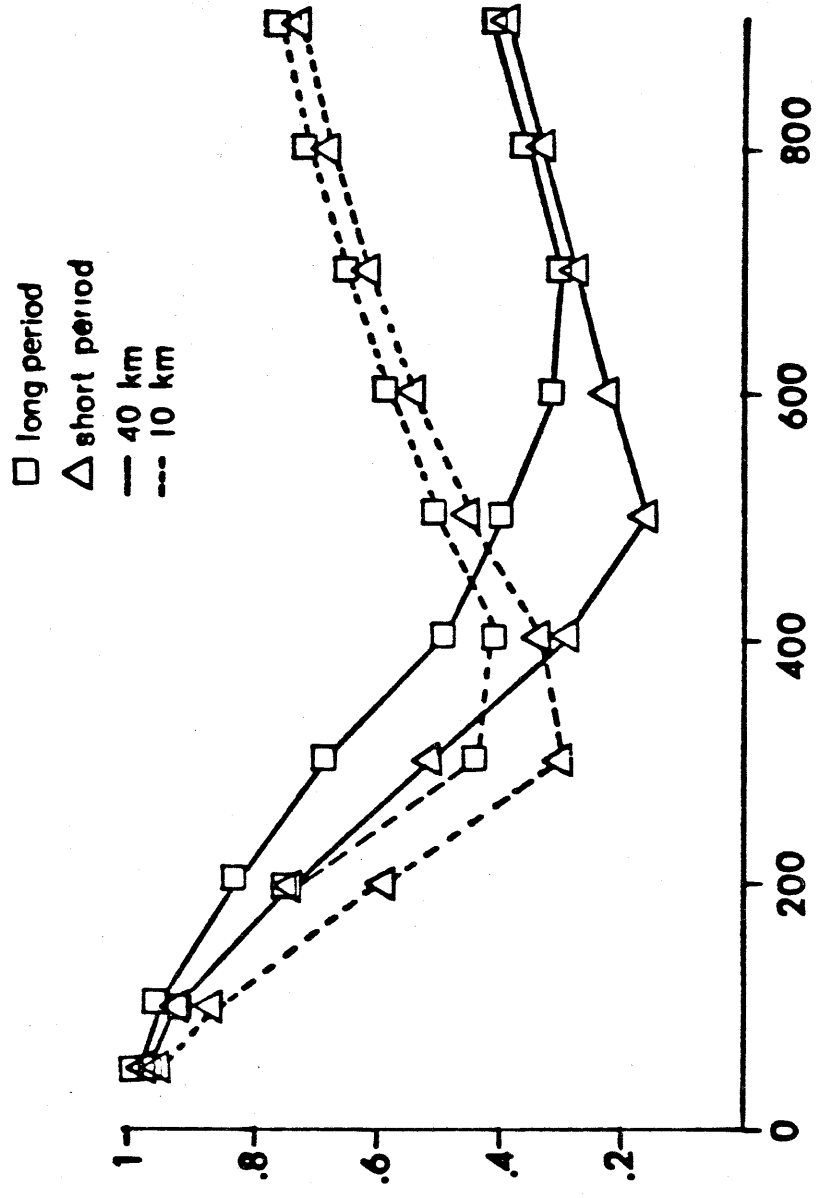

Figure 3.18. Ratios of peak amplitudes of reflections from bumps divided by reflections from a spherical CMB for long and short period bands and two heights, plotted as a function of width.

observed precursors. We caution, though, that the synthetics are for a coincident source-receiver while the actual precursors are observed for Δ between 65° and 75°.

Certainly, we must examine the CMB relief question in light of the variations of anomalies as a function of delta and azimuth. Any systematic changes provide a powerful constraint for the lateral extent of the topography. Unfortunately the systematics of these anomalies are difficult to glean from the data as Figures 3.12 and 3.14 show. If the timing scatter in Figure 3.14 is explained by CMB topography, the resultant relief will not cause any changes in the reflection amplitudes. We can only match the gradual changes of residual or amplitude ratio with delta or azimuth with these large scale bumps. Thus we must model how anomalies caused by CMB topography persist in azimuth or delta. For this preliminary study, we assume the anomalies to be a function of delta. We cannot model the effects of relief in the Δ range of interest because of the contamination by truncation phases. However, the results from the narrower range of angles may be relevant for the interpretation of the anomalies of ScS/S in the range of 55° to 85°.

The bump is positioned on the surface so that at 30° it is at the bounce point of the reflection. The choice of heights and widths of the bump is designed to maximize the waveform and amplitude distortion. The resultant synthetics are shown in Figure 3.19 and 3.20. Notably, precursors appear and disappear as a function of Δ, a result of the finite extent of the relief on the CMB. This feature may be present in profiles of ScS. For instance, we see a distinct precursor to ScS at ALQ which disappears at FLO in Figure

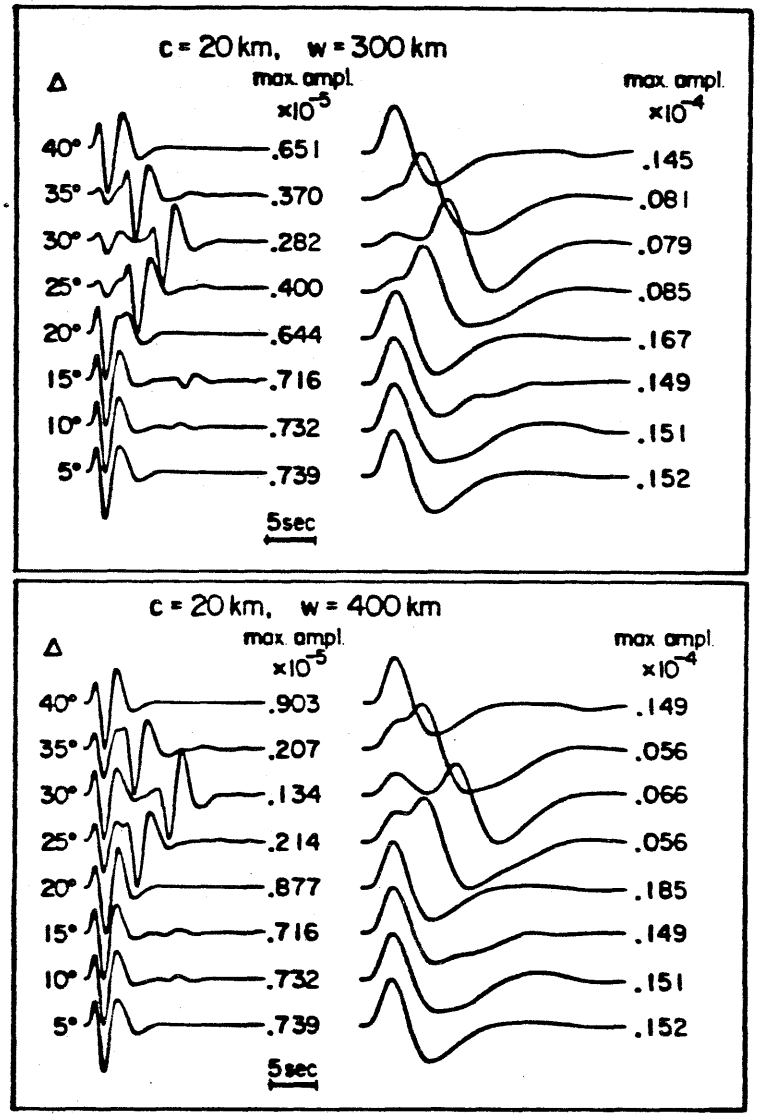

Figure 3.19. Long and short period reflections off an upwarp of height 20 kilometers and widths 300 and 400 kilometers as a function of Δ (isovelocity Kirchhoff model).

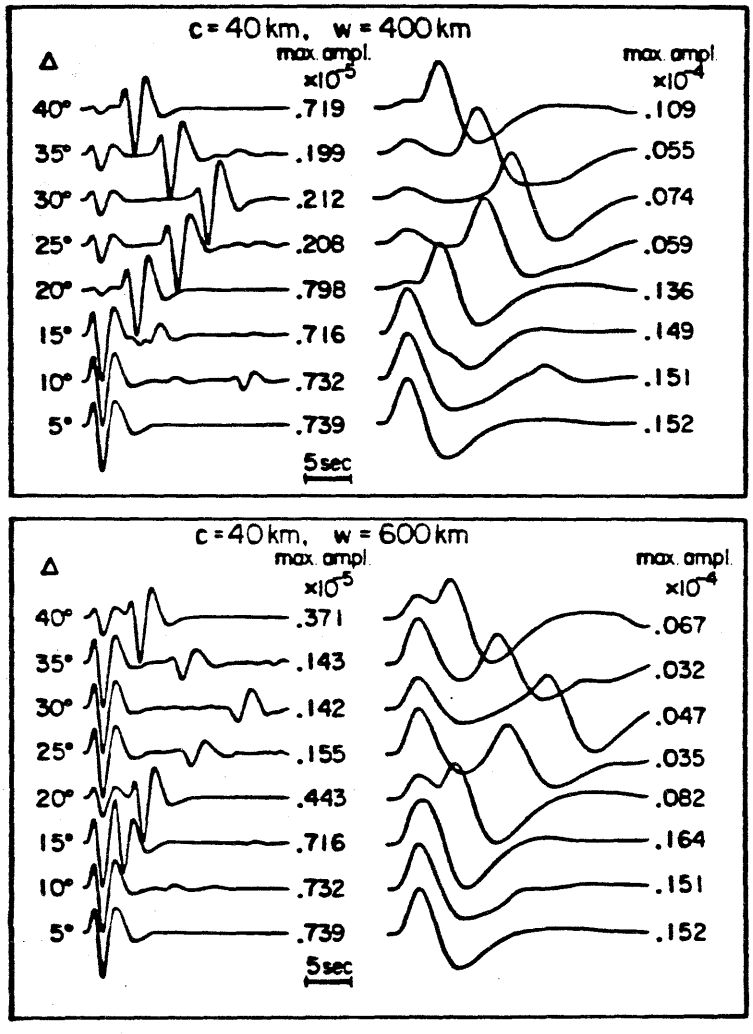

Figure 3.20. Long and short period reflections off an upwarp of height 40 kilometers and widths of 400 and 600 kilometers as a function of delta (isovelocity Kirchhoff model).

3.13. Associated with the appearance of the precursor is the occurrence of the amplitude minimum, seen in Figure 3.21. This figure shows the ratios of the peak amplitudes of the reflections from a bump divided by the predicted peak amplitudes of a reflection from a sphere. All the graphs have a minimum which develops over a 20° range. This dip in the ratio curve resembles a similar plot of Mitchell and Helmberger (1973). We also note that reflections from a bump 40 kilometers high and 400 kilometers wide have a precursor which has the appropriate height and time separation from the main phase. Alternatively we can argue that reflections from bumps 600 kilometers wide and 40 kilometers high match the observations in that they appear to be ScS waves with a negative residual.

Conclusions and Discussion

We accomplish two goals in this study. First, we establish the feasibility of computer implementation of the Kirchhoff-Helmholtz solution for a medium with a radially symmetric velocity gradient. This method requires a new computational approach because we must trace two sets of rays for every point on the surface. There are problems with jitter in the synthetics because of an inadequate interpolation scheme. The current implementation traces rays and retains information at equal increments of $\Delta i°$. Unfortunately, equal increments of $\Delta i°$ do not correspond to equal increments of horizontal and vertical distance along the integration surface. There are areas which have a high density of rays and other areas which have a paucity of ray information. A remedy for this uneven distribution is the higher order

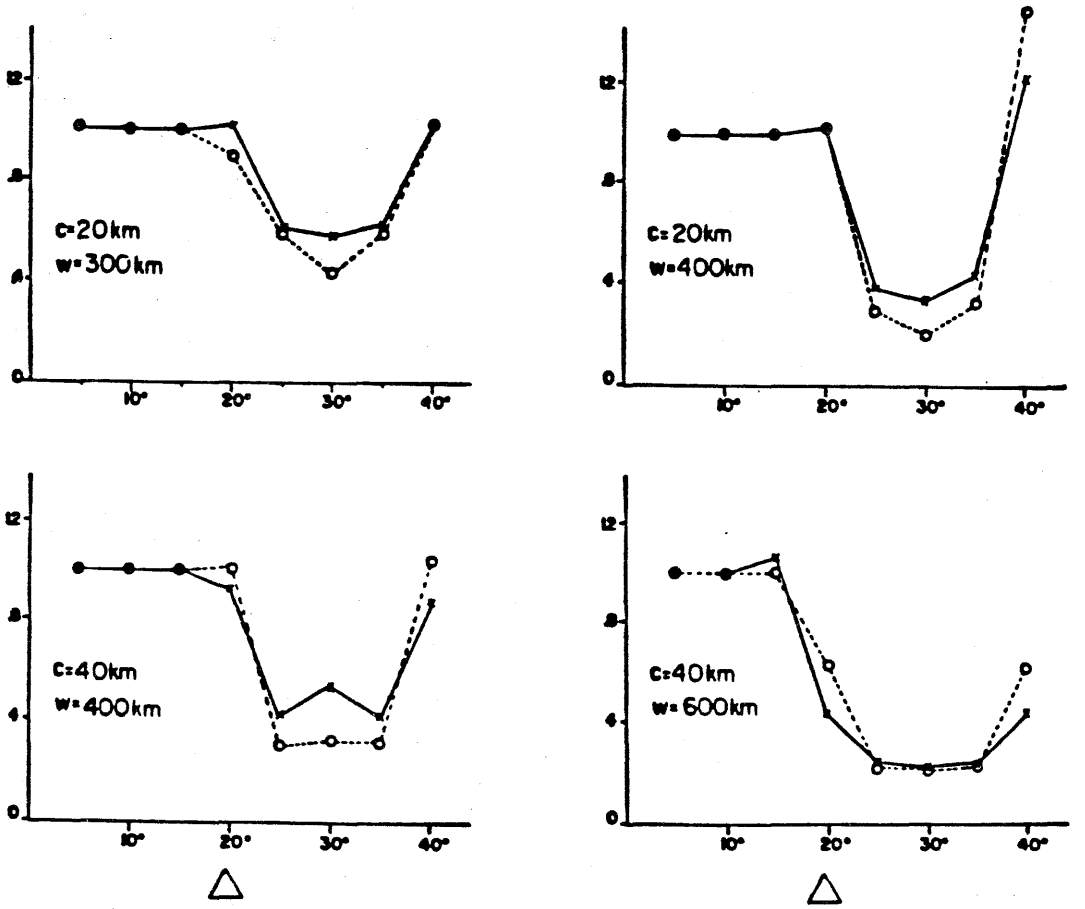

Figure 3.21. Ratios of peak amplitudes of reflections from bumps divided by reflections from a spherical CMB for long and short period bands as a function of Δ.

interpolation of the ray information. The amplitudes, travel times and ray parameters in Figure 3.3 are well-behaved and readily approximated by low order polynomials as a function of Δ and R. Only a few rays must be traced through coarse subshells to obtain enough synthetic data for interpolation. Furthermore, the interpolation has to be done only once for a given velocity model. The criterion for fitting would be either a least squares one or a min-max one rather than a Taylor series because we do not have the analytic first or second derivatives with respect to Δ or R of the ray information. Once one has interpolated the synthetic data, all the ray information can be described with only a few coefficients. Furthermore, one can calculate the ray information at each point with a formula rather than search through a large table. Finally, the smoothness of the synthetic seismogram will depend on the fineness of the surface discretization only.

With improvements the gradient technique enables us to model any high frequency precritical core phase which transmits or reflects through a bumpy CMB. It is a distinct alternative to scattering theory (Chernov, 1960; Bass and Fuks, 1979) currently used by seismologists. Scattering theory and Kirchhoff theory constitute, in a sense, two limiting cases. Both methods assume ordinary ray theory to calculate the amplitude and travel times of the incident wave before it interacts with the anomalous region. After this assumption, the similarity ends. The scattering method prescribes the statistical properties of the medium to infer the statistical properties of the wavefield, such as the mean square fluctuation of the amplitude and the phase. The deterministic material properties are not specified. However, the

mean value of the property, the mean square of the deviation, and the correlation function as a function of position are specified. If the property is random with a normal or Gaussian probability function, then these three functions are a complete statistical description of the medium (Bass and Fuks, 1979). Usually only the correlation function is specified in seismological scattering studies.

The spatial correlation function is a measure of how deviations of velocity and density from the mean values correlate from place to place. If the fluctuations of the velocity and density are random, the correlation coefficient should vanish at a large enough distance. The correlation coefficient with zero separation is the mean square fluctuation and is normalized to 1. The correlation function used by Chernov (1960) is either $e^{-\frac{|r|}{a}}$ or $e^{-\frac{r^2}{a^2}}$. The quantity a is called the correlation distance or radius and is a measure of the linear dimension of the longest irregularity. For distances beyond a , the correlation coefficient is zero. Scattering theory requires that $a <<< L$ where L is the length of the scattering volume or surface. In most discussions there is no stated assumption regarding a and the deformation wavelength. This model is statistical and does not allow for a deterministic variation of parameters. We cannot discover from these models how the average radius of the core or how the average S wave velocity in D" varies. In contrast, the Kirchhoff-Helmholtz method prescribes a deterministic property, the topography of the core-mantle boundary, to calculate the deterministic properties of the wavefield. With this method we cannot predict the effect of random fluctuations superimposed on the large scale

variations of the material properties because of the restrictions of the tangent plane approximations. A real surface can have both kinds of variations and waves can be affected by both of them.

There is another obvious difference between the two approaches. The seismological scattering studies assume that the deviations of material properties occur in a three dimensional volume with symmetry in one direction. However, the Kirchhoff-Helmholtz studies assume surface deviations. This difference makes the results of the two methods, a correlation distance and a topographic profile, difficult to compare. Detailed discussions of the similarity between the two quantities is unjustified.

The final difference is significant. The random scattering solutions (Aki and Richards, 1980) presume 1) the deviations of material properties $\delta\rho$ and $\delta\alpha$, are small compared to the mean value of these properties ρ and α and 2) the solution consists of two parts U and u where U is the solution to the unperturbed medium and u is the scattered wavefield. u is much smaller than U. If these conditions are met, u obeys a wave equation.

$$\frac{1}{\alpha_0^2}\frac{\partial^2 u}{\partial t^2} - \nabla^2 u = 4\pi Q \qquad (3.21)$$

Here Q is a body force-like term containing the relationship between $\delta\rho$, $\delta\alpha$ and U. We can write the solution to the above equation as an integral over the volume of the scatterer and it will bear a strong resemblance to the K-H solutions. However, it is only correct if u is small. Moreover, Q is not a true source term but a first-order perturbation result. To solve the integral equation involving Q, workers assume that the primary wave is a plane wave or a

spherical wave and evaluate the integral. This solution is the Born approximation (Morse and Feshbach, 1953) but it is occasionally and erroneously called the Kirchhoff solution; thus, one might incorrectly deduce that the Kirchhoff solution is appropriate for long wavelength incident waves and small perturbations. We stress that the Kirchhoff solution is valid when the radii of curvature of surface deviations are large relative to the incident wavelength. In addition, the perturbation solution is valid for all angles of incidence if the incident wave is a good approximation at these angles. Because of the tangent plane approximations assumed in the Kirchhoff-Helmholtz method, we cannot model the impact of topography on critical angle waves.

Despite this disadvantage, the preliminary K-H modeling predicts that important features of the ScS data set are compatible with upwarps with heights of 10 kilometers or more and widths of 300 to 600 kilometers. Are these scales too extreme to exist? Virtually all core phases have anomalies that are dependent on station-source geometries which can be interpreted in terms of CMB relief. However, the seismological community in the past (Cox and Cain, 1972) has concluded that deviations from the CMB can be no larger than 1 kilometer. For example, the strongest argument against significant topography is the existence of 1 Hertz PnKP and SnKS, $n \geq 2$ and ≤ 9. Bolt (1972) infers from statistics on PnKP a bound of 1 to 2 kilometers of relief. Other studies of these phases differ substantially from Bolt's. Chang and Cleary (1978,1981) and Doornbos (1980) use array analysis on 1 Hertz PKKP phases to infer the existence of precursors with unusual slownesses and

azimuths. Chang and Cleary also find that certain PKKP phases themselves have anomalous slownesses, azimuths, and amplitudes which the authors interpret as a focusing phenomenon from significant topography from the underside of the CMB. Doornbos estimates that a 7° dip on the boundary can account for these observations. Our cosine bumps have dips which vary from 1° to 7°.

Array analysis of precursors of PKP_1, PKP_2 and PKIKP (King et al., 1974; Doornbos and Husebye, 1972; Haddon and Cleary, 1974) also yield estimates of CMB topography. These precursors are 1 Hertz wavetrains with root mean square amplitudes which vary from .1 to .75 of the peak amplitude of the main phase. They are interpreted as scattered arrivals of PKP_1 and PKP_2 interacting with a random slightly heterogeneous region on or about the CMB ; their characteristics are used to deduce a and L. But these parameters have no clear quantitative relationship to the height or width of the upwarps. It is uncertain whether the features of these precursors are compatible with large scale gentle bumps. Other studies quantify deterministic features of PKP and PKIKP. Sacks et al. (1979) find that $\frac{PKP_1}{PKIKP}$ WWSSN short and long period amplitude ratios vary from .2 to 10 as a function of Δ. However, Clark and Pearce (1981) argue that these anomalies are largely a result of Sacks' failure to correct for radiation effects.

The amplitudes of long and short period P_{diff} and S_{diff} vary logarithmically as a function of Δ. In addition, the rate at which the amplitudes of these phases decay into the shadow scatters with station-source location (Ruff and Helmberger, 1982; Doornbos and Mondt, 1979a,b; Mondt, 1977;

Phinney and Cathles, 1969). Generally, unusual velocity and/or Q structure in D'' is invoked to explain these anomalies. Shimamura (1969) demonstrates that periodic irregularities on the CMB can cause anomalous decay amplitude spectra with small scale laboratory modeling. He argues that irregular structures with heights of 30 to 100 kilometers can account for some of the anomalous behavior of P_{diff}.

Long and short period PcP/P ratios scatter by an order of magnitude. (Muller et al., 1977; Lay, 1983; Chowdbury and Frasier, 1973). Occasionally this scatter can be attributed to source-station effects (Frasier and Chowdhury, 1974). Currently the consensus among workers is that long and short period PcP phases are impulsive with no obvious phase distortion despite the large amplitude variation. This observation argues for a sharp CMB boundary (Kanamori, 1967) but it does not argue against an undulating boundary. Notably, unlike ScS, PcP has no precursors. Whether bumps could produce precursors to PcP is a subject for future modeling studies.

The analysis of PcP travel times yields estimates of CMB relief. Bufe and Cardner (1972) use PcP and P times to infer 10 kilometers of relief. Engdahl and Johnson (1974) invert for P velocity structure and the CMB radius by minimizing PcP-P residuals. They interpret the remaining error after the inversion as CMB relief and obtain no more than 5 to 10 kilometers of relief. However, this estimate constitutes, in some sense, a lower bound because they are choosing the CMB radius which minimizes the sum of the square of these residuals. Another feature is that the absolute level of scatter of PcP-P residuals of 2 seconds (Buchbinder and Poupinet, 1973) is significantly less

than the overall scatter of ScS-S residuals. This difference cannot be explained by the difference in velocities alone, which suggests that the travel time anomalies arise from different paths.

We demonstrate from this data review that seismic evidence alone does not eliminate the possibility of large scale relief on the CMB. Thus, we must examine other lines of evidence to determine whether bumps of height of at least 10 kilometers and a width of several hundred kilometers are reasonable. To date the only other evidence which supports this kind of relief is a correlation between the Earth's gravitational and magnetic field (Hide and Horai, 1968; Hide, 1969). Heights of 8 kilometers over a lateral extent of several thousand kilometers are inferred. Even larger heights occur over shorter wavelengths. There is a mechanical basis for objecting to heights of this magnitude. The deviatoric stresses required to support these heights are large. Because shear waves do not propagate through the outer core, the rigidity and the strength of the outer core is low. It is unlikely, then, that these bumps can be supported statically. However, they could be supported dynamically. There is no current convection model which allows relief higher than 3 kilometers (Hager et al, 1984; Robinson, 1974). The existing mechanical reasoning points to bumps smaller than one required by the SHcSH data set. Smaller bumps are more compatible with the PcP data set. This suggests that possibly PcP waves see the topography of the CMB and that the anomalies in SHcSH/SH data are primarily a result of the S wave path rather than the ScS wave path.

REFERENCES

Aki, K. and P. G. Richards (1980), *Quantitative Seismology: Theory and Methods*, Vol. II, W. H. Freeman and Co., San Francisco.

Bass, F. and I. Fuks (1979), *Waves Scattering from Statistically Rough Surfaces*, Pergamon Press, New York.

Ben-Menahem, A. and S. Singh (1981), *Seismic Waves and Sources*, Springer-Verlag, New York.

Bolt, B. (1972), "Structure of the Earth's core from seismological evidence," EOS, Trans. Am. Geophys. Union, 53, 599.

Buchbinder, G. and G. Poupinet (1973), "Problems related to PcP and the core-mantle boundary illustrated by two nuclear events," Bull. Seism. Soc. Am., 63, 2047-2070.

Bufe, C. and D. S. Cardner (1972), "Nature of the core-mantle interface from surface-focus PcP observations," EOS, Trans. Am. Geophys. Union, 53, 600.

Bullen, K. E. (1965), *An Introduction to the theory of seismology*, Third Edition, Cambridge University Press, Cambridge.

Chang, A. and J. R. Cleary (1978), "Precursors to PKKP," Bull. Seism. Soc. Am., 68, 1059-1079.

Chang, A. and J. R. Cleary (1981), "Scattered PKKP: Further Evidence for scattering at a rough core-mantle boundary," Phys. Earth Planet. Interiors, 24, 15-29.

Chernov, L. A. (1960), *Wave Propagation in a Random Medium*, McGraw-Hill Book Co., New York.

Chowdbury, D. K. and C. W. Frasier (1973), "Observations of PcP and P phases at LASA at distances from 26° to 40°," J. Geophys. Res., 78, 6021-6027.

Clark, R. A. and R. G. Pearce (1981), Comments on "Lateral heterogeneity at the base of the mantle revealed by observations of amplitudes of PKP phases," by I. S. Sacks, J. A. Snoke, and L. Beach, Geophys. J. R. astr. Soc., 66, 741-750.

Cox, C. and J. Cain (1972), "International conference on the core-mantle interface," EOS, Trans. Am. Geophys. Union, 53, 591-597.

Doornbos, D. J. and E. S. Husebye (1972), "Array analysis of PKP phases and their precursors," Phys. Earth Planet. Interiors, 5, 387-399.

Doornbos, D. J. and J. C. Mondt (1979a), "Attenuation of P and S waves diffracted around the core," Geophys. J. R. astr. Soc., 57, 353-379.

Doornbos, D. J. and J. C. Mondt (1979b), "P and S waves diffracted around the core and the velocity structure at the base of the mantle," Geophys. J. R. astr. Soc., 57, 381-395.

Doornbos, D. J. (1980), "The effect of a rough core-mantle boundary on PKKP," Phys. Earth Planet. Interiors, 21, 351-358.

Engdahl, E. R. and L. E. Johnson (1974), "Differential PcP travel-times and the radius of the core," Geophys. J. R. astr. Soc., 39, 435-456.

Ewing, W., Jardetzky, W., and F. Press (1957), *Elastic Waves in Layered Media*, McGraw-Hill Book Co., New York.

Frasier, C. and D. Chowdbury (1974), "Effect of scattering on PcP/P amplitude ratios at LASA from 40° to 84°," J. Geophys. Res., 79, 5469-

5477.

Haddon, R. and J. Cleary (1974), "Evidence for scattering of seismic PKP waves near the mantle-core boundary," Phys. Earth Planet. Interiors, 8, 211-234.

Haddon, R. and P. Buchen (1981), "Use of the Kirchhoff's formula for body wave calculations," Geophys. J.R. astr. Soc., 67, 587-598.

Hager, B., Clayton, R., Richards, M., Comer, R., and A. Dziewonski (1984) "Lower mantle heterogeneity, dynamic topography, and the geoid," submitted to Nature.

Hales, A.L. and J. L. Roberts (1970b), "Shear velocity in the lower mantle and the radius of the core," Bull. Seism. Soc. Am., 60, 1427-1436.

Hide, R. and K. Horai (1968), "On the topography of the core-mantle interface," Phys. Earth Planet. Interiors, 1,305-308.

Hide, R. (1969), "Interaction between the Earth's liquid core and solid mantle." Nature, 222, 1055-1056.

Hide, R. and S. R. Malin (1970), "Novel correlations between global features of the Earth's gravitational and Magnetic Fields," Nature, 225, 605.

Jordan, T. H. and W. S. Lynn (1974), "A velocity anomaly in the lower mantle," J. Geophys. Res., 79, 2679-2685.

Kanamori, H. (1967), "Spectrum of P and PcP in relation to the mantle-core boundary and attenuation in the mantle," J. Geophys. Res., 72, 559-571.

King, D., Haddon, R. and J. Cleary (1974), "Array analysis of precursors to

PKIKP in the distance range 128° to 142°," Geophys. J. R. astr. Soc., 37, 157-173.

Lay, T. (1983), "Localized velocity anomalies in the lower mantle," Geophys. J. R. astr. Soc., 72, 483-516.

Lay, T. and D. V. Helmberger (1983a), "The shear-wave velocity gradient at the base of the mantle," J. Geophys. Res., 88, 8160-8170.

Lay, T. and D. V. Helmberger (1983b), "A lower mantle S-wave triplication and the shear velocity structure of D" ," Geophys. J. R. astr. Soc., 75, 799-837.

Mitchell, B. J. and D. V. Helmberger (1973), "Shear velocities at the base of the mantle from observations of S and ScS," J. Geophys. Res., 78, 6009-6020.

Mondt, J. C. (1977), "SH waves: theory and observations for epicentral distances greater than 90 degrees," Phys. Earth Planet. Interiors, 15, 46-59.

Morse, P. and H. Feshbach (1953), *Methods of Theoretical Physics*, Vol. 2, McGraw-Hill Book Co, New York.

Muller, G., Mula, A. H. and S. Gregersen (1977), "Amplitudes of long-period PcP and the core-mantle boundary," Phys. Earth Planet. Interiors, 14, 30-40.

Phinney, R. A. and L. M. Cathles (1969), "Diffraction of P by the core: a study of long-period amplitudes near the edge of the shadow," J. Geophys. Res., 74, 1556-1574.

Robinson, J. L. (1974), "A note on convection in the Earth's mantle," Earth

Planet. Sci. Letters, 21, 190-193.

Ruff, L. and D. V. Helmberger (1982), "The structure of the lowermost mantle determined by short-period P-waves amplitudes," Geophys. J. R. astr. Soc., 68, 95-119.

Sacks, I. S., Snoke, J. A. and L. Beach (1979), "Lateral heterogeneity at the base of the mantle revealed by observations of amplitudes of PKP phases," Geophys. J. R. astr. Soc., 59, 379-384.

Schloessin, H. H. (1974), "Corrugations on the core boundary interfaces due to constitutional supercooling and effects on motion in a predominantly stratified liquid core," Phys. Earth Planet. Interiors, 9, 147-156.

Shimamura, H. (1969), "Model study on core-mantle boundary structure," J. Phys. Earth, 17, 133-168.

Sinton, J. B. and L. N. Frazier (1982), "A method for the computation of finite frequency body wave synthetic seismograms in laterally varying media," Geophys. J. R. astr. Soc.,in press

Sobolev, S. (1930), "Sur l'équation d'onde pour un milieu hétérogène isotrope," Publ. Inst. Seism. Acad. Sci. U. R. S. S., 2

Stevenson, D. (1981), "Models of the Earth's core," Science, 214, 612.

Appendix

The Scalar Integral Representation for the Receiver off the Surface

This appendix consists of the derivation of the scalar integral representation and a derivation of the Kirchhoff-Helmholtz boundary conditions from the scalar integral equations. Although the former part of this appendix constitutes a review, the latter part may be original. Nowhere in the literature are there clear presentations of the scalar representation integral and its relationship to the Kirchhoff-Helmholtz boundary conditions.

From Officer (1958) we obtain the governing displacement equations of motion for small displacements and velocities in a linear elastic medium without body forces. They are

$$\rho \frac{\partial^2 u}{\partial t^2} = (\lambda + \mu) \frac{\partial \Delta}{\partial x} + \mu \nabla^2 u \tag{A1}$$

$$\rho \frac{\partial^2 v}{\partial t^2} = (\lambda + \mu) \frac{\partial \Delta}{\partial y} + \mu \nabla^2 v \tag{A2}$$

$$\rho \frac{\partial^2 w}{\partial t^2} = (\lambda + \mu) \frac{\partial \Delta}{\partial z} + \mu \nabla^2 w \tag{A3}$$

where u, v, and w are the Cartesian components of displacement. ρ is the density, λ is Lamé's constant and μ is the rigidity. Δ is the dilatation and is defined by the following equation:

$$\Delta = \frac{\partial u}{\partial x} + \frac{\partial v}{\partial y} + \frac{\partial w}{\partial z} \tag{A4}$$

Following Officer (1958) we simplify the system of equations (A1), (A2), and (A3) by letting $\mu = 0$, an assumption appropriate for gas or a liquid. The governing equations reduce to

$$\rho \frac{\partial^2 u}{\partial t^2} = \lambda \frac{\partial \Delta}{\partial x} \tag{A5}$$

$$\rho \frac{\partial^2 v}{\partial t^2} = \lambda \frac{\partial \Delta}{\partial y} \tag{A6}$$

$$\rho \frac{\partial w}{\partial t^2} = \lambda \frac{\partial \Delta}{\partial z} \quad . \tag{A7}$$

Furthermore, the stress-strain relationship reduces to

$$\sigma_{xx} = \sigma_{yy} = \sigma_{zz} = \kappa\Delta = -p \quad . \tag{A8}$$

where σ_{xx}, σ_{yy}, σ_{zz} are the normal stresses, κ is the bulk modulus and p is the hydrostatic pressure.

We solve the governing equations (A5), (A6) and (A7) by defining a velocity potential (Officer, 1958).

$$u = -\frac{1}{\rho} \frac{\partial \varphi}{\partial x} \tag{A9}$$

$$v = -\frac{1}{\rho} \frac{\partial \varphi}{\partial x} \tag{A10}$$

$$w = -\frac{1}{\rho} \frac{\partial \varphi}{\partial z} \tag{A11}$$

This potential obeys the wave equation

$$\nabla^2\varphi = \frac{\ddot{\varphi}}{\alpha^2} \tag{A12}$$

where $\alpha = (\frac{\lambda}{\rho})^{\frac{1}{2}}$. Solutions to equation (A11) are used to construct solutions to the displacement equation with the relationships (A9), (A10), and (A11). The relation between hydrostatic pressure and the potential, as a result of equations (A9), (A10), and (A11), is

$$p = \dot{\varphi} \, . \tag{A13}$$

We now derive the scalar integral representation for a potential which obeys the scalar wave equation (A12). A similar proof, for potentials obeying the Helmholtz equation, is in Mow and Pao (1971). Let us assume two such potentials φ_1 and φ_2 exist in volume V with wavespeed α. They are the result of two source potentials Φ_1 and Φ_2 in the volume. Thus,

$$\nabla^2\varphi_1 - \frac{1}{\alpha^2}\ddot{\varphi}_1 = \Phi_1 \tag{A14}$$

$$\nabla^2\varphi_2 - \frac{1}{\alpha^2}\ddot{\varphi}_2 = \Phi_2 \, . \tag{A15}$$

We define two vectors $\underline{r}$ and $\underline{r}_o$ within the volume. Figure A.1 displays the volume V and these two vectors. We manipulate (A14) and (A15) in the following way: a) multiply (A14) by φ_2 and multiply (A15) by φ_1 , b) subtract (A15) from equation (A14), c) integrate the resulting equation over all time and the volume with respect to coordinates $\underline{r}_o$ and t_o. We obtain, after these manipulations,

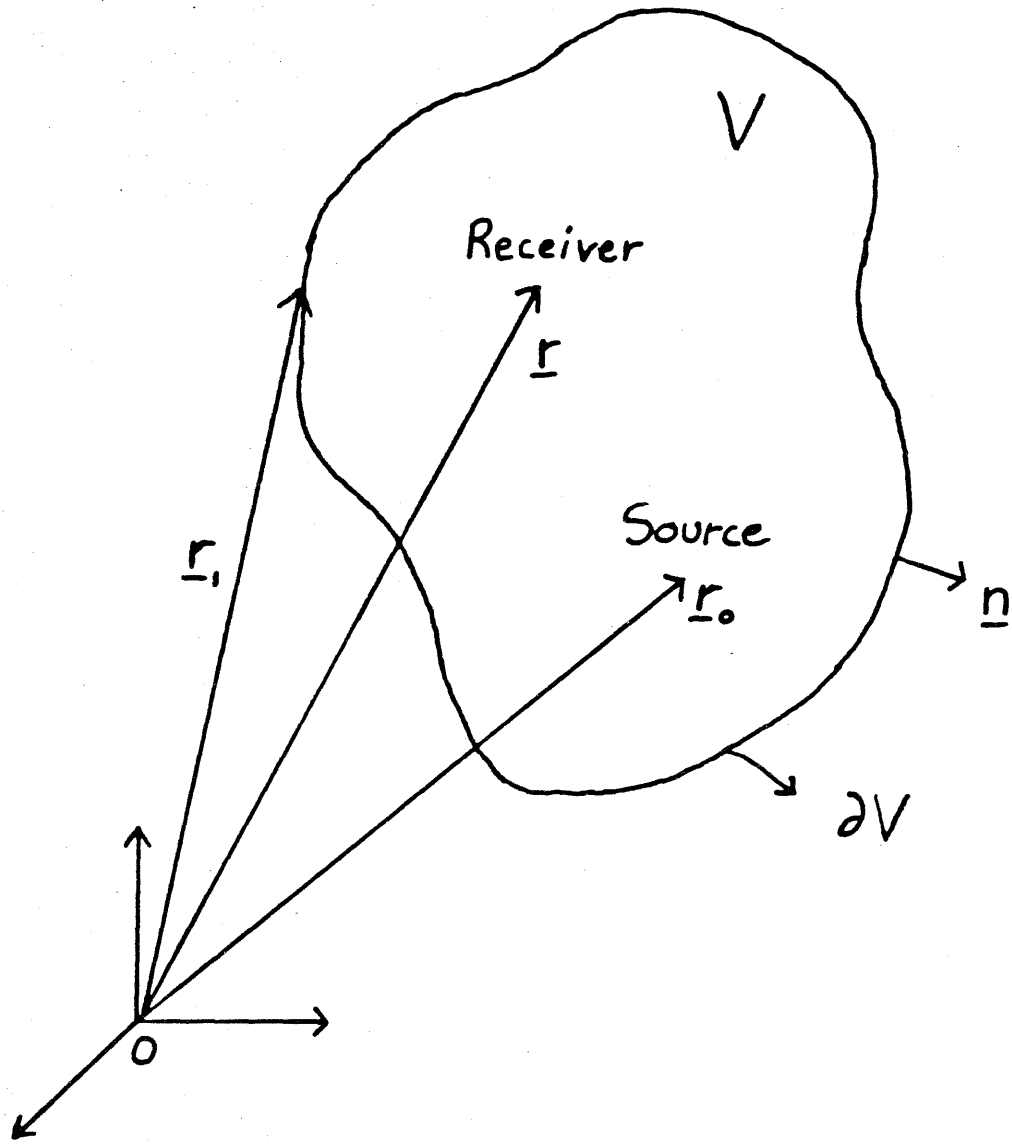

Figure A.1. The geometry for the scalar integral representation.

$$\int_0^{\infty} \int_V \{\varphi_2 \nabla^2 \varphi_1 - \varphi_1 \nabla^2 \varphi_2 - \frac{1}{\alpha^2} \varphi_2 \ddot{\varphi}_1 + \frac{1}{\alpha^2} \varphi_1 \ddot{\varphi}_2\} dV_o \, dt_o = \tag{A16}$$

$$\int_0^{\infty} \int_V \{\varphi_2 \Phi_1 - \varphi_1 \Phi_2\} dV_o \, dt_o \quad .$$

We simplify equation (A16) with use of the chain rule.

$$\frac{\partial}{\partial t} (\varphi_1 \dot{\varphi}_2 - \varphi_2 \dot{\varphi}_1) = \varphi_1 \ddot{\varphi}_2 - \varphi_2 \ddot{\varphi}_1 \tag{A17}$$

Thus

$$\frac{1}{\alpha^2} \int_0^{\infty} \int_v \{\varphi_1 \ddot{\varphi}_2 - \varphi_2 \ddot{\varphi}_1\} dV_o \, dt_o = \tag{A18}$$

$$\frac{1}{\alpha^2} \int_v \{\varphi_1 \dot{\varphi}_2 - \varphi_2 \dot{\varphi}_1\} \Big|_0^{\infty} dV_o \quad .$$

We prescribe the condition that $\underset{t \to \infty}{Lim} \varphi_1, \varphi_2 = O$ and $\underset{t \to \infty}{Lim} \dot{\varphi}_1, \dot{\varphi}_2 = 0$. The remaining integral (A16) reduces to

$$\int_0^{\infty} \int_V \{\varphi_2 \nabla^2 \varphi_1 - \varphi_1 \nabla^2 \varphi_2\} dV_o \, dt_o + \frac{1}{\alpha^2} \int_v \{\varphi_2 \dot{\varphi}_1 - \varphi_1 \dot{\varphi}_2\} \Big|_{t_o = 0} dV_o = \tag{A19}$$

$$\int_0^{\infty} \int_V \{\varphi_2 \Phi_1 - \varphi_1 \Phi_2\} dV_o \, dt_o \quad .$$

We now use Gauss' theorem to reduce the first term of the left-hand side from a volume integral to a surface integral.

$$\int_0^{\infty} \int_{\partial V} \{\varphi_2 \underline{\nabla} \varphi_1 - \varphi_1 \underline{\nabla} \varphi_2\} \cdot \underline{n} dS_o \, dt_o + \tag{A20}$$

$$\frac{1}{\alpha^2}\int_V \{\varphi_2\dot{\varphi}_1-\varphi_1\dot{\varphi}_2\}\Big|_{t_o=0} dV_o =$$

$$\int_o^\infty \int_V \{\varphi_2\Phi_1 - \varphi_1\Phi_2\} dV_o\, dt_o$$

Here $\underline{n}$ is the unit outward pointing normal of the surface ∂V (see Figure A.1).

We next define the potential φ_2 as the Green's function where $G(\underline{r},\underline{r}_o,t-t_o)$ is the fundamental singular solution of the scalar wave equation.

$$\nabla^2 G(\underline{r},\underline{r}_o,t-t_o) - \frac{1}{\alpha^2}\ddot{G}(\underline{r},\underline{r}_o,t-t_o) = \delta(\underline{r}-\underline{r}_o)\delta(t-t_o) \qquad \text{(A21)}$$

Thus we can identify the vectors $\underline{r}$ and $\underline{r}_o$ as the receiver and source coordinates, respectively. Substitution of the Green's function into (A20) yields

$$\int_o^\infty \int_{\partial V} \{G(\underline{r},\underline{r}_o,t-t_o)\underline{\nabla}\varphi(\underline{r}_o,t_o) - \varphi(\underline{r}_o,t_o)\underline{\nabla}G(\underline{r},\underline{r}_o,t-t_o)\}\cdot \underline{n}(\underline{r}_o)dS_o\, dt_o + \text{(A22)}$$

$$\frac{1}{\alpha^2}\int_V \{G(\underline{r},\underline{r}_o,t-t_o)\dot{\varphi}(\underline{r}_o,t_o) - \varphi\dot{G}(\underline{r},\underline{r}_o,t-t_o)\}\Big|_{t_o=0} dV_o =$$

$$\int_o^\infty \int_V G(\underline{r},\underline{r}_o,t-t_o)\Phi(\underline{r}_o,t_o) - \varphi_1(r_o,t_o)\delta(\underline{r}-\underline{r}_o)\delta(t-t_o)\}dV_o\, dt_o \quad .$$

We use the property of the delta function

$$\int_V h(\underline{x}')\delta(\underline{x}-\underline{x}')dV_{x'} = \begin{cases} h(\underline{x}) & , \underline{x}\in V \\ O & , \underline{x}\in V \end{cases} \qquad \text{(A23)}$$

to obtain the result, for $\underline{r}\in V$

$$\varphi(\underline{r},t) = \int_0^{\infty}\int_V G\Phi dV_o\,dt_o - \frac{1}{\alpha^2}\int_V \{G\dot{\varphi}-\varphi\dot{G}\}\Big|_{t_o=0} dV_o - \tag{A24}$$

$$\int_0^{\infty}\int_{\partial V} \{G\underline{\nabla}\varphi-\varphi\underline{\nabla}G\}\cdot\underline{n}dS_o\,dt_o \quad .$$

Now let $f(\underline{r},t)$ equal the sum of the first two terms on the right-hand side of (A24). In the absence of material boundaries, we obtain from (A24) that $\varphi(\underline{r},t) = f(\underline{r},t)$. Thus we can identify $f(\underline{r},t)$ as the whole-space solution with specified initial conditions. Thus, for $\underline{r} \in V$

$$\varphi(\underline{r},t) = f(\underline{r},t) - \int_0^{\infty}\int_{\partial V} \{G\underline{\nabla}\varphi-\varphi\underline{\nabla}G\}\cdot\underline{n}dS_o\,dt_o \quad . \tag{A25}$$

The second term is the reflected part of the solution. If $\underline{r} \notin V$, then the left side of (A24) is zero. If $\underline{r} \in \partial V$, then we obtain an integral equation which couples φ at $\underline{r}_1$, a station position on the surface ∂V, with all other values of φ and $\frac{\partial\varphi}{\partial n}$ on the surface. This integral equation contains a singularity when $\underline{r}_o = \underline{r}_1$; therefore, we must evaluate the integral as a limit as $\underline{r}_o \to \underline{r}_1$, a receiver position on the surface.

The Scalar Integral Representation for the Receiver on the Surface

There are several derivations of the limits of integral representations as the receiver point approaches the surface. Cole (1980) derives the limit for the elastodynamic integral representation. Banaugh (1962) derives the limit for the two dimensional Helmholtz representation. Mow and Pao (1971) discuss the limit for the three dimensional Helmholtz representation. For

completeness, we include a derivation of the limit of equation (A25) as the receiver approaches the surface.

We first specify a Green's function. For a linear homogeneous medium, it is sufficient to choose

$$G(\underline{r},\underline{r}_o,t-t_o) = \frac{-1}{4\pi\,|\underline{r}-\underline{r}_o|}\,\delta\left(t-t_o-\frac{|\underline{r}-\underline{r}_o|}{\alpha}\right) \quad . \tag{A26}$$

Let $\varphi(\underline{r}_1,t)$ be the potential on the surface. We want to evaluate the following equation:

$$\lim_{x\to x_1} \int_o^\infty \int_{\partial V} \{G\nabla\underline{\varphi}-\varphi\nabla\underline{G}\}\cdot\underline{n}\,dS_o\,dt_o \quad . \tag{A27}$$

This integral is singular at one point on the surface. Let us break up the integral into an integration over two surfaces, one which contains the singular point as the receiver approaches the surface, Σ, and one which does not, $\partial V-\Sigma$.

$$\int_o^\infty \int_{\partial V} \{G\nabla\underline{\varphi}-\varphi\nabla\underline{G}\}\cdot\underline{n}\,dS_o\,dt_o = \int_o^\infty \int_{\Sigma} \{G\nabla\underline{\varphi}-\varphi\nabla\underline{G}\}\cdot\underline{n}\,dS_o\,dt_o \tag{A28}$$

$$+ \int_o^\infty \int_{\partial V-\Sigma} \{G\nabla\underline{\varphi}-\varphi\nabla\underline{G}\}\cdot\underline{n}\,dS_o\,dt_o$$

We now evaluate the limit of the integral over Σ as the receiver approaches the surface Σ and as Σ shrinks to zero size. The second integral becomes a principal value. The first term of the integral containing the singular point is

$$\lim_{\delta\to o}\lim_{x\to x_1} \int_o^\infty \int_{\Sigma} G\frac{\partial\varphi}{\partial n}(\underline{r}_o,t_o)\,dS_o\,dt_o \quad . \tag{A29}$$

Here δ is the maximum chord of Σ. Substitution of (A26) into (A29) yields

$$\lim_{\delta \to 0} \lim_{x \to x_1} \int_{\Sigma} \frac{\partial \varphi}{\partial n} \frac{(\underline{r}_o, t - \frac{|\underline{r} - \underline{r}_o|}{\alpha})}{4\pi |\underline{r} - \underline{r}_o|} dS_o \quad . \tag{A30}$$

Following Cole (1980) and Kellogg (1953), we require that the functions φ and $\frac{\partial \varphi}{\partial n}$ satisfy the Holder condition in space and time; that is,

$$| \varphi(\underline{r}_o, t) - \varphi(\underline{r}, t) | \leq A \, |\underline{r} - \underline{r}_o|^n \text{ for } |\underline{r} - \underline{r}_o| < \delta \tag{A31}$$

$$| \varphi(\underline{r}, t_2) - \varphi(\underline{r}, t_1) | \leq B \, |t_2 - t_1|^\gamma \text{ for } |t_2 - t_1| < \frac{\delta}{\alpha} \quad .$$

We specify that $o < n \leq 1$ and $o < \gamma \leq 1$. Similar conditions hold for $\frac{\partial \varphi}{\partial n}$. Therefore,

$$[\frac{\partial \varphi}{\partial n}(\underline{r}_o, t)] = \frac{\partial \varphi}{\partial n}(\underline{r}_1, t) + A |\underline{r} - \underline{r}_o|^n + B |\underline{r} - \underline{r}_o|^\gamma \text{ for } |\underline{r} - \underline{r}_o| < \delta \tag{A32}$$

Here the brackets denote the retarded values of $\frac{\partial \varphi}{\partial n}$. We substitute (A32) into the integral (A30). We also allow $\underline{r}$ to approach the surface to the singular point $\underline{r}_1$. Thus we obtain

$$\lim_{\delta \to o} \left[\frac{\partial \varphi}{\partial n}(\underline{r}_1, t) \int_{\Sigma} \frac{dS_o}{|\underline{r}_1 - \underline{r}_o|} + A \int_{\Sigma} \frac{|\underline{r}_1 - \underline{r}_o|^n}{|\underline{r}_1 - \underline{r}_o|} dS_o + B \int \frac{|\underline{r}_1 - \underline{r}_o|^\gamma}{|\underline{r}_1 - \underline{r}_o|} dS_o \right] \tag{A33}$$

We now invoke a theorem from Kellogg (1953). This theorem states that the integral

$$\int\int \frac{dS}{R^\beta} \quad 0 < \beta < 2 \tag{A34}$$

where S is a regular region of the plane, is convergent, and, for all regions S of the same area, it is greatest when S is a circle about P.

We can choose the surface Σ, containing the singular point $\underline{r}_1$, to be small enough such that it can be described as a regular region of a plane which is tangent to the point $\underline{r}_1$. We also choose the region to be a circle. Thus, all three terms in (A33) converge. Let us evaluate the first and most singular term.

$$\lim_{\delta \to o} \frac{\partial \varphi}{\partial n}(\underline{r}_1,t) \int_0^{\delta} \int_0^{2\pi} \frac{R_o \, dR_o \, d\Theta_o}{R_o} = \lim_{\delta \to o} \left[\frac{\partial \varphi}{\partial n}(\underline{r}_1,t) 2\pi\delta \right] = O \qquad \text{(A35)}$$

If the most singular term vanishes, then the other two terms must also vanish. Thus, the integral (A29) gives no contribution to the singular integral in (A28).

We next evaluate the second term of the singular term.

$$\lim_{\delta \to o} \lim_{x \to x_1} \int_o^{\infty} \int_{\Sigma} \{\varphi \nabla \underline{G}\} \cdot \underline{n} \, dS_o \, dt_o \qquad \text{(A36)}$$

The gradient is comprised of two terms.

$$\nabla \underline{G} = \frac{-\dot{\delta}\left(t - t_o - \frac{|\underline{r} - \underline{r}_o|}{\alpha}\right)}{1\pi\alpha |\underline{r} - \underline{r}_o|} \nabla |\underline{r} - \underline{r}_o| + \qquad \text{(A37)}$$

$$\frac{\delta\left(t - t_o - \frac{|\underline{r} - \underline{r}_o|}{\alpha}\right)}{4\pi} \nabla \left(\frac{1}{|\underline{r} - \underline{r}_o|} \right)$$

where

$$\nabla|\underline{r}-\underline{r}_o| = \frac{\underline{r}-\underline{r}_o}{|\underline{r}-\underline{r}_o|} \tag{A38}$$

$$\nabla\left(\frac{1}{|\underline{r}-\underline{r}_o|}\right) = -\frac{\underline{r}-\underline{r}_o}{|\underline{r}-\underline{r}_o|^3} \quad .$$

Substitution of the gradient into equation (A36) yields

$$\lim_{\delta\to o}\lim_{x\to x_1}\int_\Sigma \frac{1}{4\pi}\left\{\frac{-\varphi(\underline{r}_o,t-\frac{|\underline{r}-\underline{r}_o|}{\alpha})}{\alpha|\underline{r}-\underline{r}_o|} - \frac{\varphi(\underline{r}_o,t-\frac{|\underline{r}-\underline{r}_o|}{\alpha})}{|\underline{r}-\underline{r}_o|^2}\right\}\cos\lambda dS_o \tag{A39}$$

where

$$\cos\lambda = \underline{n}\cdot\frac{(\underline{r}-\underline{r}_o)}{|\underline{r}-\underline{r}_o|} \quad .$$

If $\dot{\varphi}$ and φ obey the Holder condition, the term involving $\dot{\varphi}$ vanishes as we take the two ordered limits. The remaining term is

$$\lim_{\delta\to o}\lim_{x\to x_1}\left[\frac{\varphi(\underline{r}_1,t)}{4\pi}\int_\Sigma \frac{\cos\lambda dS_o}{|\underline{r}-\underline{r}_o|^2} + A\int_\Sigma \frac{|\underline{r}-\underline{r}_o|^\gamma}{|\underline{r}-\underline{r}_o|^2}\cos\lambda dS_o\right] \quad . \tag{A40}$$

From prior arguments, the second term vanishes. To evaluate the first term, we set up a local cylindrical coordinate system on the area surrounding the singular point and specify z to be parallel to $\underline{n}$ (see Figure A.2). Then $\underline{r}_o = (0,R_o,\theta)$ and $\underline{r} = (z,R,0)$. Then

$$|\underline{r}-\underline{r}_o|^2 = R^2 + R_o^2 - 2RR_o\cos\theta + z^2 \tag{A41}$$

and

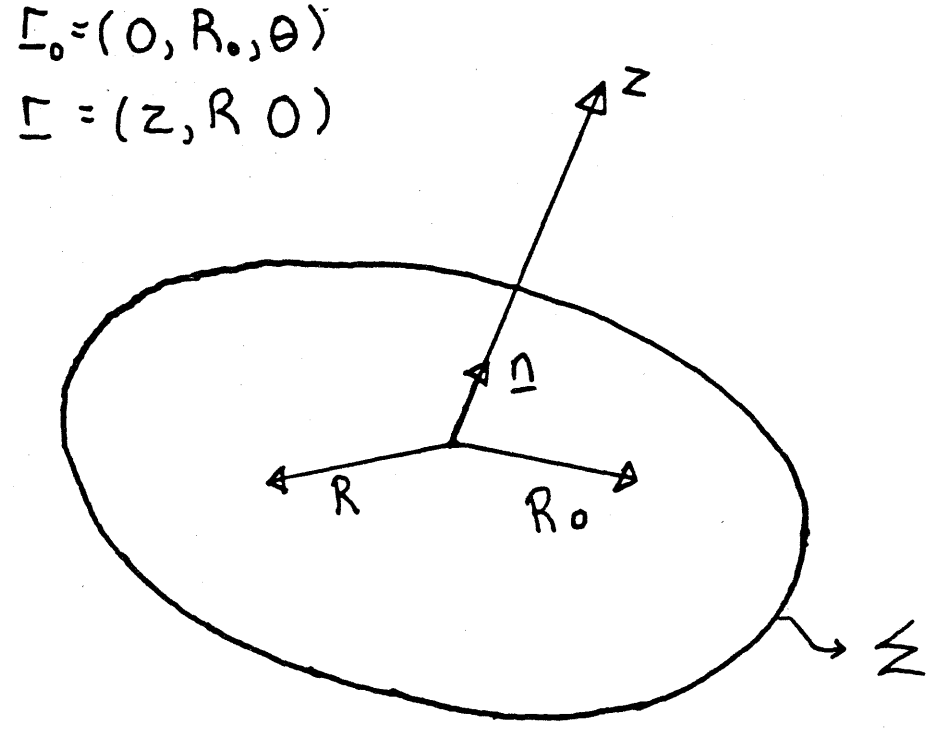

Figure A.2. The local cylindrical coordinate system centered on the singular point.

$$\cos\lambda = \frac{z}{\left[z^2 + R^2 + R_o^2 - 2RR_o\cos\theta\right]^{\frac{1}{2}}} \quad .$$

Without loss of generality we set $R = 0$; that is, the receiver point approaches the surface along the normal $\underline{n}$. Therefore,

$$\lim_{\delta\to 0}\lim_{x\to x_1}\frac{\varphi(\underline{r}_1,t)}{4\pi}\int_0^{\delta}\int_0^{2\pi}\frac{z}{(z^2 + R_o^2)^{\frac{3}{2}}}R_o\,dR_o \quad . \tag{A42}$$

To obtain the final result, we take the following ordered limit:

$$\tfrac{1}{2}\varphi(\underline{r}_1,t) = \lim_{\delta\to 0}\lim_{z\to 0}\frac{-z}{(z^2 + R_o^2)^{\frac{1}{2}}}\Bigg|_0^{\delta} \quad . \tag{A43}$$

Evaluating this ordered limit yields $\tfrac{1}{2}\varphi(\underline{r}_1,t)$.

The Derivation of the Kirchhoff-Helmholtz Boundary Conditions

We now derive the Kirchhoff-Helmholtz boundary values from the scalar integral representation. We specify two volumes V_1 and V_2 with velocities α_1 and α_2 and densities ρ_1 and ρ_2. The two volumes are welded together at a surface ∂V. The source is in V_1. Applying the representation theorem for a potential off the surface yields

$$\varphi_i(\underline{r},t) = \int_{\partial V}\{G_i * \nabla\underline{\varphi}_i - \varphi_i * \nabla\underline{G}_i\}\cdot\underline{n}_i\,dS_o + f_i(\underline{r},t) \tag{A44}$$

where i = 1 or 2 and

$$G_i = -\frac{1}{4\pi|\underline{r} - \underline{r}_o|}\delta\left(t - t_o - \frac{|\underline{r} - \underline{r}_o|}{\alpha_i}\right) \quad .$$

Furthermore $f_i(\underline{r},t) = 0$ when i = 2. On the surface ($\underline{r}_1 \in \partial V$) the potential is

$$\tfrac{1}{2}\varphi_i(\underline{r}_1,t) = \int_{\partial V}\{G_i * \nabla\varphi_i\}\cdot\underline{n}_i\,dS_o - P\int_{\partial V}\{\varphi_i * \nabla\underline{G}_i\}\cdot\underline{n}_i\,dS_o + f_i(\underline{r}_1,t) \quad . \quad \text{(A45)}$$

The following boundary conditions are specified on the interface : 1) continuity of particle velocity normal to the surface 2) continuity of pressure.

$$\frac{1}{\rho_1}\nabla\varphi_1\cdot\underline{n}_1 = -\frac{1}{\rho_2}\nabla\varphi_2\cdot\underline{n}_2 \qquad \text{(A46.a)}$$

$$\dot{\varphi}_1 = \dot{\varphi}_2 \qquad \text{(A46.b)}$$

The surface is described by a function $z(x,y)$. Then the normals and dS in cartesian coordinates are

$$\underline{n}_1 = \frac{(\frac{\partial z}{\partial x}\hat{i} + \frac{\partial z}{\partial y}\hat{j} - \hat{k})}{|\underline{n}_1|} \qquad \text{(A47.a)}$$

$$\underline{n}_2 = \frac{(-\frac{\partial z}{\partial x}\hat{i} - \frac{\partial z}{\partial y}\hat{j} + \hat{k})}{|\underline{n}_2|} \qquad \text{(A47.b)}$$

$$dS = \left\{(\frac{\partial z}{\partial x})^2 + (\frac{\partial z}{\partial y})^2 + 1\right\}^{\frac{1}{2}} dxdy \quad . \qquad \text{(A47.c)}$$

We wish to solve for φ_1, $\frac{\partial\varphi_1}{\partial n_1}$, φ_2, and $\frac{\partial\varphi_2}{\partial n_2}$ using expressions (A45) and (A46). Once we obtain the values of the potentials and their normal derivatives on the surface, we substitute them into equations (A44) and obtain the values of the potential off the surface. We proceed by taking the time Fourier transform of equation (A45). The convolutions become multiplications.

$$\tfrac{1}{2}\varphi_i(\underline{r}_1,\omega) = \int_{\partial V} G_i(\underline{r}_1,\underline{r}_o,\omega)\frac{\partial \varphi_i}{\partial n}(\underline{r}_o,\omega)dS_o - P\int_{\partial V}\varphi_i(\underline{r}_o,\omega)\frac{\partial G_i}{\partial n}(\underline{r}_1,\underline{r}_o,\omega)dS_o \quad \text{(A48)}$$

$$+ f_i(\underline{r}_1,\omega)$$

Consider the case of φ_1. Equation (A48) describes a complex coupling between φ_1 at $\underline{r}_1$ and the values of φ_1 and $\frac{\partial \varphi_1}{\partial n_1}$ at all other points on the surface. To gain insight as to the method of decoupling, we evaluate equation (A48) for an infinitely flat surface. Then

$$dS_o = dx_o\, dy_o \quad \text{(A49.a)}$$

$$\nabla\underline{\varphi}_1 = -\frac{\partial \varphi_1}{\partial z} \quad \text{(A49.b)}$$

$$G_1 = -\frac{e^{-i\omega\frac{R}{a_1}}}{4\pi R} \quad . \quad \text{(A49.c)}$$

Here $R = (x_1 - x_o)^2 + (y_1 - y_o)^2$. The integral (A48) reduces to

$$\tfrac{1}{2}\varphi_1(\underline{r}_1,\omega) = \int_{-\infty}^{\infty}\int_{-\infty}^{\infty}\frac{e^{-i\omega\frac{R}{a_1}}}{4\pi R}\frac{\partial \varphi_1}{\partial z}(x_o,y_o)dx_o\,dx_o \quad \text{(A50)}$$

$$+ f_1(\underline{r}_1,\omega) \quad .$$

The principal value contribution vanishes because $\nabla\underline{G}\cdot\underline{n}$ on a flat surface is zero everywhere. Expression (A50) is a two-dimensional spatial convolution. Upon taking the two spatial transforms, one obtains

$$\tfrac{1}{2}\tilde{\varphi}_1(\underline{k}_1,\omega) = \tilde{G}(\underline{k}_1,\omega)\frac{\partial \tilde{\varphi}_1}{\partial z} + f(\underline{k}_1,\omega) \quad . \quad \text{(A51)}$$

We obtain the two-dimensional spatial transform of $G_1(\underline{r}_1,\omega)$ where

$$\tilde{G}(\underline{k},\omega) = \int_{-\infty}^{\infty}\int_{-\infty}^{\infty} \frac{e^{-i\omega\frac{R}{a_1}}}{4\pi R} e^{ik_x x} e^{ik_y y}\, dx dy \tag{A52}$$

by transforming the Cartesian coordinates into angular coordinates

$$x + iy = Re^{i\varphi} \tag{A53}$$

$$k_x + ik_y = qe^{i\theta}$$

$$k_x x = Rq\cos\varphi\cos\theta$$

$$k_y y = Rq\sin\varphi\sin\theta \quad .$$

Therefore, the integral (A52) simplifies to

$$\tilde{G} = \int_0^{\infty}\int_0^{2\pi} \frac{e^{-i\omega\frac{R}{a_1}}}{4\pi R} e^{iRq\cos\beta} R\, dR\, d\beta \quad . \tag{A54}$$

Here $\beta = \varphi - \theta$. We next apply the identity

$$J_o(z) = \frac{1}{2\pi}\int_0^{2\pi} e^{-iz\cos\beta} d\beta \tag{A55}$$

to reduce equation (A54) to a one-dimensional Fourier transform of the Bessel function.

$$\tilde{G} = \int_0^{\infty} \frac{e^{-i\omega\frac{R}{a}}}{4\pi} J_o(qR) dR \tag{A56}$$

We look up the Fourier transform of the Bessel function and obtain the final result that

$$\tilde{\varphi}_1(\underline{k}_1,\omega) = \frac{1}{i\nu_1}\frac{\partial\tilde{\varphi}_1}{\partial n_1} + 2\tilde{f}_1(\underline{k}_1,\omega) \quad . \tag{A57}$$

Similarly we obtain the transmitted potential

$$\tilde{\varphi}_2(\underline{k}_1,\omega) = \frac{1}{i\nu_2}\frac{\partial\tilde{\varphi}_2}{\partial n_2} \quad . \tag{A58}$$

Here $\nu_i = \left\{\frac{\omega^2}{\alpha_i} - k_x^2 + k_y^2\right\}^{\frac{1}{2}}$. Now along with the transformed boundary conditions

$$\frac{1}{\rho_1}\frac{\partial\tilde{\varphi}_1}{\partial n_1} = -\frac{1}{\rho_2}\frac{\partial\tilde{\varphi}_2}{\partial n_2} \tag{A59}$$

and

$$\tilde{\varphi}_1 = \tilde{\varphi}_2$$

we have an algebraic system of four equations and four unknowns. Solving these equations yields the standard plane wave reflection and transmission solutions.

$$\tilde{\varphi}_1 = (1+R)\tilde{f} \tag{A60}$$

$$\tilde{\varphi}_2 = T\tilde{f}$$

$$\frac{\partial\varphi_1}{\partial n_1} = -i\nu_1(1-R)\tilde{f}$$

$$\frac{\partial \varphi_2}{\partial n_2} = i\nu_2 T\tilde{f}$$

where

$$R = \frac{\frac{\nu_1}{\rho_1} - \frac{\nu_2}{\rho_2}}{\frac{\nu_1}{\rho_1} + \frac{\nu_2}{\rho_2}}$$

and

$$T = \frac{\frac{2\nu_1}{\rho_1}}{\frac{\nu_1}{\rho_1} + \frac{\nu_2}{\rho_2}} .$$

These solutions are in the Fourier domain. The solution in x-y space, for φ_1, is

$$\varphi_1(\underline{r}_1,\omega) = \int_{-\infty}^{\infty}\int_{-\infty}^{\infty}(1 + R)\,\tilde{f}e^{-ik_x x}e^{-ik_y y}\,dk_x\,dk_y \quad . \tag{A61}$$

The solution is a summation of weighted plane waves. If we assume that f is a point source,

$$f(\underline{r},t) = \frac{f(t - \frac{R_o}{\alpha_1})}{R_o} \tag{A62}$$

where $R_o = |\underline{r}-\underline{r}_1|$, then the spatial and time fourier transform is

$$\tilde{f} = \frac{e^{-\nu_1|z|}}{\nu_1} \quad . \tag{A63}$$

Substitution of this expression into equation (A60) yields the Weyl integral.

$$\varphi_1(\underline{r}_1,\omega) = \int_{-\infty}^{\infty}\int_{-\infty}^{\infty}(1 + R)\frac{e^{\nu_1|z|}}{\nu_1}e^{-ik_x x}e^{-ik_y y}\,dk_x\,dk_y \qquad \text{(A64)}$$

This is the expected result for an infinitely flat surface. Several authors (Aki and Richards,1980) show that the two dimensional Weyl integral can be transformed into the one dimensional Sommerfeld integral.

$$\int(1 + R)k_r J_o(k_r r)\frac{e^{-\nu_1|z|}}{\nu_1}dk_r \qquad \text{(A65)}$$

where

$$\nu_1 = \left[\frac{\omega^2}{\alpha_1} - k_r^2\right]^{1/2}$$

A stationary phase evaluation, valid for high frequencies, yields (Aki and Richards, 1980)

$$\varphi_1(\underline{r}_1,\omega) = \frac{(1 + R(p_o))}{R_o}e^{-i\omega\frac{R_o}{\alpha_1}} \qquad \text{(A66)}$$

This is the Kirchhoff-Helmholtz boundary value. A similar expression can be obtained for $\varphi_2(\underline{r}_1,\omega)$. We substitute these boundary values into equation (A44) to obtain the potential off the surface. To complete the discussion for the planar case, we include a further identity. We note that the whole-space solution $f(\underline{r},t)$ is a valid solution of equation (A44). Substitution of $f(\underline{r},t)$ for φ and $\frac{\partial f}{\partial n}$ for $\frac{\partial \varphi}{\partial n}$ yields the identity

$$\int_{\partial V}(f^*\frac{\partial G}{\partial n} - \frac{\partial f}{\partial n}^*G)dS_o = 0 \quad . \tag{A67}$$

Thus the incident part of the reflected Kirchhoff-Helmholtz boundary values vanishes when substituted into the representation integral for a receiver off the surface.

Clearly the Kirchhoff-Helmholtz boundary values for the potentials φ_1 and φ_2 are independent of the tilt of the plane. Thus we can use these results to decouple the integral equation (A45) for an arbitrary surface. Let us expand equation (A45) out for an arbitrary surface.

$$\tfrac{1}{2}\varphi(\underline{r}_1,\omega) = \int\int G(R,\omega)\left[\frac{\partial\varphi}{\partial x}\frac{\partial z}{\partial x}(x_o,y_o) + \frac{\partial\varphi}{\partial y}\frac{\partial z}{\partial y}(x_o,y_o) - \frac{\partial\varphi}{\partial z}(x_o,y_o)\right]dx_o\,dy_o \tag{A68}$$

$$P\int\int\varphi\frac{\partial G}{\partial R}\frac{1}{R}\left[(x_1-x_o)\frac{\partial z}{\partial x} + (y_1-y_o)\frac{\partial z}{\partial y} - (z(x_1,y_1) - z(x_o,y_o))\right]dx_o\,dy_o$$

Here $R = (\Delta x^2 + \Delta y^2 + \Delta z^2)^{\frac{1}{2}}$. If we could discard terms of Δz, we could reduce this integral to a spatial convolution and solve for the boundary values as in the infinite plane example. We justify discarding these terms by supposing that the frequency content of the incident source field is high. Therefore G and $\frac{\partial G}{\partial R}$ oscillate rapidly but have a slowly varying magnitude as a function of distance away from the receiver point. We also assume that φ, $\frac{\partial\varphi}{\partial n}$, and $\underline{n}\cdot\nabla R$ on the surface vary slowly. Given these assumptions, we argue that the major contributions to the integral (A67) come from points close to the receiver point $\underline{r}_1$ and not from points on the surface which are remote from the receiver. Therefore we may replace $z(x_o,y_o)$ with a simpler

function which approximates the actual topography well near $\underline{r}_0 = \underline{r}_1$. In fact, by discarding terms of Δz in (A67), we replace $z(x_0, y_0)$ with a plane which is tangent to the surface at $\underline{r}_1$ (see Figure A.3). In addition to substituting the tangent plane for the actual surface, we change the limits of the integration in (A67) from a finite surface to an infinite surface. We may do this without introducing much error if the integral is dominated by contributions close to the receiver. Then a simple coordinate transformation of the integral (A67) yields (A50). This completes the derivation of the Kirchhoff-Helmholtz boundary conditions.

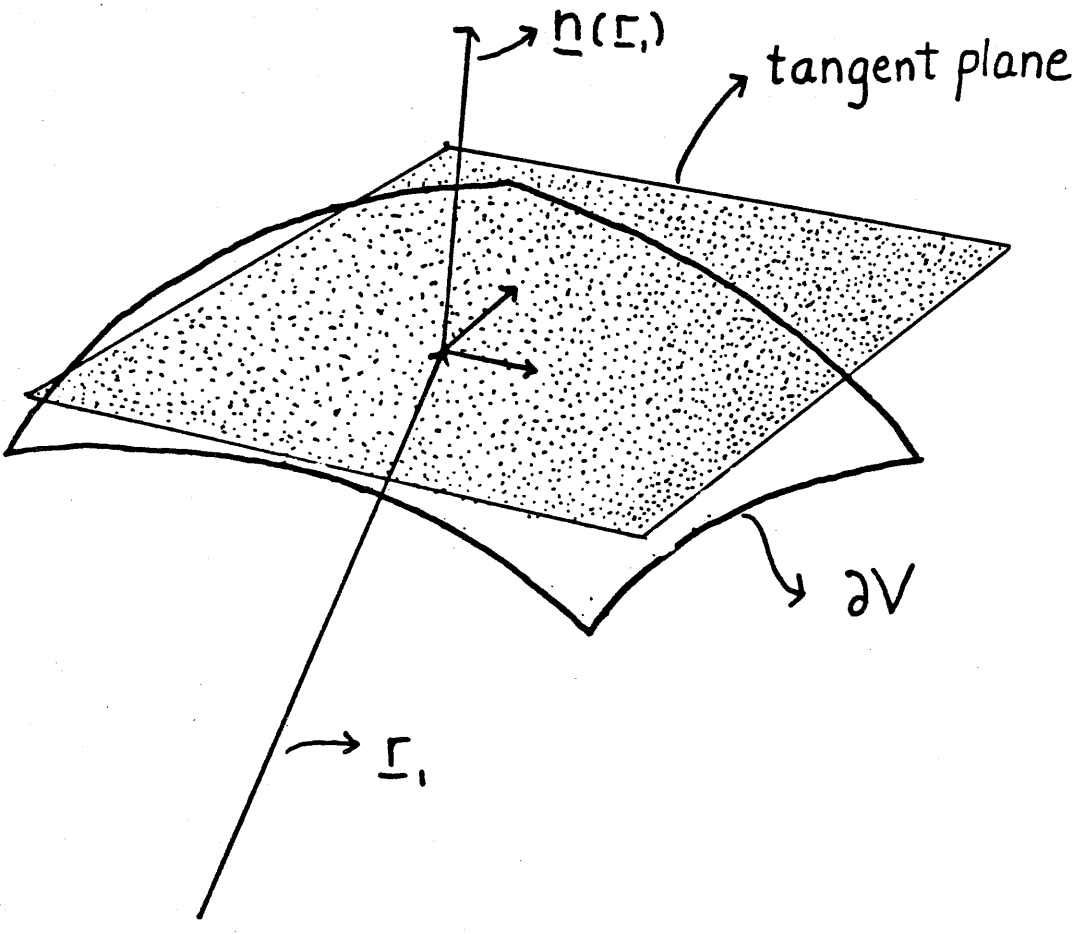

Figure A.3. The tangent plane surface.

REFERENCES

Aki, K. and P. Richards (1980), *Quantitative Seismology: Theory and Methods*, Vol. I, W. H. Freeman and Co., San Francisco.

Banaugh, R. (1962), *Scattering of acoustic and elastic waves by surfaces of arbitrary shape* (Thesis, University of California, Lawrence Radiation Laboratory).

Cole, D. (1980), *A numerical boundary integral equation method for transient motions* (Thesis, California Institute of Technology).

Kellogg, O. D. (1953), *Foundations of Potential Theory*, Dover Publications, Inc., New York.

Mow, C. and Y. Pao (1971), *The diffraction of elastic waves and dynamic stress concentrations*, #R-482-RR, A report prepared for United States Air Force Project Rand.

Officer, C. B. (1958), *Introduction to the Theory of Sound Transmission Theory*, McGraw-Hill Book Co., New York.